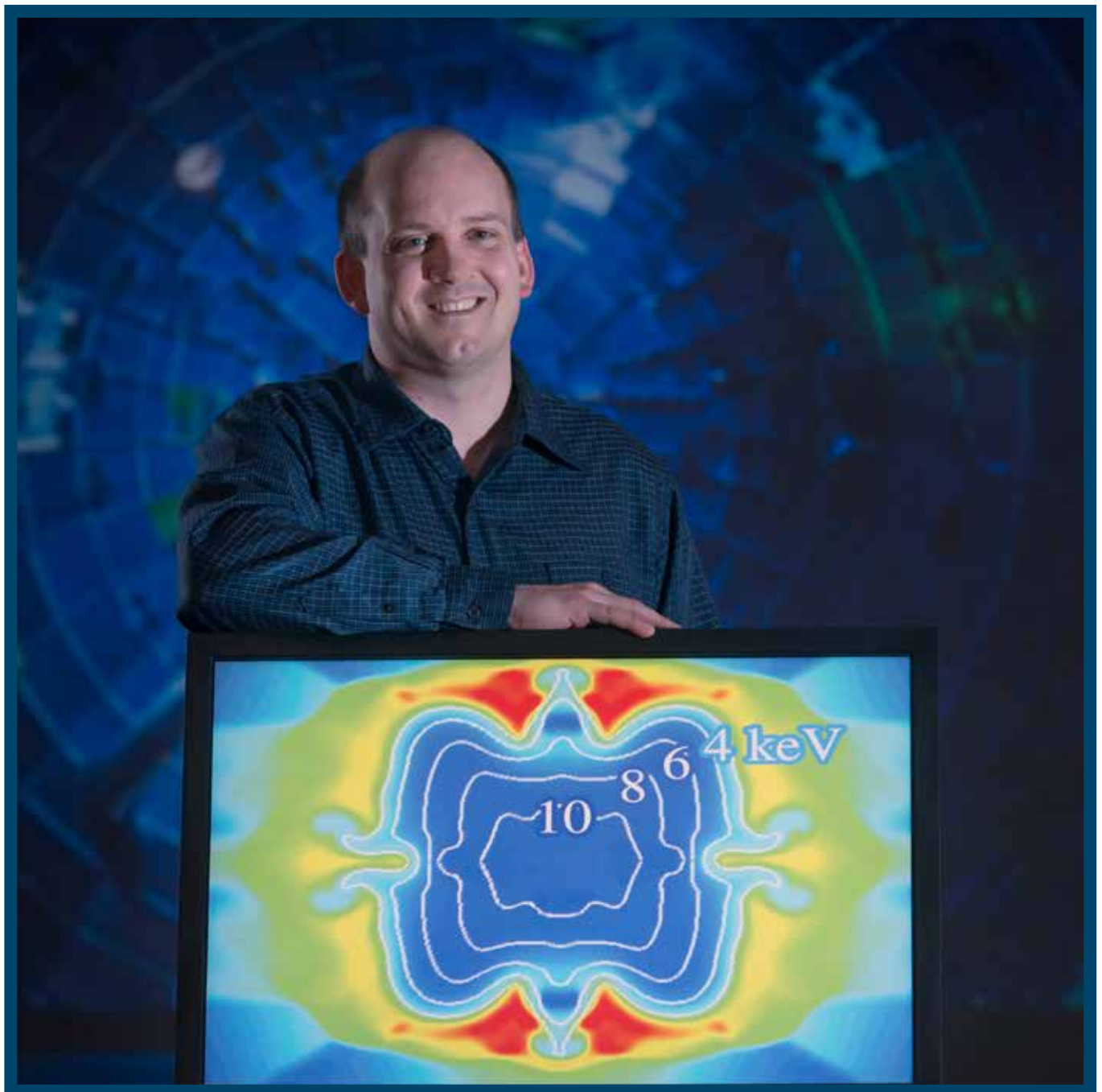


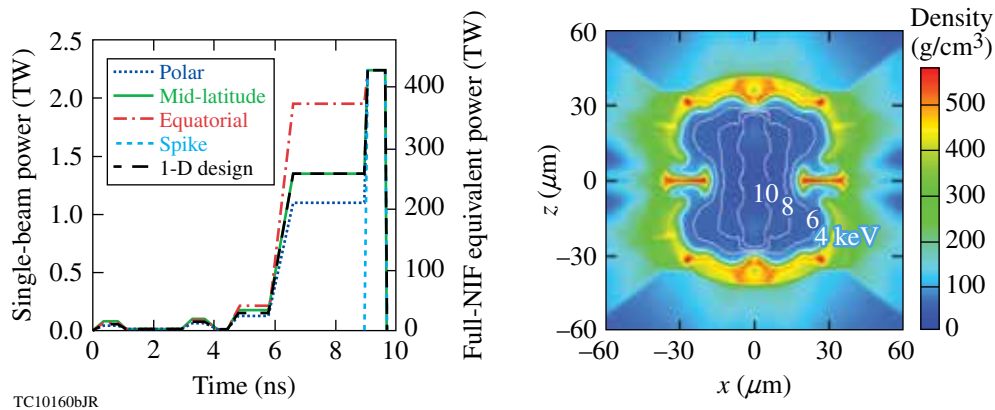
LLE Review

Quarterly Report



About the Cover:

The cover photo shows LLE scientist Dr. Kenneth Anderson and a simulation of target density and temperature at the onset of ignition for a polar-drive shock-ignition point design on the National Ignition Facility. In shock ignition, the shell-compression and hot-spot-ignition phases are distinct, and a subset of the laser beams is used to heat the hot-spot to ignition temperatures with a high-intensity spike. The required pulse shape and power for all beams are compatible with NIF performance. The 1-D and 2-D simulations take into account the known sources of instabilities and uncertainties to quantify the gain for a 1080- μm -radius target with a 161- μm solid DT-fuel layer surrounded by a 31- μm outer plastic ablator layer. Credit: Lawrence Livermore National Laboratory for background image on cover.



The figure on the left shows the required on-target pulse shapes in the full-quad geometry for shock ignition. The four beams within each of the 48 NIF quads have the same pulse shape, and the quads are pointed and shaped for compression (all the beams from Ring 1 as polar beams, and half of the beams from Rings 2 and 3 as mid-latitude and equatorial beams) and ignition spike (all remaining beams, including all the beams from Ring 4). The figure on the right displays the simulated density and temperature contour at the onset of ignition for the target in these conditions.

This report was prepared as an account of work conducted by the Laboratory for Laser Energetics and sponsored by New York State Energy Research and Development Authority, the University of Rochester, the U.S. Department of Energy, and other agencies. Neither the above-named sponsors nor any of their employees makes any warranty, expressed or implied, or assumes any legal liability or responsibility for the accuracy, completeness, or usefulness of any information, apparatus, product, or process disclosed, or represents that its use would not infringe privately owned rights. Reference herein to any specific commercial product, process, or service by trade name, mark, manufacturer, or otherwise, does not necessarily constitute or imply its endorsement, recommendation, or favoring

by the United States Government or any agency thereof or any other sponsor. Results reported in the LLE Review should not be taken as necessarily final results as they represent active research. The views and opinions of authors expressed herein do not necessarily state or reflect those of any of the above sponsoring entities.

The work described in this volume includes current research at the Laboratory for Laser Energetics, which is supported by New York State Energy Research and Development Authority, the University of Rochester, the U.S. Department of Energy Office of Inertial Confinement Fusion under Cooperative Agreement No. DE-FC52-08NA28302, and other agencies.

Printed in the United States of America
Available from
National Technical Information Services
U.S. Department of Commerce
5285 Port Royal Road
Springfield, VA 22161
www.ntis.gov

For questions or comments, contact
Christophe Dorrer, Editor
Laboratory for Laser Energetics
250 East River Road
Rochester, NY 14623-1299
(585) 273-2778
www.lle.rochester.edu

LLE Review

Quarterly Report



Contents

In Brief	iii
A Polar-Drive Shock-Ignition Design for the National Ignition Facility.....	1
Polar-Drive Implosions on OMEGA and the National Ignition Facility.....	15
Cross-Beam Energy Transfer in Polar-Drive Implosions on OMEGA.....	27
Measured Hot-Electron Intensity Thresholds Quantified by a Two-Plasmon–Decay Resonant Common-Wave Gain in Various Experimental Configurations	33
Mitigation of Cross-Beam Energy Transfer: Implications of Two-State Optical Zooming on OMEGA.....	43
Measuring 8- to 250-ps Short Pulses Using a High-Speed Streak Camera on Kilojoule, Petawatt-Class Laser Systems.....	58
A Solid-State, Inductive-Adder, 10-kV Pulse Generator for Driving Large-Aperture Pockels Cells	64
Publications and Conference Presentations	

In Brief

This volume of the LLE Review, covering October–December 2012, features “A Polar-Drive Shock-Ignition Design for the National Ignition Facility” by K. S. Anderson, R. Betti, P. W. McKenty, T. J. B. Collins, M. Hohenberger, W. Theobald, R. S. Craxton, J. A. Delettrez, M. Lafon, J. A. Marozas, R. Nora, S. Skupsky, and A. Shvydky. In this article (p. 1), the performance of a shock-ignition polar-drive design is estimated using 1-D and 2-D simulations for implementation on the National Ignition Facility. The authors quantify the impact of instabilities and uncertainties on gain to study the robustness of this approach in experimental conditions. The target is shown to robustly ignite when taking into account uncertainties in the shock timing and initial gas density and nonuniformities caused by the laser drive, capsule position, and asymmetries.

Additional highlights of research presented in this issue include the following:

- P. B. Radha, F. J. Marshall, J. A. Marozas, A. Shvydky, I. Gabalski, T. R. Boehly, T. J. B. Collins, R. S. Craxton, D. H. Edgell, R. Epstein, D. H. Froula, V. N. Goncharov, M. Hohenberger, P. W. McKenty, T. C. Sangster, and S. Skupsky (LLE); R. L. McCrory and D. D. Meyerhofer (LLE and Departments of Mechanical Engineering and Physics, University of Rochester); and J. A. Frenje and R. D. Petrasso (MIT) simulate polar-drive experiments on OMEGA and observe a good agreement with *DRACO* simulations in terms of areal density and symmetry (p. 15). The scaling of these experiments to the National Ignition Facility and the role of laser–plasma interactions are discussed.
- D. H. Edgell, R. E. Bahr, V. N. Goncharov, I. V. Igumenshchev, J. F. Myatt, P. B. Radha, W. Seka, and D. H. Froula present a comparison of measured and simulated angular dependence of the unabsorbed light in OMEGA experiments (p. 27). The 3-D simulations show that cross-beam energy transfer explains the decreased laser absorption, which can be mitigated using smaller laser beams on target and tuning the wavelength of the laser beams organized in different rings.
- D. T. Michel, A. V. Maximov, R. W. Short, J. A. Delettrez, S. X. Hu, I. V. Igumenshchev, J. F. Myatt, A. A. Solodov, C. Stoeckl, B. Yaakobi, and D. H. Froula describe a model of two-plasmon decay based on a common electron plasma wave (p. 33). This model is consistent with the threshold for hot-electron production measured in multibeam OMEGA and OMEGA EP experiments.
- D. H. Froula, T. J. Kessler, I. V. Igumenshchev, A. Shvydky, J. H. Kelly, J. D. Zuegel, E. Hill, and V. N. Goncharov review the physics and possible implementations of two-state optical zooming to mitigate cross-beam energy transfer on OMEGA (p. 43). Scattering of the incident laser energy is reduced using a smaller beam radius on target for the main drive while maintaining the beam size for the pickets.
- J. Qiao, P. A. Jaanimagi, R. Boni, J. Bromage, and E. Hill report on the reliability and accuracy improvement of streak-camera–based short-pulse measurements by homogenizing the slit illumination using an anamorphic diffuser and calibrating the space-charge broadening, for application to the measurement of OMEGA EP pulses with durations ranging from 8 to 250 ps (p. 58).

- W. Bittle and J. D. Zuegel present the design of a new solid-state, high-voltage pulse generator for driving large-aperture Pockels cells (p. 64). These generators are reliable replacements for the obsolete thyratron-based drivers used in the large-aperture ring amplifiers of the OMEGA and OMEGA EP front ends.

Christophe Dorrer
Editor

A Polar-Drive Shock-Ignition Design for the National Ignition Facility

Introduction

In direct-drive inertial confinement fusion (ICF),¹ a small spherical capsule filled with a deuterium–tritium (DT) mix is imploded by irradiating the capsule symmetrically with high-intensity lasers to achieve a high-density, high-temperature state where fusion reactions may readily occur. The capsule shell is accelerated by the ablation pressure of the laser-heated plasma at the outer edge of the shell to high velocity ($v_{\text{imp}} > 3.5 \times 10^7$ cm/s, where v_{imp} is the implosion velocity), compressing the capsule to a high density. As the capsule implodes, the back pressure from the compressed plasma in the center of the capsule slows the implosion until the shell stagnates. At stagnation, the fill gas has been compressed and heated via shocks and adiabatic compression, forming a low-density central hot spot surrounded by a dense shell tamper consisting of DT fuel. If sufficient hot-spot temperature (≥ 10 keV) and shell areal density ($\rho R \equiv \int_0^\infty \rho dr \geq 0.3$ g/cm²) are achieved, energetic alpha particles created by the hot-spot fusion reactions are stopped in the cold dense shell, heating it quickly, and initiating ignition, which causes the fusion reaction rate to rise dramatically, burning a substantial portion of the DT fuel.

Shock ignition (SI)² is a relatively new concept in which the compression phase and ignition phase are separated.³ Practically, this separation is achieved by dividing the laser pulse into two parts: a main-drive or compression pulse, and a spike or ignition pulse timed at the end of the main pulse. The main-drive pulse is typically of lower power than in hot-spot direct drive since the main pulse serves solely to compress the shell to the required areal density for ignition and not to heat the hot spot. This lower drive power corresponds to a lower implosion velocity, typically less than 3.0×10^7 cm/s. At the end of the main pulse, an intense spike pulse launches a strong shock through the imploding shell material to heat the hot spot quickly to ignition temperatures.

By separating the compression from the hot-spot heating, SI somewhat resembles the fast-ignition concept.⁴ However, SI requires a spherically symmetric laser illumination of much more moderate laser intensity (typically several times

10^{15} W/cm²) than is required for fast ignition ($> 10^{19}$ W/cm²), such that the SI heating pulse can be generated with the same laser system as the main-drive pulse. In contrast, fast ignition requires chirped-pulse amplification to generate pulses of high intensity. Furthermore, SI heating is accomplished via shock heating, which is well understood and easily modeled, as opposed to fast ignition, which delivers energy via the generation and transport of relativistic fast electrons, which is difficult to model theoretically or computationally.

Achieving ignition through SI is not without its uncertainties. For SI to be viable, laser-generated strong shocks of the order of 300 Mbar must be demonstrated experimentally in a spherical geometry. Furthermore, at these intensities, laser–plasma interactions (LPI’s) become significant and can greatly influence the coupling of laser energy to the imploding capsule, affecting the strong-shock formation and potentially preheating the cold fuel prior to full capsule compression. An experimental understanding of LPI in this intensity regime, therefore, is very important in predicting the success of SI implosions.

It should be noted that a concept similar to SI was proposed a few decades ago by Shcherbakov.⁵ The concept proposed at that time, however, called for much lower initial compression velocities $v_{\text{imp}} \simeq 2.0 \times 10^6$ cm/s (the final velocity after the shock pulse is quoted as $v_{\text{imp}} \simeq 1.5 \times 10^7$ cm/s). The laser drive needed to compress and shock the capsule in that design was not specified, and only the absorbed laser energy $E \simeq 30$ kJ was cited. An article by the same author two decades later⁶ indicates laser-drive parameters of $P \simeq 10$ TW, $I \simeq 10^{13}$ W/cm², and $\Delta t_{\text{pulse}} \simeq$ tens of nanoseconds, with shock laser parameters of $P \simeq 10$ PW, $I \simeq 10^{16}$ W/cm², and $\Delta t_{\text{pulse}} \simeq$ a few hundreds of picoseconds. This work, therefore, seems to indicate very different regimes of both laser operation and capsule design relative to the conceptual paper of Betti *et al.*² even though the concept is essentially the same.

Research in SI^{7–30} has garnered much interest both experimentally and theoretically in the international fusion community over the past several years. Theoretical models,^{7–10} scaling

laws,^{7,11–16} and computational target designs in one dimension (1-D)^{11,13,14,17,18} and multiple dimensions^{13–15,18–20} have investigated the feasibility of SI on a variety of target platforms. These studies have validated the claims of Betti *et al.*² that the addition of a strong shock reduces the energy required for ignition, allowing for higher gain at a given input laser energy. Strong-shock propagation experiments in planar²¹ and spherical geometry²² have validated computation modeling of shocks driven at intensities up to 1.5×10^{15} W/cm². Full-implosion experiments²³ have been performed on OMEGA²⁴ showing increased neutron yield, areal density, and yield-over-clean (defined as the ratio of the experimental yield to 1-D simulated predictions) relative to similar no-spike experiments. Particle-in-cell LPI simulations of OMEGA experiments²⁵ and full-scale ignition designs²⁶ have reported hot-electron generation in the temperature regime up to 40 keV at SI-relevant laser intensities with total reflectivities (Raman and Brillouin scattering) from 10% to 35% of the incident laser energy. Spherical LPI experiments^{27,28} performed on OMEGA at SI-relevant intensities and plasma conditions have resulted in similar findings. Planar LPI experiments²⁹ have also been performed in France. The hot-electron temperatures reported in these simulations and experiments appear favorable for SI in light of computational investigations of hot-electron coupling during spike propagation,³⁰ which report enhanced strong-shock pressures and higher ignition margin as a result of hot-electron energy coupling at electron temperatures up to 100 keV. All of these studies indicate that the SI method is a viable path to achieve ignition and gain in ICF.

Most of the theoretical research published to date has been limited to either conceptual designs or designs for proposed laser facilities or facilities still under construction. This article proposes a design for experiments on the currently operational National Ignition Facility (NIF).³¹ These proposed experiments conform to the NIF system specifications and could be fielded in the polar-drive configuration on the NIF within the next several years, requiring only minor system modifications. Such modifications include the design and manufacture of specifically tailored phase plates;^{32,33} implementation of multifrequency-modulation smoothing by spectral dispersion (multi-FM SSD)^{34,35} in NIF beamlines; design and introduction of polarization plates for polarization smoothing; and the development of a polar-drive target insertion cryostat.

This article is organized as follows: A theoretical model for calculating target robustness is outlined; a 1-D target design for the NIF is developed and implosion robustness to 1-D physics and system uncertainties is detailed; and a polar-drive

beam configuration for the NIF is outlined and robustness to two-dimensional (2-D) drive and capsule nonuniformities is explored. The capsule is found to robustly ignite under all anticipated sources of 1-D uncertainty and 2-D perturbations.

Characterizing Robustness

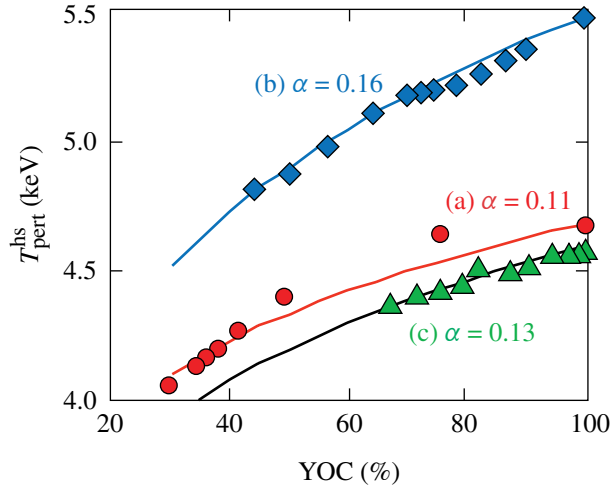
In ICF target design, it is important to characterize design performance. Often in the ICF community, 1-D target gain has been used as a metric to preferentially guide target design. One-dimensional gain in an igniting target, however, is largely a function of the assembled fuel areal density (see Ref. 1, p. 40) and, as a metric for target design, does not provide a reference for how close the target implosion is to the ignition threshold. It is therefore important to define a metric for the margin of error, in a 1-D sense, to quantify the robustness of the proposed shock-ignition design for the NIF. In this article, target designs will be characterized using the ignition threshold factor (ITF).^{36–38} By the definition of ITF as described in Spears *et al.*,³⁸ an ITF of 1 corresponds to an ~50% chance of ignition with the DT target in simulations.

In this article, the ITF is calculated in 1-D simulations using the methodology of Chang *et al.*³⁷ Essentially, the fusion reactivity rate $\langle\sigma\nu\rangle$ of the DT fuel is artificially reduced by a variable parameter in the simulation

$$\langle\sigma\nu\rangle_{\text{mod}} = \xi\langle\sigma\nu\rangle \quad (1)$$

until the target yield degrades to a gain of 1, where the fusion output energy equals the input laser energy. Here $\langle\sigma\nu\rangle_{\text{mod}}$ is the modified fusion reactivity rate, and ξ is the fractional input parameter. This is analogous to multiplying the neutron yield obtained in the absence of alpha-particle heating by the same factor. One may characterize this input parameter ξ as a clean-volume fraction, defined as the fraction of the 1-D hot-spot volume $\xi = V_{3\text{-D}}^{\text{hs}}/V_{1\text{-D}}^{\text{hs}}$, where $V_{3\text{-D}}^{\text{hs}}$ is the clean hot-spot volume in three dimensions (3-D) varied as an input parameter and $V_{1\text{-D}}^{\text{hs}}$ is the 1-D hot-spot volume.

In simple models of clean volume fraction, the yield-over-clean (YOC), which is defined as the 3-D yield divided by the 1-D yield ($\text{YOC} \equiv Y_{3\text{-D}}/Y_{1\text{-D}}$), is typically equated to the clean-volume fraction. These models, however, ignore the effect of shell perturbations on the hot-spot temperature. Two-dimensional DRACO³⁹ simulations of three igniting targets, described in Fig. 3 of Ref. 37 with varying levels of input nonuniformity, are used to evaluate the functional dependence of the hot-spot ion temperature on the YOC. In Fig. 133.1, the neutron-averaged ion temperature is plotted for these three



TC10412JR

Figure 133.1

Relation of the hot-spot temperature ($T_{\text{pert}}^{\text{hs}}$) to the yield-over-clean (YOC), as calculated by 2-D DRACO simulations for the three targets discussed in Fig. 3 of Ref. 37. Power-law fits to each of these are shown as solid lines with power-law exponents varying from 0.11 to 0.16.

targets [labeled (a), (b), and (c), as in Ref. 37] versus the no-burn YOC. The perturbed, hot-spot ion temperature for each of these designs is shown to scale roughly as a weak power-law function of the YOC:

$$T_{\text{pert}}^{\text{hs}}(\text{YOC}) = T_{1\text{-D}}^{\text{hs}} \cdot \text{YOC}^{\alpha}, \quad (2)$$

as shown by the continuous lines of Fig. 133.1. The power-law exponent α was found to vary from 0.11 to 0.16 in the different designs. Here, we will assume an average value of 0.13 for α .

We employ a simple model of the hot spot, which assumes a single temperature over the hot-spot volume

$$\text{YOC} = \frac{Y_{3\text{-D}}}{Y_{1\text{-D}}} = \xi \left(\frac{T_{3\text{-D}}^{\text{hs}}}{T_{1\text{-D}}^{\text{hs}}} \right)^{\beta}, \quad (3)$$

where $T_{3\text{-D}}^{\text{hs}}$ is the perturbed hot-spot ion temperature and $T_{1\text{-D}}^{\text{hs}}$ is the 1-D hot-spot ion temperature. The fusion reactivity in the hot spot is assumed to scale as a power law⁴⁰ in the temperature over the temperatures of interest, with $\beta = 2$.

Using the formula for the χ parameter from Eq. (12) of Ref. 37,

$$\chi = \left[\rho R (\text{g/cm}^2) \right]^{0.8} (T/4.7 \text{ keV})^{1.7} (\text{YOC})^{0.5}, \quad (4)$$

the scalings for areal density ρR and hot-spot ion temperature from Eqs. (19) and (52), respectively, of Ref. 41,

$$\rho R_{\text{shell}} \sim E_{\text{kin}}^{0.33} \quad (5)$$

and

$$T_{\text{hs}} \sim E_{\text{kin}}^{0.07}, \quad (6)$$

and defining the ITF as the ratio of the kinetic energy E_{kin} of the imploding shell to the minimum energy required to ignite the same shell, one obtains a scaling relation between χ and the ITF,

$$\text{ITF} \sim \chi^{2.6}. \quad (7)$$

Substituting Eqs. (2)–(4) into Eq. (7) yields

$$\text{ITF} \sim \xi^{1.5}. \quad (8)$$

When a series of 1-D simulations with alpha-energy transport are performed, varying the clean-volume fraction ξ , one finds a critical value of ξ , below which ignition is quenched. We will term this the minimum clean-volume fraction required for ignition $\xi_{\text{min}}^{\text{ign}}$, which corresponds to an ITF of 1. Using $\xi_{\text{min}}^{\text{ign}}$, one can rewrite Eq. (8) for the 1-D ITF as

$$\text{ITF}_{1\text{-D}} \simeq (\xi_{\text{min}}^{\text{ign}})^{-1.5}. \quad (9)$$

In this article, we will use Eq. (9) to determine the 1-D robustness of our target design.

One-Dimensional Target Design and Robustness Studies

This section outlines the NIF SI target design in 1-D and details the robustness of the target to various sources of physics and system uncertainties. In designing a shock-ignition target for the NIF, the most-constraining system limitation is the total system's peak laser power. The early SI design at 290 kJ proposed by Betti *et al.*² used a laser spike with a peak laser power of 540 TW. Scaling this target to NIF's total energy of ~ 1.5 MJ, the required laser power reaches ~ 1600 TW, prohibitively high for the NIF, which recently achieved⁴² a peak power of 520 TW. Indeed, Betti's design at 290 kJ already exceeds the demonstrated NIF peak power. Therefore, some modifications to the conceptual design must be made for experiments on the NIF. The first is to scale only to sub-MJ laser energy to allow for more headroom in power space. The second is to raise the capsule's implosion velocity by making the shell thinner. This recovers the stagnation pressure and temperature that is lost

when simply reducing the laser power to conform to the NIF’s power ceiling. Additional robustness is achieved by allowing that the laser pulse may be split, such that half of the NIF beams drive the target compression and are focused at the original target radius, while the other half drive the spike shock using more tightly focused beams to improve energy coupling to the target late in time. All 1-D simulations in this article were performed using the radiation–hydrodynamics code *LILAC*⁴³ with the *SESAME*⁴⁴ equation of state and a flux-limited Spitzer heat conductivity⁴⁵ with a flux-limiter value of 0.06.

The target design chosen is shown in Fig. 133.2. The capsule has a 1080- μm radius with a 161- μm solid-DT fuel layer surrounded by a 31- μm outer plastic ablator layer. The ablator thickness is chosen such that the ablator material is fully ablated by the end of the laser pulse to mitigate deceleration-phase mixing of the plastic with the DT fuel. The total energy delivered by the laser is 689 kJ, divided into two pulses, as shown in Fig. 133.3. The main pulse shown by the solid line contains a total of 544 kJ and has a laser profile characterized as a super-Gaussian intensity profile $I(r) = \exp\left[-(r/r_0)^\sigma\right]$ with a $1/e$ radius $r_0 = 677 \mu\text{m}$ and super-Gaussian exponent $\sigma = 2.5$. The spike pulse (dashed line) contains a total of 145 kJ with a peak power of 215 TW, also in a super-Gaussian spot of $r_0 = 258 \mu\text{m}$ and $\sigma = 2.5$.

As seen in Fig. 133.3, the laser pulse design has two “picket” pulses at the beginning, followed by a low-intensity foot with a slow rise to the main compression drive, and ultimately concluding with a spike pulse at the end of the main compression.

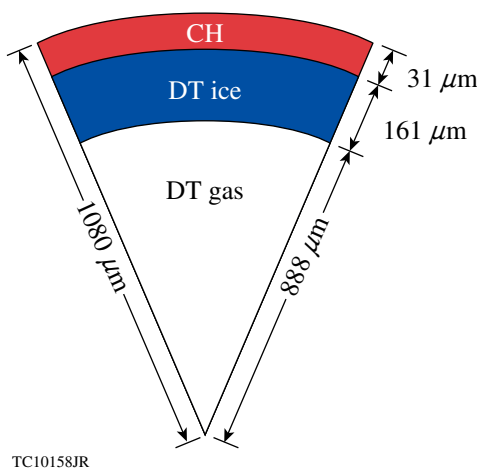


Figure 133.2
Capsule dimensions for the NIF shock-ignition (SI) design.

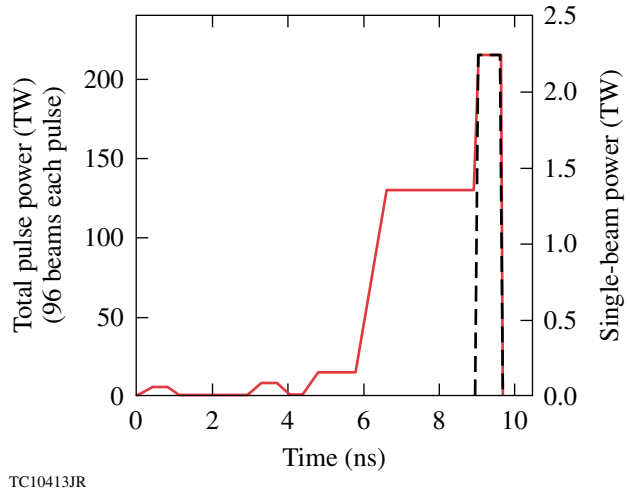


Figure 133.3
Laser pulse history for the main drive beams (solid red) and spike beams (dashed black) comprising the 1-D SI laser pulse design.

The picket pulses serve two purposes: The first is to raise the ablation velocity^{46–49} $v_{\text{abl}} = \dot{m}/\rho_{\text{abl}}$ (where v_{abl} is the ablation velocity, \dot{m} is the mass ablation rate, and ρ_{abl} is the density at the ablation front) to reduce the growth of the Rayleigh–Taylor (RT) instability,^{50,51} which is a major obstacle to ICF. This ablative stabilization of the RT instability has been demonstrated theoretically^{52–54} and experimentally.⁵⁵ The second purpose of the picket pulses is to facilitate simplified shock tuning and adiabat control.⁵⁶

The ramp times of the pickets and foot of the main drive are chosen as 400-ps linear ramps to account for a 350-ps spatiotemporal skew in the NIF beamlines that is introduced by the diffraction grating required for 1-D multi-FM SSD.⁵⁷ Shorter, more-intense pickets would more efficiently reduce laser imprint^{58–65} and provide increased adiabat shaping⁴⁸ for multidimensional stability, but such pickets are not currently possible on the NIF. The flattop of each picket pulse is also 400 ps, chosen to facilitate better SSD smoothing.^{57,66} This allows for a longer time when the laser pickets are at their highest power and while the beams fill the full aperture of the phase plates. The ramp time from the main drive to the spike pulse is, by design, 100 ps; however, 1-D simulations indicate that increasing the rise time to 400 ps (fixing the center of the rise in time) still gives full 1-D gain with the same $\text{ITF}_{1\text{-D}}$; i.e., no margin is lost.

The compression pulse launches four distinct shocks: one by each picket, one by the foot, and one by the ramp to main compression drive. As in previous designs with multiple

shocks,^{48,49,56} the shocks are tuned such that the shocks merge approximately at the rear surface of the solid DT fuel layer. The first picket pulse has a peak 96-beam (single-beam powers in parentheses) power of 6 TW (0.063 TW) and is followed by a second picket, which starts at 2.9 ns and has a peak power of 8 TW (0.083 TW). The foot of the main compression pulse is 15 TW (0.16 TW) beginning at 4.4 ns. Following the foot, the laser pulse rises beginning at $t = 5.8$ ns over 800 ps to a main compression power of 130 TW (1.35 TW). Finally, at $t = 8.95$ ns, the spike pulse begins, rising over 100 ps to 215 TW (2.24 TW). At the same time, the shock beams are turned on using the pulse history shown by the dashed curve, which also peaks at 215 TW (2.24 TW), giving a total system 192-beam peak power of 430 TW—17% below the recently demonstrated achieved peak power⁴² of 520 TW on the NIF. Since both the peak power and individual pulse energies of this design are significantly below the demonstrated capabilities of the NIF, this design offers substantial system headroom for capsule tuning to match experimental and simulated absorption, shell velocity, and spike shock pressure, as well as 2-D polar-drive symmetry.

The result is a mass-averaged in-flight fuel adiabat at the end of the compression drive of $\langle \alpha \rangle_{\text{fuel}} = 1.8$ with a minimum adiabat at the inner edge of the dense shell of $\alpha_{\text{in}} = 1.2$. The adiabat here is characterized using the “DT-standard” adiabat,⁴⁰ which is given by $\alpha_{\text{DT-standard}} = P/(2.18 \rho^{5/3})$, where P is in Mbar and ρ in g/cm^3 . The implosion velocity is $v_{\text{imp}} = 3.05 \times 10^7$ cm/s, which is substantially faster than Betti’s target of Ref. 2. The target achieves a 1-D gain of 58 with a peak areal density $\rho R = 1.6$ g/cm². The in-flight aspect ratio (defined as $\text{IFAR} \equiv R/\Delta R$, where R is the shell radius and ΔR is the shell thickness), calculated when the shell radius is two-thirds of the initial target radius, is 22. Target robustness is excellent with an $\text{ITF}_{1\text{-D}} = 4.1$. These 1-D performance parameters are summarized in Table 133.I.

The effect of the spike shock on target robustness was studied in 1-D by varying the spike laser intensity to alter the applied

Table 133.I: One-dimensional performance characteristics of the NIF shock-ignition design.

Gain	58
ρR (g/cm ²)	1.6
v_{imp} ($\mu\text{m/ns}$)	305
$\text{IFAR}_{2/3}$	22
Average adiabat	1.8
$\text{ITF}_{1\text{-D}}$	4.1

pressure of the spike shock. Figure 133.4 plots the calculated $\text{ITF}_{1\text{-D}}$ as a function of the initial shock pressure near the ablation surface. The nominal shock pressure of the original design is 300 Mbar. The lowest pressure in Fig. 133.4 corresponds to the case where the spike shock is removed entirely. In this case, the pressure reported (160 Mbar) is the ablation pressure. Figure 133.4 shows that this target is predicted to ignite in 1-D even without the spike shock, but with a much lower $\text{ITF}_{1\text{-D}}$ of 1.3. It also shows clearly that additional ignition margin is predicted when the spike pulse is present.

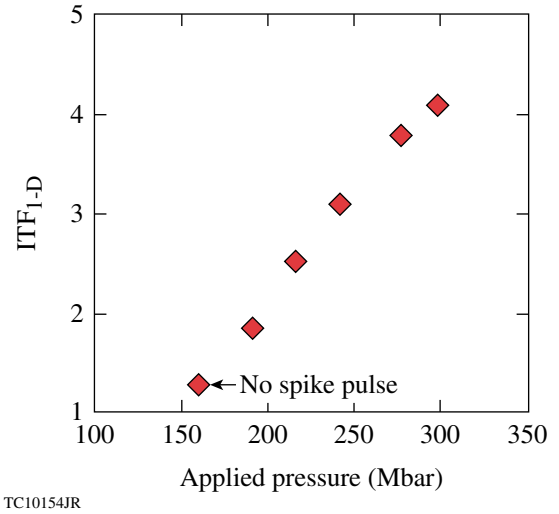
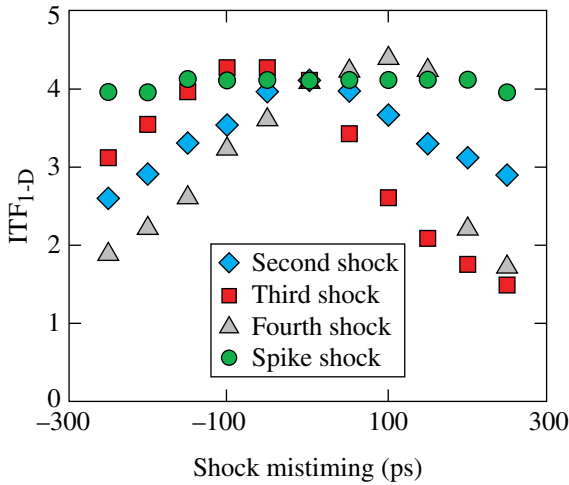


Figure 133.4 Plot of the $\text{ITF}_{1\text{-D}}$ versus the applied pressure in the spike shock. The lowest pressure point corresponds to the ablation pressure with no spike pulse. ITF: ignition threshold factor.

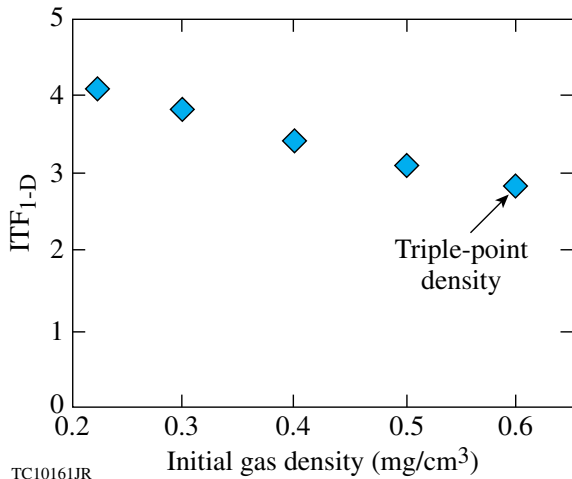
A series of 1-D simulations examined the robustness of the design to systematic mistiming of shocks. Figure 133.5 shows the calculated $\text{ITF}_{1\text{-D}}$ as a function of shock mistiming for the second shock (launched by the second picket), the third shock (launched by the foot of the main pulse), the fourth shock (launched by the ramp to the main compression drive), and the spike-pulse shock. As can be seen from the plots, the design ignites for all mistimings studied and has large timing windows within which a high margin is maintained. For reference, systematic shock mistiming on the NIF is estimated⁶⁷ to be 10 ps.

It is anticipated that such a target would be shot on the NIF at a temperature of 17.8 K, two degrees below the triple point of the DT fuel mixture with an initial gas density of 0.225 mg/cm³. Figure 133.6 illustrates how changing the initial gas density affects the $\text{ITF}_{1\text{-D}}$ in simulations. These data demonstrate the advantage of shooting at a lower temperature and gas density since the $\text{ITF}_{1\text{-D}}$ drops noticeably as the temperature



TC10414JR

Figure 133.5
Plot of the ITF_{1-D} versus shock mistiming for the 1-D capsule design.



TC10161JR

Figure 133.6
 ITF_{1-D} plotted versus the initial gas density in the target.

and gas density increase. It should be noted that the target is still predicted to ignite in 1-D at a gas density near the triple point ($T = 19.8$ K, $\rho_{\text{gas}} = 0.62$ mg/cm³) with an ITF_{1-D} of 2.8.

Since laser–plasma interactions can have a significant impact on ICF implosions, it is important to quantify the laser intensity, plasma temperature, and density scale lengths in the hot corona. Temporally and spatially averaged conditions at the quarter-critical surface are reported in Table 133.II during both the main compression pulse and the spike pulse. The laser intensities reported in this table are “nominal” in the sense that

Table 133.II: Average laser intensity $\langle I_{14} \rangle$ at the quarter-critical radius (units of 10^{14} W/cm²); average density gradient scale length $\langle L_n \rangle$ (μm); electron temperature T_e (keV); and the two-plasmon–decay hot-electron threshold F_{TPD} , calculated by Eq. (10). Values are reported during both the main-drive and spike pulses.

	Main drive	Spike
$\langle I_{14} \rangle$	8	34
$\langle L_n \rangle$ (μm)	350	450
T_e (keV)	3.5	8.5
F_{TPD}	3.5	7.8

they are averaged over the quarter-critical surface. Since the laser spots of the spike beams are much smaller ($1/e$ radius of 258 μm) compared to the average quarter-critical radius (~ 1000 μm), there will be hot spots of higher laser intensity in some locations.

From these plasma conditions, one can evaluate a two-plasmon–decay (TPD) threshold parameter F_{TPD} during both pulses using the formula⁶⁸

$$F_{\text{TPD}} = \frac{I_{14} L_n}{230 T_e}, \quad (10)$$

where I_{14} is the laser intensity in units of 10^{14} W/cm², L_n is the density gradient scale length in microns, and T_e is the electron temperature in keV. For values of F_{TPD} greater than 1, hot-electron heating from TPD has been reported in OMEGA experiments.^{69,70} The threshold parameter is predicted to be above 1 during both the main-drive and spike pulses, indicating a likelihood of hot-electron generation and preheating during both the compression and shock phases of the implosion. TPD thresholds for NIF targets have not yet been characterized, but thresholds for OMEGA targets have been shown to be dependent on beam geometry.⁷¹ Hot-electron generation during the main-drive pulse caused by TPD may be an issue for this target. If so, one mitigation strategy that has been proposed is the use of higher-Z ablaters, e.g., silicon or glass.^{70,72}

Given the high intensity of the spike pulse, and in light of recent shock-ignition–relevant experiments on OMEGA, it is predicted that during the spike pulse, stimulated Raman scattering (SRS), rather than TPD, will likely be the dominant factor in hot-electron generation.^{28,73,74} The SRS hot-electron temperature in those experiments was shown to be ~ 40 keV with a conversion efficiency of up to $\sim 16\%$ of the incident spike laser energy.

With this in mind, 1-D simulations of hot-electron energy coupling were performed in *LILAC* using a multigroup diffusion model of suprathermal electron energy transport. Various electron temperatures and coupling efficiencies were studied. The results, plotted in Fig. 133.7, show that this SI design is robust to energy coupling from hot electrons with Maxwellian temperatures of up to 150 keV and coupling efficiencies of up to 30%, similar to the results of Ref. 30. Furthermore, an analysis of *LILAC* simulations at hot-electron temperatures above 100 keV suggests a competition between increased shock coupling as a result of the lower-energy hot electrons stopping at the ablation front and volumetric heating of the cold fuel caused by higher-energy hot electrons streaming through the target, increasing the shell adiabat and lowering compressibility. These two effects oppose one another: one to improve target performance, the other to degrade performance. A more-rigorous model of suprathermal electrons is required to more-accurately quantify the effects of hot-electron transport at temperatures above 150 keV.

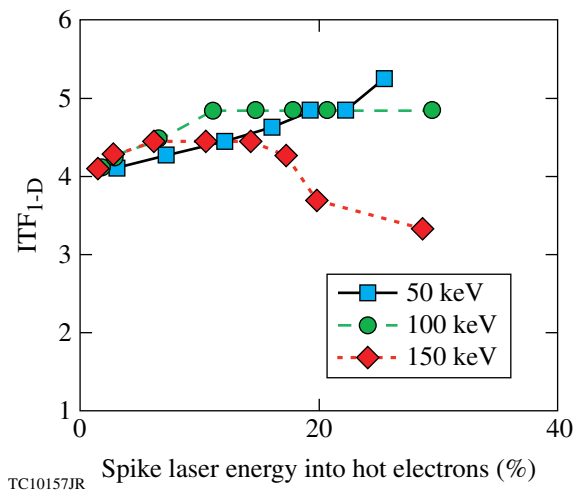


Figure 133.7
ITF_{1-D} plotted with various levels of hot-electron energy coupling during the spike pulse. Energy coupling is varied for different hot-electron temperatures and generation efficiency as a percentage of the spike laser energy.

Two-Dimensional Polar-Drive Configuration and Nonuniformity Studies

Because of the current indirect-drive laser configuration on the NIF, in which the laser beams are clustered near the poles for entry into a vertically oriented hohlraum, it is necessary to devise a scheme that will directly drive a capsule uniformly to preserve shell integrity and hot-spot confinement. Simply pointing all the NIF beams with equal power toward the center of the capsule will result in higher intensities at the poles than at the equator. As such, the equator of the target would be driven

at a slower velocity than the poles, resulting in an unacceptable target asymmetry. In polar drive (PD), beams from the poles and mid-latitudes of the target chamber are deliberately pointed toward the equator of the target to correct for the lower drive intensity there. Hot-spot polar-drive targets have shown promise in both simulations^{75–78} and experiments.^{79,80} While other schemes have been devised in which no repointing is deemed necessary¹⁸ or in which an equatorial ring is used to redirect laser energy toward the equator,^{80,81} they are not investigated in this article.

As mentioned earlier, substantial margin can be regained for SI designs on the NIF by using two separate laser pulses—one to drive the compression and one to shock the capsule. For SI-specific purposes, two separate PD beam-configuration types have been proposed. NIF beams are bundled into groups of four termed “quads.” The first and simplest PD scheme to implement on the NIF is one where half of the NIF’s 48 quads drive the capsule compression and the other half drive the ignitor shock. The other scheme divides the beams within a single quad, using two beams from each of the 48 NIF quads for the compression and the remaining two beams for the shock. Here, we will use the term “full-quad” for the first scheme and “split-quad” for the second. It should be noted that the split-quad scheme requires modifications to the front end of the NIF Laser System to allow different laser pulses to propagate through separate beamlines within a single quad;⁸² therefore, the full-quad scheme is more likely to be used in the near term. However, since much work has been done on PD designs of standard hot-spot capsules for the NIF using 48-quad beam pointings,^{75–77} this article focuses mainly on polar-drive SI using 48 split quads as compression beams to capitalize on lessons learned in a similar beam geometry. Initial results from full-quad, polar-drive SI are also presented.

Modeling the laser deposition computationally in either scheme requires a fully 3-D ray trace. All 2-D PD simulations in this article were performed using the arbitrary Lagrangian–Eulerian radiation–hydrodynamics code *DRACO*.^{39,76} In designing a PD pointing scheme for a specific target, one may use different laser spot shapes and sizes, as well as vary the pulse power from quad to quad until the desired shell uniformity is achieved. The NIF is currently capable of providing separate laser pulse shapes to each quad, and phase plates can be designed to produce specified laser spot shapes and sizes.

A specific split-quad beam-pointing scheme was developed for the compression beams wherein the 48 half-quads, which can be divided into five separate “rings” of beams with the

same port angle, were repointed toward five separate latitudes on the target surface. The beam repointings are summarized in Table 133.III. In this table, the beam port angle describes the location at which the beams enter the target chamber, relative to pole, and the repointing angle on target represents the polar-angle position of the center of the beam on the target surface. All the beams located at the 23.5° and 30° port angles are repointed to the target surface at 24.5° and 44°, respectively, both toward the target equator, and are referred to as Ring 1 and Ring 2 in Table 133.III. Half of the 44.5° quads (Ring 3) are repointed slightly toward the pole to the 44° target angle, and the other half (Ring 4) to the 82° position. Finally, the 50° quads (Ring 5) are all pointed to 82° on target.

Table 133.III: Split-quad polar-drive (PD) beam-repointing angles for the main-drive beams given by beam port location.

	Beam port angle (°)	Repointing angle on target (°)
Ring 1	23.5	24.5
Ring 2	30.0	44.0
Ring 3	44.5	44.0
Ring 4	44.5	82.0
Ring 5	50.0	82.0

In addition, laser-spot profiles for the drive beams were altered from the 1-D spot shapes to better distribute laser absorption and achieve better capsule uniformity and performance. The first alteration is to use a lower super-Gaussian order, reducing it from $\sigma = 2.5$ in the 1-D design to $\sigma = 2.2$. This removes much of the short-wavelength nonuniformity in the absorption. Next, a secondary elliptical spot is superimposed over the circular spots of Rings 4 and 5. This secondary ellipse has an amplitude of 30% relative to the circular spot, an ellipticity of 2.5 with its major axis oriented in the same plane as the target’s equator, a super-Gaussian order $\sigma = 2.2$, and is offset relative to the center of the circular spot by 30% of the initial target radius toward the target’s equator. The addition of this secondary ellipse directs more energy toward the equator. Finally, this spot redesign also uses a spot masking that effectively redistributes back onto target laser energy that would otherwise be lost over the target horizon as a result of the beam repointing. This is done at time $t = 0$ for all beams; however, the beam profile is modified only slightly in the polar and mid-latitude beams because of their more-moderate repointing angles. The resulting beam profiles are shown in Fig. 133.8.

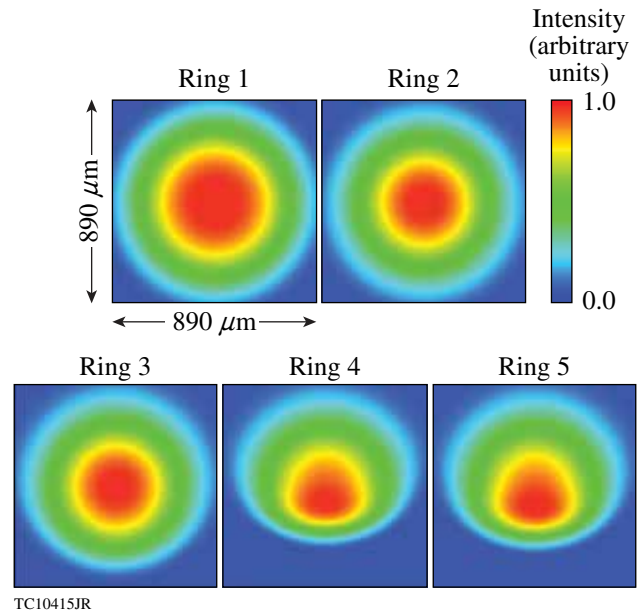


Figure 133.8

Laser-spot profiles for the split-quad polar-drive (PD) design. Laser intensity is plotted in arbitrary units with respect to position. Each box is approximately 890 μm square.

Finally, the beam powers of each ring are optimized to produce a more-uniform implosion. The beam power versus time for each ring is plotted in Fig. 133.9, along with the 1-D design pulse (black dashed line). The beams from Ring 1 are grouped together using a single laser pulse shape and are labeled the “polar.” The Ring-2 and Ring-3 beams share a second pulse shape and are labeled the “mid-latitude” beams. The Ring-4 and Ring-5 beams comprise the final grouping (“equatorial”

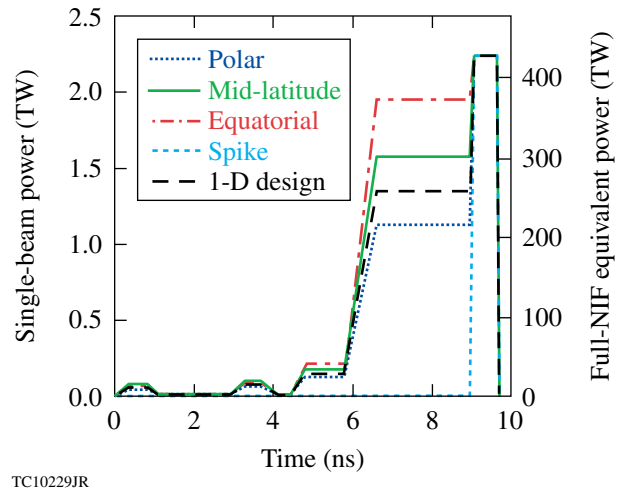


Figure 133.9

Laser pulse shapes for the split-quad PD design for each grouping of beams.

beams), all using a third pulse shape. Initial polar-drive SI simulations indicated that the final capsule symmetry is much more dependent on the compression-beam geometry than the spike-beam geometry. As such, in this design, no repointing of the shock beams in the remaining 48 half-quads was done to minimize refractive losses. The spike-beam profiles, therefore, are circular with the same super-Gaussian order $\sigma = 2.2$ as the main-drive beams. Since symmetry is largely unaffected by the spike beams, each ignitor beam has a pulse shape exactly as in 1-D for all rings, as is shown in Fig. 133.9.

This 2-D PD design uses a total of 760 kJ of laser energy. Additional input laser energy compared to the 689 kJ of the 1-D design is required to offset the enhanced refractive losses of the repointed beams caused by their higher impact parameters as well as the loss in ablative drive efficiency in those same beams as a result of the ray turning points and the position of peak absorption lying farther away from the ablation front. The maximum laser energy in any single beam is 7.4 kJ. For reference, the NIF is rated at 1.8 MJ (9.4 kJ per beam) and has already demonstrated this energy level. The simulated target density and temperature profiles at peak compression, shortly before the onset of ignition, are shown in Fig. 133.10. This target achieves a 2-D simulated gain of 52.

Recently, comparisons between OMEGA experimental data and 1-D simulations have indicated the need for implementing a numerical model of nonlocal heat transport combined with a

model of cross-beam energy transfer (CBET)⁸³ due to stimulated Brillouin scattering. While nonlocal effects and CBET are anticipated to affect laser coupling and symmetry in this target to some extent, both the nonlocal transport⁸⁴ and CBET⁸⁵ models developed recently for *DRACO* in 2-D were being tested at the time of this publication. Therefore, these simulations all use flux-limited Spitzer heat transport with a flux-limiter value of 0.06 with no cross-beam model. Given that this target design is well below the energy and power limits of the NIF, it may be possible to recover lost energy coupling caused by CBET by increasing laser power and energy. Symmetry can likewise be recovered by tuning in future simulations with the added physics packages and through experiment.

Several robustness studies were performed on this PD design to evaluate the additional contributions to compression nonuniformity caused by both capsule asymmetries and laser system uncertainties. Unless otherwise specified, these simulations were performed in a half-sphere geometry and include all even perturbation modes from $\ell = 2$ to $\ell = 50$ with a minimum grid resolution of 12 cells per smallest-wavelength mode in the transverse direction. Capsule asymmetry studies include outer-surface roughness of the plastic ablator, inner-shell-surface roughness from DT ice layering, as well as target offset due to mispositioning of the target relative to the center of beam convergence. Modeled laser system uncertainties include random beam-mispointing errors, beam-to-beam mistiming of the laser pulse, power imbalance between beams, and laser speckle and imprint from the phase plates, including beam smoothing using multi-FM SSD. Each of the capsule nonuniformity sources has been characterized experimentally in NIF-scale or OMEGA-scale capsules, and laser system uncertainty⁶⁸ on the NIF is well quantified.

Robustness to capsule nonuniformities was found to exceed NIF specifications and achieved values. Each of the following sources of nonuniformity was added to the PD capsule design individually and varied in magnitude to assess the capsule's sensitivity to the perturbation source: capsule outer-surface roughness, inner-surface DT-ice roughness, target offset from target chamber center (TCC), beam-to-beam mispointing and mistiming, and laser power balance between beams. Note that root-mean-square (rms) values in laser parameters are not systematic variations from the design specifications, but rather indicate statistical deviations of individual beams from the intended design.

Outer-surface roughness on NIF-scale capsules has been quantified as 115-nm rms with a spectrum approximated by the

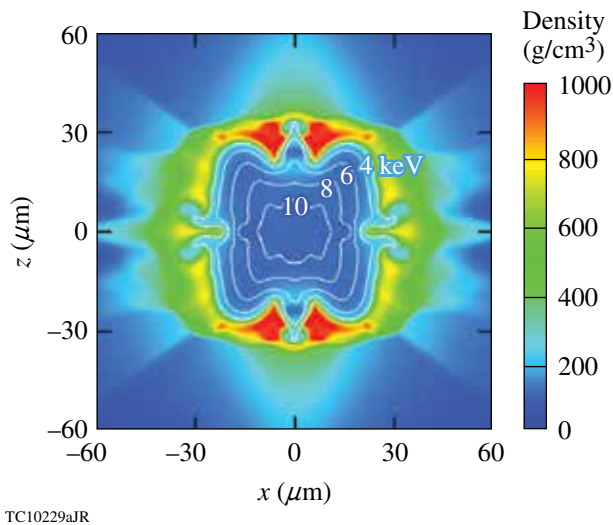


Figure 133.10
Simulated density contour plot of the 2-D split-quad PD design at the onset of ignition. Temperature contours are plotted with white lines. The target gain is 52.

formula given in Eq. (2) of Ref. 86. Simulations of this polar-drive SI design with this outer-surface roughness spectrum indicate that the target can withstand outer-surface roughness up to $5\times$ this NIF specification, or up to 575-nm rms, and still achieve ignition. The NIF specification for the inner DT-ice surface roughness is $1\text{-}\mu\text{m}$ rms, and cryogenic DT-layered OMEGA capsules have routinely demonstrated this level of uniformity.⁸⁷ These simulations indicate that the SI design tolerates over $5\text{-}\mu\text{m}$ -rms inner-surface ice roughness. Target offset was modeled in a full-sphere geometry, resolving modes $\ell = 1$ to $\ell = 50$. This capsule ignited with a target offset of up to $25\ \mu\text{m}$ — $2.5\times$ greater than the NIF specification of $10\ \mu\text{m}$. Figure 133.11 shows the predicted density and temperature profiles for this $25\text{-}\mu\text{m}$ -offset implosion. One can see that the hot spot has been pushed away from the capsule’s original position, and that the hot-spot displacement is in the same direction as the initial target offset from TCC. This is expected as a result of the increased laser intensity on the side of the capsule closer to TCC. With a $25\text{-}\mu\text{m}$ offset, the gain of this target is 56.

Robustness to laser system uncertainties likewise exceed NIF specifications with ignition indicated for beam-mispointing errors up to $100\text{-}\mu\text{m}$ rms and beam-to-beam mistiming up to 100-ps rms [for comparison, the NIF specifications are $50\text{-}\mu\text{m}$ mispointing and 30-ps mistiming (see Ref. 67)]. The NIF has demonstrated 8% rms quad-to-quad power imbalance,

corresponding to a 2% rms illumination nonuniformity on target (see Ref. 67). In a split-quad beam configuration, care should be taken when pairing beams within a quad, given that the power output of beams within a quad varies significantly. This variation is systematic, however, due to a design variation in the thickness of the frequency-conversion crystals and can be minimized in a split-quad configuration by consistently choosing the same beams in each of the drive quads. Therefore, effectively for this target design, the NIF-specified power imbalance between half-quads is $\sim 11\%$ rms, a factor of $\sqrt{2}$ higher due to the fact that half of the NIF beams are used. Simulations indicate that the SI target will ignite with power imbalance up to 15% rms between half-quads.

A full nonuniformity simulation including all of these sources of nonuniformity at the NIF specifications was performed. This simulation included expected levels of laser imprint on the NIF caused by phase-plate speckle with the multi-FM-SSD smoothing parameters used in Ref. 77. This simulation, which was performed on a full sphere and resolved modes from $\ell = 1$ to $\ell = 100$, indicated a target gain of 38.

As mentioned earlier, SI with a full-quad PD beam configuration is more likely to be fielded on the NIF in the near term. Therefore, a full-quad PD beam configuration for the same capsule design has been developed. As in Ref. 88, all four quads from the 30° beams (Ring 1) and half of the quads from the 44.5° and 50° beams (Rings 2 and 3, respectively) are used for the main compression drive, while the other quads are used for the ignitor shock pulse. The main-drive beams are repointed as outlined in Table 133.IV. Each of these three rings of beams has a separate laser pulse-shape history. The pulse shapes for each ring are detailed in Fig. 133.12, with the 1-D design pulse shown for reference by the dashed line. Ring 1 comprises the polar beams, Ring 2 the mid-latitude beams, and Ring 3 the equatorial beams. As with the split-quad design, no repointing was considered for the shock beams, and the pulse shape is the same as the 1-D design. Simulations of this target design indicate a gain of 51. A density and temperature plot at the onset of ignition (Fig. 133.13) shows that the target exhibits

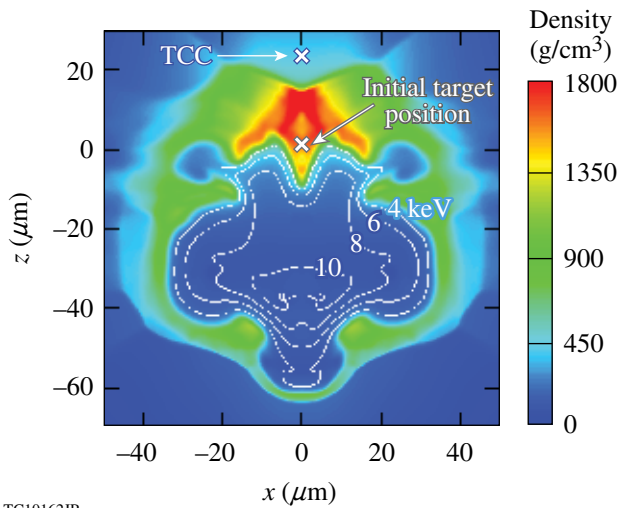


Figure 133.11 Simulated density contour plot of the 2-D split-quad PD design with an initial $25\text{-}\mu\text{m}$ target offset. The plot is shown at the onset of ignition. Temperature contours are plotted with white lines. For reference, the position of the target chamber center (TCC) and the initial target position are indicated. The target gain is 56.

Table 133.IV: Full-quad PD beam-repointing angles for the main-drive beams given by beam port location.

Beam port angle ($^\circ$)	Repointing angle on target ($^\circ$)
30.0	25.0
44.5	59.0
50.0	85.0

similar shell integrity compared to the split-quad design shown in Fig. 133.10.

Further optimization and robustness studies on this full-quad design are underway. Beam configurations that offer different repointings of beams within a single quad, as in Ref. 88, are also being considered to improve drive symmetry. Simulations with the nonlocal heat transport and CBET models must be performed, and an accounting for laser backscatter caused by LPI should be included. In addition, hot-electron

preheat effects must be modeled in the 2-D simulations. It is also anticipated that 3-D effects will be somewhat larger in the full-quad design than in the split-quad design because of the smaller number of azimuthal beam ports used during compression, and, as such, 3-D PD simulations must be performed in the future.

Conclusion

A polar-drive SI design for the National Ignition Facility has been developed within the NIF Laser System specifications. The target implosion velocity is higher than for standard SI designs to account for laser power limitations on the NIF. The proposed target ignites in 1-D simulations with an ITF_{1-D} of 4.1 using 700 kJ of input laser energy. Excellent robustness in 1-D to shock mistiming and initial gas density is predicted. Hot-electron energy coupling during the spike pulse is shown to have a positive effect on target margin at hot-electron temperatures up to 150 keV and below 20% of the incident spike laser energy.

Two-dimensional PD simulations including a 3-D laser ray-trace modeling of NIF beams and using either a split-quad or a full-quad beam configuration predict good shell uniformity and ignition with gains above 50 using 750 kJ of laser energy. PD target robustness has been shown to be excellent with respect to individual nonuniformity sources. Simulations of the split-quad PD design including all anticipated levels of system uncertainty and capsule and laser nonuniformity predict a gain of 38.

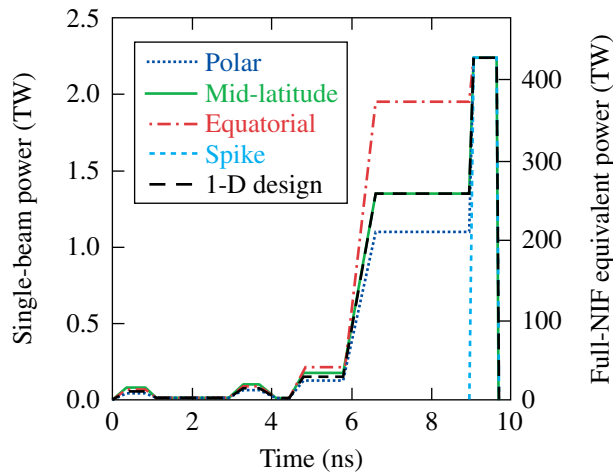
This target may be imploded on the NIF using the proposed full-quad PD beam configuration in a relatively short time frame, requiring only minor modifications to the NIF system. These modifications include the incorporation of 1-D multi-FM SSD beam smoothing, the manufacture of specially tailored laser phase plates, the introduction of polarization plates for polarization smoothing, and the development of a PD target insertion cryostat.

ACKNOWLEDGMENT

The authors thank L. J. Perkins, A. J. Schmitt, X. Ribeyre, and S. Atzeni for many enlightening discussions. This work was supported by the U.S. Department of Energy Office of Inertial Confinement Fusion under Cooperative Agreement Nos. DE-FC52-08NA28302 and DE-FC02-04ER54789, the University of Rochester, and the New York State Energy Research and Development Authority. The support of DOE does not constitute an endorsement by DOE of the views expressed in this article.

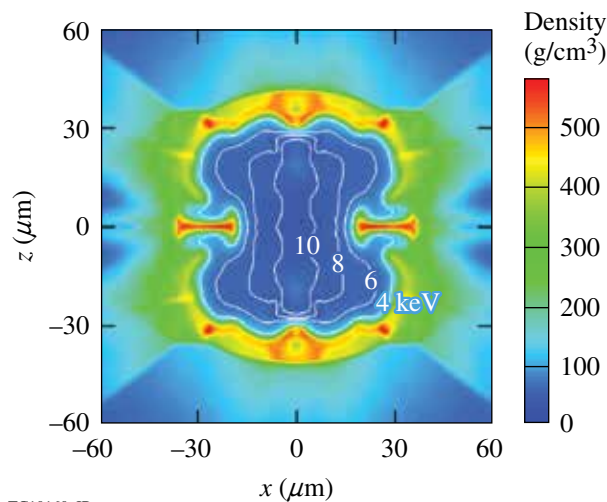
REFERENCES

1. S. Atzeni and J. Meyer-ter-Vehn, *The Physics of Inertial Fusion: Beam Plasma Interaction, Hydrodynamics, Hot Dense Matter*, International Series of Monographs on Physics (Clarendon Press, Oxford, 2004).



TC10160JR

Figure 133.12
Laser pulse shapes for the full-quad PD design for each grouping of beams.



TC10160aJR

Figure 133.13
Simulated density contour plot of the 2-D full-quad PD design at the onset of ignition. Temperature contours are plotted with white lines. The target gain is 51.

2. R. Betti, C. D. Zhou, K. S. Anderson, L. J. Perkins, W. Theobald, and A. A. Solodov, *Phys. Rev. Lett.* **98**, 155001 (2007).
3. N. G. Basov, S. Yu. Gus'kov, and L. P. Feokistov, *J. Sov. Laser Res.* **13**, 396 (1992).
4. M. Tabak *et al.*, *Phys. Plasmas* **1**, 1626 (1994).
5. V. A. Shcherbakov, *Sov. J. Plasma Phys.* **9**, 240 (1983).
6. V. A. Shcherbakov, presented at the XXXII Conference on Plasma Physics and CF, Zvenigorod, Moscow, 14–18 February 2005.
7. M. Lafon, X. Ribeyre, and G. Schurtz, *Phys. Plasmas* **17**, 052704 (2010).
8. G. Schurtz, X. Ribeyre, and M. Lafon, *J. Phys.: Conf. Ser.* **244**, 022013 (2010).
9. R. Nora and R. Betti, *Phys. Plasmas* **18**, 082710 (2011).
10. X. Ribeyre, V. T. Tikhonchuk, J. Breil, M. Lafon, and E. Le Bel, *Phys. Plasmas* **18**, 102702 (2011).
11. L. J. Perkins, R. Betti, K. N. LaFortune, and W. H. Williams, *Phys. Rev. Lett.* **103**, 045004 (2009).
12. X. Ribeyre, M. Lafon, G. Schurtz, M. Olazabal-Loume, J. Breil, S. Galera, and S. Weber, *Plasma Phys. Control. Fusion* **51**, 124030 (2009).
13. A. J. Schmitt, J. W. Bates, S. P. Obenschain, S. T. Zalesak, D. E. Fyfe, and R. Betti, *Fusion Sci. Technol.* **56**, 377 (2009).
14. A. J. Schmitt *et al.*, *Phys. Plasmas* **17**, 042701 (2010).
15. J. W. Bates *et al.*, *High Energy Density Phys.* **6**, 128 (2010).
16. B. Canaud and M. Temporal, *New J. Phys.* **12**, 043037 (2010).
17. S. Atzeni *et al.*, *Nucl. Fusion* **49**, 055008 (2009).
18. X. Ribeyre *et al.*, *Plasma Phys. Control. Fusion* **51**, 015013 (2009).
19. M. Temporal *et al.*, *Plasma Phys. Control. Fusion* **53**, 124008 (2011).
20. S. Atzeni, A. Schiavi, and A. Marocchino, *Plasma Phys. Control. Fusion* **53**, 035010 (2011).
21. M. Hohenberger, W. Theobald, S. X. Hu, K. S. Anderson, R. Betti, T. R. Boehly, A. Casner, D. E. Fratanduono, M. Lafon, D. D. Meyerhofer, R. Nora, X. Ribeyre, T. C. Sangster, G. Schurtz, W. Seka, C. Stoeckl, and B. Yaakobi, "Shock-Ignition Experiments with Planar Targets on OMEGA," submitted to *Physical Review Letters*.
22. R. Florido, R. C. Mancini, T. Nagayama, R. Tommasini, J. A. Delettrez, S. P. Regan, and B. Yaakobi, *Rev. Sci. Instrum.* **81**, 10E307 (2010).
23. W. Theobald, R. Betti, C. Stoeckl, K. S. Anderson, J. A. Delettrez, V. Yu. Glebov, V. N. Goncharov, F. J. Marshall, D. N. Maywar, R. L. McCrory, D. D. Meyerhofer, P. B. Radha, T. C. Sangster, W. Seka, D. Shvarts, V. A. Smalyuk, A. A. Solodov, B. Yaakobi, C. D. Zhou, J. A. Frenje, C. K. Li, F. H. Séguin, R. D. Petrasso, and L. J. Perkins, *Phys. Plasmas* **15**, 056306 (2008).
24. T. R. Boehly, D. L. Brown, R. S. Craxton, R. L. Keck, J. P. Knauer, J. H. Kelly, T. J. Kessler, S. A. Kumpan, S. J. Loucks, S. A. Letzring, F. J. Marshall, R. L. McCrory, S. F. B. Morse, W. Seka, J. M. Soures, and C. P. Verdon, *Opt. Commun.* **133**, 495 (1997).
25. O. Klimo *et al.*, *Phys. Plasmas* **18**, 082709 (2011).
26. O. Klimo *et al.*, *Plasma Phys. Control. Fusion* **52**, 055013 (2010).
27. W. Theobald, K. S. Anderson, R. Betti, R. S. Craxton, J. A. Delettrez, J. A. Frenje, V. Yu. Glebov, O. V. Gotchev, J. H. Kelly, C. K. Li, A. J. Mackinnon, F. J. Marshall, R. L. McCrory, D. D. Meyerhofer, J. F. Myatt, P. A. Norreys, P. M. Nilson, P. K. Patel, R. D. Petrasso, P. B. Radha, C. Ren, T. C. Sangster, W. Seka, V. A. Smalyuk, A. A. Solodov, R. B. Stephens, C. Stoeckl, and B. Yaakobi, *Plasma Phys. Control. Fusion* **51**, 124052 (2009).
28. W. Theobald, R. Nora, M. Lafon, A. Casner, X. Ribeyre, K. S. Anderson, R. Betti, J. A. Delettrez, J. A. Frenje, V. Yu. Glebov, O. V. Gotchev, M. Hohenberger, S. X. Hu, F. J. Marshall, D. D. Meyerhofer, T. C. Sangster, G. Schurtz, W. Seka, V. A. Smalyuk, C. Stoeckl, and B. Yaakobi, *Phys. Plasmas* **19**, 102706 (2012).
29. S. Depierreux, C. Goyon, K. Lewis, H. Bandulet, D. T. Michel, G. Loisel, V. Yahia, V. Tassin, C. Stenz, N. G. Borisenko, W. Nazarov, J. Limpouch, P. E. Masson Laborde, P. Loiseau, M. Casanova, Ph. Nicolaï, S. Hüller, D. Pesme, C. Riconda, V. T. Tikhonchuk, and C. Labaune, *Plasma Phys. Control. Fusion* **53**, 124034 (2011).
30. R. Betti, W. Theobald, C. D. Zhou, K. S. Anderson, P. W. McKenty, S. Skupsky, D. Shvarts, V. N. Goncharov, J. A. Delettrez, P. B. Radha, T. C. Sangster, C. Stoeckl, and D. D. Meyerhofer, *J. Phys., Conf. Ser.* **112**, 022024 (2008).
31. G. H. Miller, E. I. Moses, and C. R. Wuest, *Opt. Eng.* **43**, 2841 (2004).
32. *LLE Review Quarterly Report* **33**, 1, Laboratory for Laser Energetics, University of Rochester, Rochester, NY, LLE Document No. DOE/DP/40200-65, NTIS Order No. DE88008065 (1987). (Copies may be obtained from the National Technical Information Service, Springfield, VA 22161.)
33. Y. Kato *et al.*, *Phys. Rev. Lett.* **53**, 1057 (1984).
34. *LLE Review Quarterly Report* **114**, 73, Laboratory for Laser Energetics, University of Rochester, Rochester, NY, LLE Document No. DOE/NA/28302-826, OSTI ID 93524 (2008).
35. S. Skupsky, R. W. Short, T. Kessler, R. S. Craxton, S. Letzring, and J. M. Soures, *J. Appl. Phys.* **66**, 3456 (1989).
36. D. S. Clark, S. W. Haan, and J. D. Salmonson, *Phys. Plasmas* **15**, 056305 (2008).
37. P. Y. Chang, R. Betti, B. K. Spears, K. S. Anderson, J. Edwards, M. Fatenejad, J. D. Lindl, R. L. McCrory, R. Nora, and D. Shvarts, *Phys. Rev. Lett.* **104**, 135002 (2010).
38. B. K. Spears *et al.*, *Phys. Plasmas* **19**, 056316 (2012).
39. P. B. Radha, V. N. Goncharov, T. J. B. Collins, J. A. Delettrez, Y. Elbaz, V. Yu. Glebov, R. L. Keck, D. E. Keller, J. P. Knauer, J. A. Marozas, F. J.

- Marshall, P. W. McKenty, D. D. Meyerhofer, S. P. Regan, T. C. Sangster, D. Shvarts, S. Skupsky, Y. Srebro, R. P. J. Town, and C. Stoeckl, *Phys. Plasmas* **12**, 032702 (2005).
40. R. Betti, K. Anderson, V. N. Goncharov, R. L. McCrory, D. D. Meyerhofer, S. Skupsky, and R. P. J. Town, *Phys. Plasmas* **9**, 2277 (2002).
 41. C. D. Zhou and R. Betti, *Phys. Plasmas* **14**, 072703 (2007).
 42. J. Kline, *Bull. Am. Phys. Soc.* **57**, 200 (2012).
 43. J. Delettrez and E. B. Goldman, Laboratory for Laser Energetics, University of Rochester, Rochester, NY, LLE Report No. 36 (1976).
 44. B. I. Bennett *et al.*, Los Alamos National Laboratory, Los Alamos, NM, Report LA-7130 (1978).
 45. R. C. Malone, R. L. McCrory, and R. L. Morse, *Phys. Rev. Lett.* **34**, 721 (1975).
 46. V. N. Goncharov, J. P. Knauer, P. W. McKenty, P. B. Radha, T. C. Sangster, S. Skupsky, R. Betti, R. L. McCrory, and D. D. Meyerhofer, *Phys. Plasmas* **10**, 1906 (2003).
 47. K. Anderson and R. Betti, *Phys. Plasmas* **10**, 4448 (2003).
 48. K. Anderson and R. Betti, *Phys. Plasmas* **11**, 5 (2004).
 49. R. Betti, K. Anderson, J. Knauer, T. J. B. Collins, R. L. McCrory, P. W. McKenty, and S. Skupsky, *Phys. Plasmas* **12**, 042703 (2005).
 50. Lord Rayleigh, in *Scientific Papers* (Cambridge University Press, Cambridge, England, 1900), Vol. II, pp. 200–207.
 51. G. Taylor, *Proc. R. Soc. London Ser. A* **201**, 192 (1950).
 52. S. E. Bodner, *Phys. Rev. Lett.* **33**, 761 (1974).
 53. H. Takabe *et al.*, *Phys. Fluids* **28**, 3676 (1985).
 54. R. Betti, V. N. Goncharov, R. L. McCrory, and C. P. Verdon, *Phys. Plasmas* **5**, 1446 (1998).
 55. J. P. Knauer, K. Anderson, R. Betti, T. J. B. Collins, V. N. Goncharov, P. W. McKenty, D. D. Meyerhofer, P. B. Radha, S. P. Regan, T. C. Sangster, V. A. Smalyuk, J. A. Frenje, C. K. Li, R. D. Petrasso, and F. H. Séguin, *Phys. Plasmas* **12**, 056306 (2005).
 56. V. N. Goncharov, T. C. Sangster, T. R. Boehly, S. X. Hu, I. V. Igumenshchev, F. J. Marshall, R. L. McCrory, D. D. Meyerhofer, P. B. Radha, W. Seka, S. Skupsky, C. Stoeckl, D. T. Casey, J. A. Frenje, and R. D. Petrasso, *Phys. Rev. Lett.* **104**, 165001 (2010).
 57. J. A. Marozas, J. D. Zuegel, and T. J. B. Collins, *Bull. Am. Phys. Soc.* **55**, 294 (2010).
 58. N. Metzler, A. L. Velikovich, and J. H. Gardner, *Phys. Plasmas* **6**, 3283 (1999).
 59. N. Metzler *et al.*, *Phys. Plasmas* **9**, 5050 (2002).
 60. N. Metzler *et al.*, *Phys. Plasmas* **10**, 1897 (2003).
 61. T. J. B. Collins and S. Skupsky, *Phys. Plasmas* **9**, 275 (2002).
 62. T. J. B. Collins, J. P. Knauer, R. Betti, T. R. Boehly, J. A. Delettrez, V. N. Goncharov, D. D. Meyerhofer, P. W. McKenty, S. Skupsky, and R. P. J. Town, *Phys. Plasmas* **11**, 1569 (2004).
 63. A. B. Iskakov *et al.*, *Phys. Rev. E* **61**, 842 (2000).
 64. E. Krouský *et al.*, *Laser Part. Beams* **18**, 87 (2000).
 65. V. A. Smalyuk, V. N. Goncharov, K. S. Anderson, R. Betti, R. S. Craxton, J. A. Delettrez, D. D. Meyerhofer, S. P. Regan, and T. C. Sangster, *Phys. Plasmas* **14**, 032702 (2007).
 66. J. A. Marozas, LLE, private communication (2012).
 67. C. J. Stolz, *Phil. Trans. R. Soc. Lond. A* **370**, 4115 (2012).
 68. A. Simon, R. W. Short, E. A. Williams, and T. Dewandre, *Phys. Fluids* **26**, 3107 (1983).
 69. W. Seka, D. H. Edgell, J. P. Knauer, J. F. Myatt, A. V. Maximov, R. W. Short, T. C. Sangster, C. Stoeckl, R. E. Bahr, R. S. Craxton, J. A. Delettrez, V. N. Goncharov, I. V. Igumenshchev, and D. Shvarts, *Phys. Plasmas* **15**, 056312 (2008).
 70. W. Seka, D. H. Edgell, J. F. Myatt, A. V. Maximov, R. W. Short, V. N. Goncharov, and H. A. Baldis, *Phys. Plasmas* **16**, 052701 (2009).
 71. D. T. Michel, A. V. Maximov, R. W. Short, S. X. Hu, J. F. Myatt, W. Seka, A. A. Solodov, B. Yaakobi, and D. H. Froula, *Phys. Rev. Lett.* **109**, 155007 (2012).
 72. J. F. Myatt, J. Zhang, V. N. Goncharov, A. V. Maximov, R. W. Short, D. F. DuBois, D. A. Russell, and H. X. Vu, *Bull. Am. Phys. Soc.* **57**, 299 (2012).
 73. C. Riconda *et al.*, *Phys. Plasmas* **18**, 092701 (2011).
 74. S. Weber *et al.*, *Phys. Rev. E* **85**, 016403 (2012).
 75. S. Skupsky, J. A. Marozas, R. S. Craxton, R. Betti, T. J. B. Collins, J. A. Delettrez, V. N. Goncharov, P. W. McKenty, P. B. Radha, T. R. Boehly, J. P. Knauer, F. J. Marshall, D. R. Harding, J. D. Kilkenny, D. D. Meyerhofer, T. C. Sangster, and R. L. McCrory, *Phys. Plasmas* **11**, 2763 (2004).
 76. J. A. Marozas, F. J. Marshall, R. S. Craxton, I. V. Igumenshchev, S. Skupsky, M. J. Bonino, T. J. B. Collins, R. Epstein, V. Yu. Glebov, D. Jacobs-Perkins, J. P. Knauer, R. L. McCrory, P. W. McKenty, D. D. Meyerhofer, S. G. Noyes, P. B. Radha, T. C. Sangster, W. Seka, and V. A. Smalyuk, *Phys. Plasmas* **13**, 056311 (2006).
 77. T. J. B. Collins, J. A. Marozas, K. S. Anderson, R. Betti, R. S. Craxton, J. A. Delettrez, V. N. Goncharov, D. R. Harding, F. J. Marshall, R. L. McCrory, D. D. Meyerhofer, P. W. McKenty, P. B. Radha, A. Shvydky, S. Skupsky, and J. D. Zuegel, *Phys. Plasmas* **19**, 056308 (2012).
 78. A. M. Cok, R. S. Craxton, and P. W. McKenty, *Phys. Plasmas* **15**, 082705 (2008).

79. F. J. Marshall, R. S. Craxton, M. J. Bonino, R. Epstein, V. Yu. Glebov, D. Jacobs-Perkins, J. P. Knauer, J. A. Marozas, P. W. McKenty, S. G. Noyes, P. B. Radha, W. Seka, S. Skupsky, and V. A. Smalyuk, *J. Phys. IV France* **133**, 153 (2006).
80. R. S. Craxton, F. J. Marshall, M. J. Bonino, R. Epstein, P. W. McKenty, S. Skupsky, J. A. Delettrez, I. V. Igumenshchev, D. W. Jacobs-Perkins, J. P. Knauer, J. A. Marozas, P. B. Radha, and W. Seka, *Phys. Plasmas* **12**, 056304 (2005).
81. R. S. Craxton and D. W. Jacobs-Perkins, *Phys. Rev. Lett.* **94**, 095002 (2005).
82. L. J. Perkins, LLNL, private communication (2011).
83. I. V. Igumenshchev, W. Seka, D. H. Edgell, D. T. Michel, D. H. Froula, V. N. Goncharov, R. S. Craxton, L. Divol, R. Epstein, R. Follett, J. H. Kelly, T. Z. Kosc, A. V. Maximov, R. L. McCrory, D. D. Meyerhofer, P. Michel, J. F. Myatt, T. C. Sangster, A. Shvydky, S. Skupsky, and C. Stoeckl, *Phys. Plasmas* **19**, 056314 (2012).
84. G. A. Moses, LANL, private communication (2012).
85. J. A. Marozas and T. J. B. Collins, *Bull. Am. Phys. Soc.* **57**, 344 (2012).
86. P. W. McKenty, V. N. Goncharov, R. P. J. Town, S. Skupsky, R. Betti, and R. L. McCrory, *Phys. Plasmas* **8**, 2315 (2001).
87. T. C. Sangster, R. Betti, R. S. Craxton, J. A. Delettrez, D. H. Edgell, L. M. Elasky, V. Yu. Glebov, V. N. Goncharov, D. R. Harding, D. Jacobs-Perkins, R. Janezic, R. L. Keck, J. P. Knauer, S. J. Loucks, L. D. Lund, F. J. Marshall, R. L. McCrory, P. W. McKenty, D. D. Meyerhofer, P. B. Radha, S. P. Regan, W. Seka, W. T. Shmayda, S. Skupsky, V. A. Smalyuk, J. M. Soures, C. Stoeckl, B. Yaakobi, J. A. Frenje, C. K. Li, R. D. Petrasso, F. H. Séguin, J. D. Moody, J. A. Atherton, B. D. MacGowan, J. D.ilkenny, T. P. Bernat, and D. S. Montgomery, *Phys. Plasmas* **14**, 058101 (2007).
88. L. Tucker, *2010 Summer Research Program for High School Juniors at the University of Rochester's Laboratory for Laser Energetics*, University of Rochester, Rochester, NY, LLE Report No. 365, LLE Document No. DOE/NA/28302-1000 (2011).

Polar-Drive Implosions on OMEGA and the National Ignition Facility

Introduction

Polar drive (PD)¹ provides the capability to perform direct-drive-ignition experiments on laser facilities like the National Ignition Facility (NIF)² when cylindrically but not spherically configured for x-ray drive. Beams are absent near the equator in the x-ray drive configuration (Fig. 133.14). As a result, beams must be repointed to adequately irradiate the equator. This repointing of the beams results in oblique beams, which in turn result in laser energy deposition farther from the ablation surface, and consequently reduced kinetic energy of the imploding shell. Ignition designs^{3,4} compensate for this reduced hydrodynamic efficiency (defined as the ratio of the maximum shell kinetic energy to the laser energy) by increasing the energy of the most-oblique beams. To achieve adequate uniformity locally near the equator, these designs use beam profiles that include a skewed ellipse for the most-oblique beams. The combination of beam pointing, higher energies for the equatorial beams, and the skewed elliptical beam profiles results in nonradial (or lateral) gradients of the deposited laser energy and the temperature in the corona. Departures from the model predictions of deposited laser energy and lateral heat flow can play an important role in determining the symmetry of the

implosion. The goal of OMEGA and early NIF experiments is to develop and validate ignition-relevant models of laser deposition and heat conduction.

Several aspects of PD are similar to symmetrically driven direct-drive implosions. In the latter, beams are located around the target with spherical symmetry and irradiate the capsule more normally. In these schemes, the implosion velocity V_{imp} , defined as the maximum shell velocity, and the adiabat α_{inn} , defined as the ratio of the pressure to the Fermi-degenerate pressure averaged over the mass density that forms the high-density shell, are the most important parameters. The minimum energy for ignition E_{min} scales as⁵

$$E_{\text{min}} \text{ (kJ)} = 50.8 \alpha_{\text{min}}^{1.88} \left(\frac{V_{\text{imp}}}{3 \times 10^7 \text{ cm/s}} \right)^{-5.89} \left(\frac{P}{100 \text{ Mbar}} \right)^{-0.77},$$

where P is the ablation pressure. For both symmetric and polar drive, it is critical to achieve the designed implosion velocity while also setting the shell on the required adiabat. The implosion velocity and adiabat are primarily determined by one-dimensional (1-D) physics. The additional challenge in polar drive is multidimensional; it is necessary to adequately compensate for reduced energy coupling at the equator while achieving the required values of the adiabat and implosion velocity. Hydrodynamic simulations⁴ suggest that this compensation is achievable. The parameter space of adiabat and implosion velocity over which ignition is possible, including multidimensional effects, is therefore the same between the two direct-drive schemes.

Short-wavelength nonuniformities result from the imprinting of single-beam nonuniformities on the target. Subsequent multidimensional growth caused by the Rayleigh–Taylor (RT) instability⁶ influences the stability of the converging shell. Significant RT growth can degrade implosion performance. Since the number of e foldings of the most-dangerous mode to RT instability depends on the implosion velocity and details of the adiabat profile in the converging shell,⁷ which is very

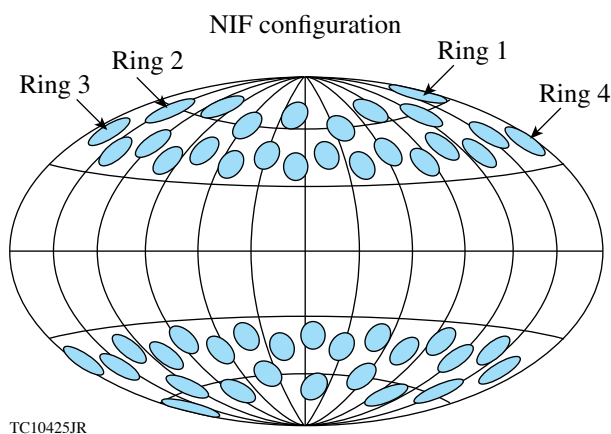


Figure 133.14
The NIF beam-port configuration arranged in four rings.

similar between PD and symmetric drive, short-wavelength behavior is very similar between the two schemes. Therefore, symmetric-drive implosions on OMEGA^{8–10} play an important role in validating models of laser imprint and RT growth that are also relevant for PD.

Polar drive differs from symmetric drive in the seeds that determine the low-mode asymmetry of the imploding shell and the hot spot. Beam geometry has a marginal influence on target symmetry and performance in symmetric drive. In PD, however, beam obliquity changes the angular and radial locations of the deposited laser energy. This influences the symmetry of the imploding shell. Seeds for long-wavelength nonuniformity are set throughout the laser pulse. Figure 133.15 shows the contours of laser energy deposited normalized to the volume as a function of radial location and polar angle for a NIF ignition design.⁴ Two aspects are unique to polar drive. The conduction zone (the distance between the ablation surface and the peak in deposited energy) is larger near the equator than at the pole, leading to lower hydrodynamic efficiency near the equator. There are significant transverse gradients in the deposited energy primarily because of the unique beam profiles and the higher power in the equatorial beams. These lateral gradients are insignificant in the symmetric design. Modeling this lateral heat flow is critical for an accurate prediction of symmetry in polar drive.

Shock nonuniformity is another important determinant of shell asymmetry. Long-wavelength shock-front perturbations, determined primarily by polar variations in the laser deposition [Fig. 133.16(a)], seed the nonuniformities on the inner shell surface [Fig. 133.16(b)]. The shocks shown in Fig. 133.16 are from an OMEGA-scale design with deliberate repointing

and mistiming to illustrate the seeding of perturbations at the rear shell surface. These perturbations grow when subsequent shocks reach the surface. Inner shell perturbations also grow as a result of the feedthrough of perturbations being seeded at the ablation surface determined by polar variations in laser-energy deposition and heat conduction. Accurate predictions of symmetry rely on accurate modeling of laser deposition and heat conduction.

Laser–plasma interactions (LPI’s) can compromise target performance by reducing implosion velocity, altering symmetry, and preheating the cold shell. Incorporating LPI effects within fluid codes is challenging because of the different length and time scales over which plasmas and fluids evolve. Empirical guidance is critical to understanding the magnitude of the effects of LPI processes and in improving designs to mitigate their deleterious effects. The goal of the early NIF experiments is to understand issues relating to energetics, symmetry, and preheat in NIF-scale plasmas.

In the following sections, OMEGA PD experiments are discussed with emphasis on adiabat and symmetry. The implosion velocity has been discussed in previous work.¹¹ Next, limitations of OMEGA experiments and early experiments planned for the NIF are discussed, followed by the conclusions.

OMEGA Experiments

The goal of OMEGA experiments is to predictably model target performance in polar drive. Twenty of the 60 OMEGA beams are omitted from the drive to emulate the 48-quad NIF x-ray-drive configuration [Fig. 133.17(a)].¹² The beams are then shifted toward the equator to directly drive the target more symmetrically. The 40 OMEGA beams can be considered to

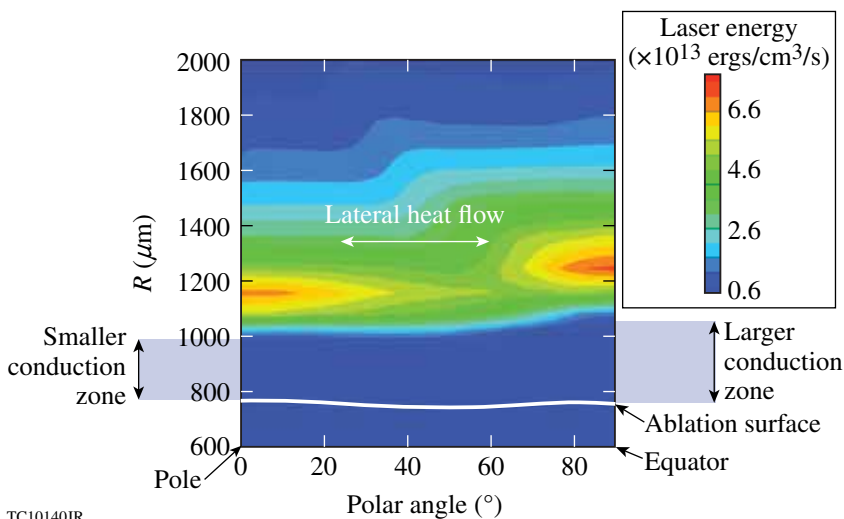


Figure 133.15

Density of laser energy deposited at the end of the laser pulse ($t = 9.0$ ns) for a NIF ignition design versus polar angle. The white line shows the location of the ablation surface. The conduction zone is larger at the equator, leading to reduced hydrodynamic efficiency. A significant transverse gradient in the deposited laser energy leads to transverse heat flow in polar drive.

TC10140JR

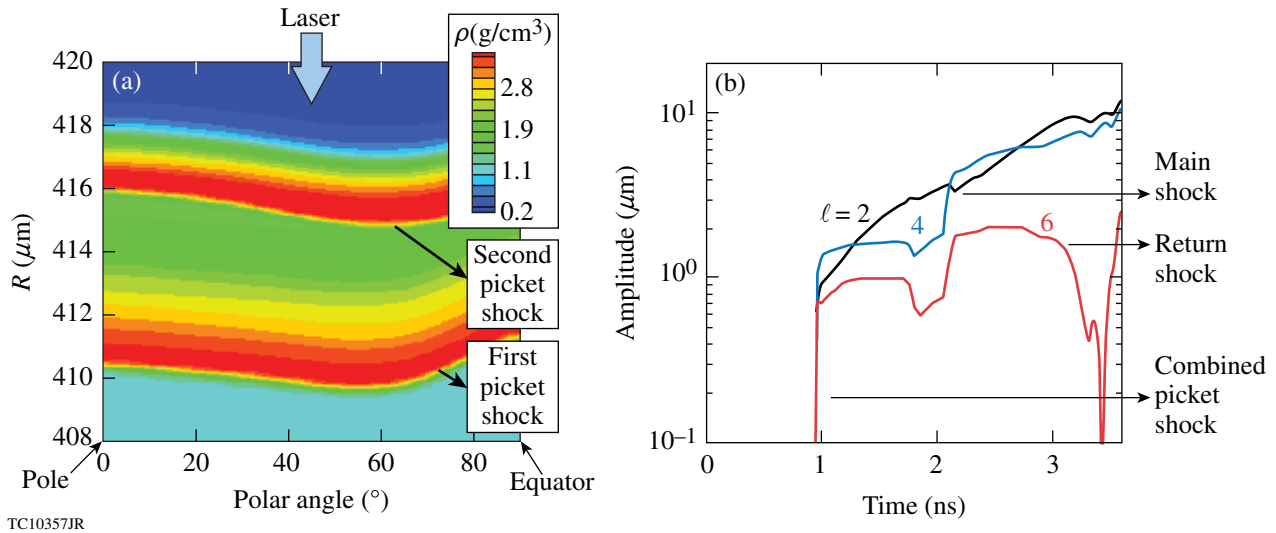


Figure 133.16

(a) Density contours at 650 ps showing nonuniform shocks from the first two pickets transiting the shell for an OMEGA PD design. (b) Perturbation amplitude at the rear shell surface is seeded by the shocks. Feedthrough from the ablation surface results in amplitude growth during acceleration and convergence (until 3 ns).

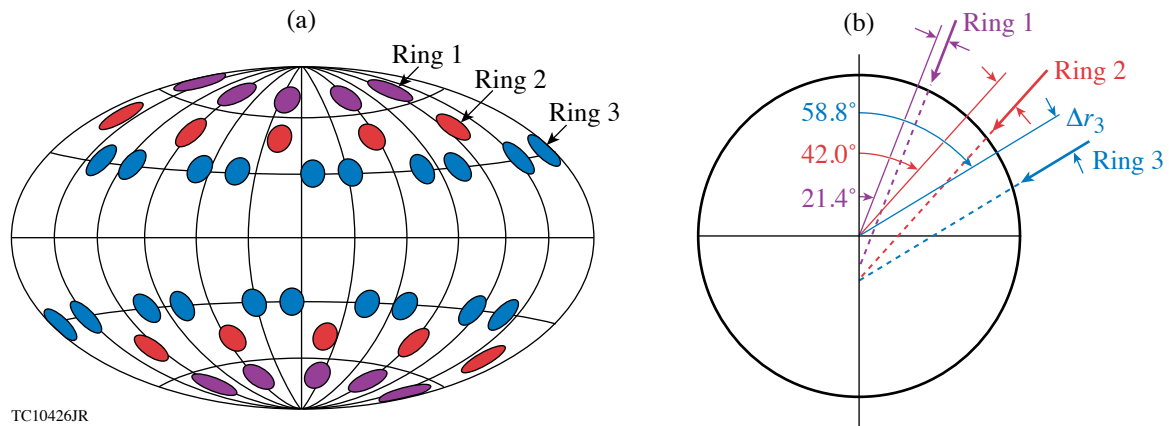


Figure 133.17

(a) The OMEGA beam port configuration with the equatorial beams omitted. There are three rings in each hemisphere. (b) Schematic showing the shifted beams for OMEGA PD geometry.

be arranged in three rings. Each ring is repointed only in polar angle by a distance Δr perpendicular to the beam axis (the azimuthal angles for OMEGA are already optimally pointed) [see Fig. 133.17(b)]. Each repointed configuration is characterized by three numbers $\{\Delta r_1, \Delta r_2, \Delta r_3\}$; larger values of these numbers correspond to more-oblique beams. Room-temperature experiments on OMEGA employ a 24- to 27- μm -thick plastic (CH) shell with 10 atm of deuterium (D_2) fill [see Fig. 133.18(a)]. Since 40 of the 60 beams are used, the energy on target is limited to approximately 13.5 kJ. (In principle, nearly 16 kJ can be obtained for PD implosions—these highest-energy implosions are reserved for cryogenic capsules.) A variety of laser pulse

shapes, with different temporal histories, irradiate the target. A flat foot to a continuous rise¹² [Fig. 133.18(b)] and three pickets preceding a main pulse are used^{11,13} [Fig. 133.18(c)]. The PD ignition design uses the latter pulse shape since nearly 1-D high areal densities have been demonstrated with this pulse shape in symmetric drive.¹⁴ In the room-temperature CH designs, both of these pulse shapes set the shell at a minimum adiabat of approximately 3.5. The continuous pulse shape irradiates the target at a higher peak intensity of $8 \times 10^{14} \text{ W/cm}^2$, while the triple-picket pulse irradiates the target at $4 \times 10^{14} \text{ W/cm}^2$ (these values are defined at the initial target radius). The advantage of the triple-picket pulse shape is the ability to achieve

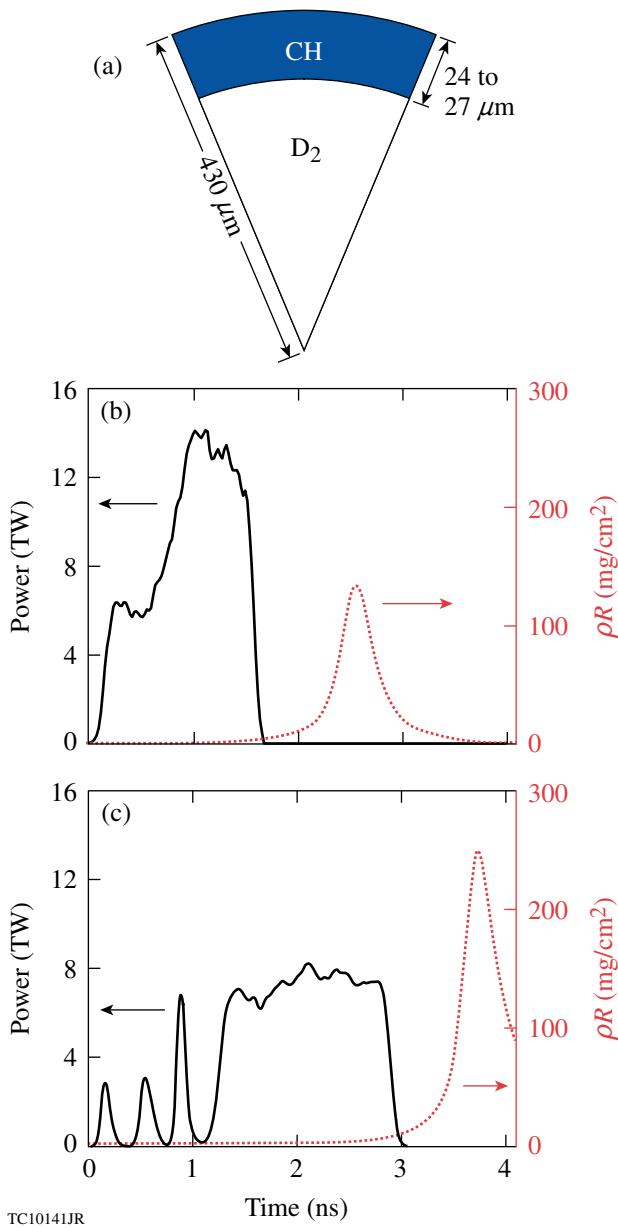


Figure 133.18
 (a) Schematic of the target used in PD implosion experiments on OMEGA. [(b) and (c)] Laser pulse (left axis) and simulated areal density averaged over the polar angle (right axis) for (b) the continuous pulse shape and (c) the triple-picket pulse shape.

higher convergence as explained below. Full beam smoothing (1/3-THz three-color-cycle smoothing by spectral dispersion¹⁵ and polarization smoothing¹⁶) is used. The implosion velocity of these capsules is approximately 2×10^7 cm/s. Higher velocities can be obtained in cryogenic implosions where the lower-density deuterium–tritium (DT) layer permits thicker shells and technically feasible spacing between the pickets for less-massive targets.¹¹ Target performance is studied from

measurements of areal density (ρR) and x-ray images obtained by backlighting the converging shell using a subset of the beams omitted from the drive. Other measures of target performance such as yield, neutron rate history, and the related implosion velocity have been presented elsewhere.¹¹

The predicted areal densities for the two pulse shapes discussed in this work differ quite significantly. The triple-picket pulse maintains the drive pressure until the shock is reflected from the center of the converging capsule, whereas the continuous pulse permits the shell to coast and decompress, reducing the areal density. Figure 133.19 shows the mass density and adiabat profile for the two pulse shapes at the end of the laser

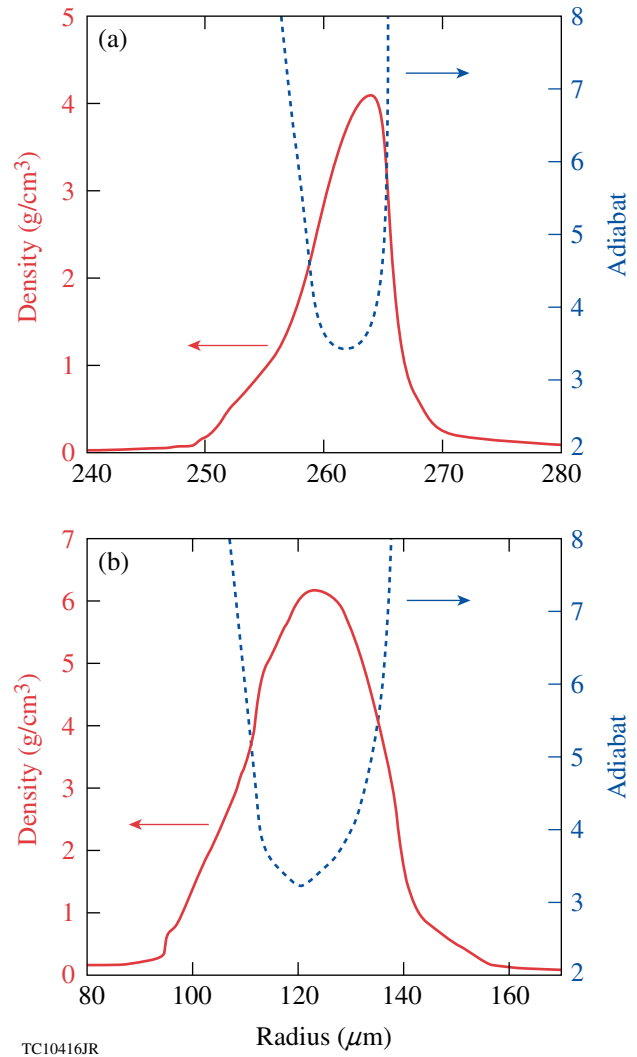


Figure 133.19
 Mass-density profile at the end of the laser pulse (left axis) and adiabat profile in the converging shell (right axis) for (a) the continuous pulse shape and (b) the triple-picket pulse shape.

pulse; while the adiabat profiles are very similar, the shell has traveled a greater distance for the triple-picket pulse shape. At peak neutron production, the shell in the implosion driven with the triple-picket pulse is simulated to have higher convergence (the convergence ratio is $CR \sim 19$ compared to $CR \sim 13$ for the continuous laser pulse) and to have a higher density than the shell driven with the continuous pulse shape.

The areal density is inferred in implosion experiments through the energy loss of secondary protons¹⁷ and is inferred only during neutron production. To compare the areal density from simulations with that inferred from observations, it is important to account for the observed neutron production history.⁸ Figure 133.20(a) shows the measured and simulated rates

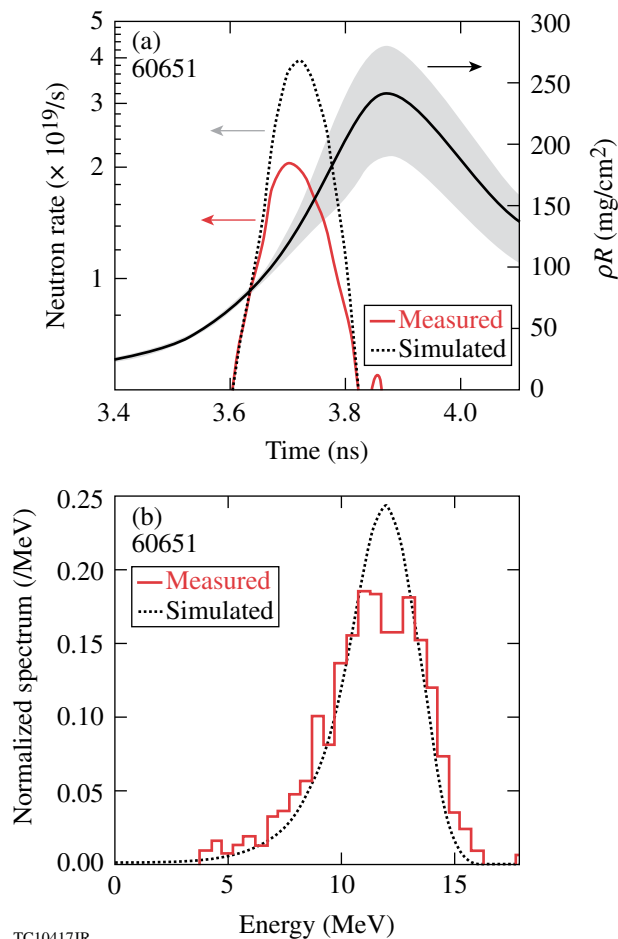


Figure 133.20
 (a) Simulated neutron rate (dotted line, left axis) overlaid on the measured neutron rate (red line, left axis), and the polar-angle averaged areal-density history (solid line, right axis). The shaded region indicates the minimum and maximum areal density in polar angle. (b) Measured (solid) and simulated (dotted) secondary proton spectrum.

for neutron history overlaid with the areal-density evolution for a PD implosion driven with a triple-picket pulse shape and beam repointing corresponding to $\{90 \mu m, 150 \mu m, 150 \mu m\}$. The simulations were performed with the hydrodynamic code *DRACO*¹⁸ including a full 3-D laser ray trace,¹⁹ collisional absorption as the only laser-energy deposition mechanism, a flux-limited heat-conduction model (with a flux limiter $f = 0.06$) (Refs. 20 and 21), and multigroup diffusive radiation transport with astrophysical opacity tables. The experimental neutron rate history is measured using the neutron temporal diagnostic.²² The *DRACO*-simulated profiles are post-processed with the particle-tracking code *IRIS*²³ using this measured rate history to calculate the emergent proton spectrum. Excellent agreement is obtained in the spectrum, as seen in Fig. 133.20(b), indicating that the adiabat is modeled well for this pulse shape. The areal density from the continuous pulse shape has been published previously.¹¹ The trend across pulse shapes is recovered experimentally as seen in Fig. 133.21. For an implosion with no coasting phase, the maximum areal density has been shown to depend primarily on the adiabat²⁴ as $\rho R_{max} (mg/cm^2) = [2.6 \times 10^2 E_L^{1/3} (kJ)] / \alpha_{inn}^{0.6}$, where E_L is the laser energy. Simulations reproduce the areal density for both pulse shapes, indicating that *DRACO* accurately models shock timing and the effect of coasting on compression. This result is consistent with independent PD shock-timing measurements using cone-in-shell geometries.¹³

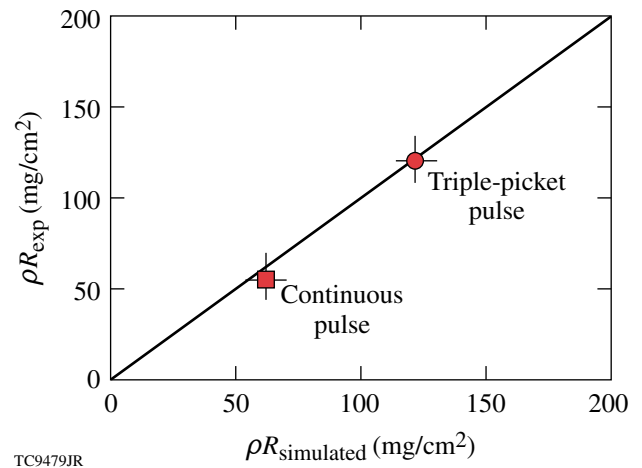


Figure 133.21
 Inferred areal density compared to simulated values for the continuous and triple-picket pulse shapes. The vertical error bars represent the standard deviation of the four areal-density measurements around the target chamber center for each shot. The horizontal error bars represent the standard deviation of the inferred areal density in polar angle from the simulated spectra.

Backlit images indicate that simulations reproduce the gross features of the converging shell. Figure 133.22 shows the images obtained by backlighting the converging shell with an ~ 4.7 -keV Ti backlighter for two different pointing configurations, corresponding to $\{90 \mu\text{m}, 150 \mu\text{m}, 150 \mu\text{m}\}$ and $\{30 \mu\text{m}, 150 \mu\text{m}, 150 \mu\text{m}\}$, for the triple-picket pulse shape. *DRACO* simulations are post-processed with the code *Spect3D*,²⁵ which transports x rays through the *DRACO* profiles accounting for absorption using opacities generated by the PRISM group.²⁵ The plasma is assumed to be in local thermodynamic equilibrium (LTE), which is an excellent assumption for the densities (from solid up to $\sim 150 \text{ g/cm}^3$) and temperatures (from $\sim \text{eV}$ up to $\sim \text{keV}$) characteristic in the compressing capsule. The detector resolution and the time window over which the images are integrated in the experiment are included in the postprocessing. The simulations reproduce the measured images very well. The images shown in Fig. 133.22 correspond to the latest time at

which the shell can be unambiguously viewed. At this time the shell has converged by approximately a factor of 5. Later in time the backlighter intensity is significantly lower than the self-emission from the compressed core, precluding an inference of the symmetry. For the first pointing configuration, the converging shell is prolate, for which one can correct by repointing Ring 1 closer to the pole. The second pointing configuration achieves a rounder core as seen in the images. The contour of maximum x-ray absorption (white line in Fig. 133.22) is decomposed into Legendre modes ℓ . The normalized mode amplitudes (defined as the ratio of the mode amplitude to the radius of maximum absorption) for $\ell = 2$ to 10 are in reasonable agreement between simulation and measurement. The typical error in the amplitude measurement is estimated to be of the order of 2% to 3%. The best observed uniformity with only repointing to correct for PD geometry has been obtained with the $\{30 \mu\text{m}, 150 \mu\text{m}, 150 \mu\text{m}\}$ configuration.

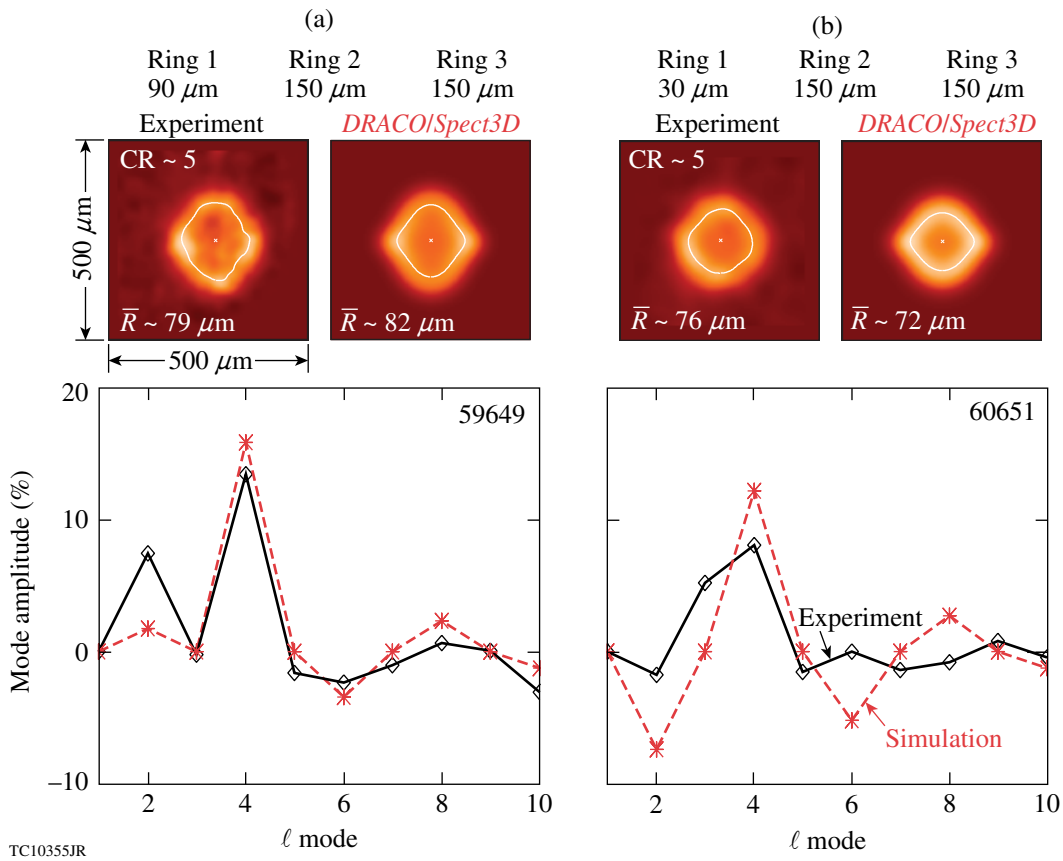


Figure 133.22

(a) Backlit image from the experiment together with the simulated image for the triple-picket pulse shape. The white lines indicate the contour of maximum absorption. The graphs show experimental and simulated normalized Legendre-mode amplitudes (the ratio of mode amplitude to average radius \bar{R}) of the contour of maximum absorption. (b) Same as (a) but for a different pointing that reduces the amplitude of the $\ell = 2$ Legendre mode.

Experimental and simulated backlit images for the two different pulse shapes for the same pointing configuration $\{90 \mu\text{m}, 120 \mu\text{m}, 120 \mu\text{m}\}$ are compared for the continuous pulse shape [Fig. 133.23(a)] and the triple-picket pulse shape [Fig. 133.23(b)]. With this pointing configuration there is an observable difference in the shape of the core for the two pulse shapes, which is reproduced by simulation. Excellent agreement is obtained in the modal amplitudes of the shell perturbations.

Current high-convergence OMEGA PD implosions can only be driven at low intensities owing to the limited energy available from 40 beams combined with the fixed spot size produced by OMEGA's existing phase plates (860 μm diameter corresponding to 95% of the energy enclosed).²⁶ Higher on-target intensities can be obtained with smaller targets and phase plates with smaller focal spots.¹¹ New phase plates have been obtained for the OMEGA laser, and experiments to study PD implosions at ignition-relevant intensities will begin in the near future.

NIF ignition targets have a radius that is nearly $4\times$ the radius of OMEGA-scale targets. Consequently, the density scale lengths in the corona of NIF targets are larger by the same ratio. As discussed in the next section, laser-plasma interactions become increasingly important to target performance for larger scale lengths. Experiments at the NIF scale are critical to understanding the role of these interactions on target performance.

Early NIF Experiments

The radial coronal density scale length in typical NIF ignition designs⁴ is $\sim 600 \mu\text{m}$, compared to the OMEGA-scale density scale length of $\sim 150 \mu\text{m}$. The magnitude of LPI effects typically increases with scale length. LPI can influence shell adiabat,²⁷ energetics,²⁸ and symmetry.²⁹ Two-plasmon decay (TPD)³⁰ primarily determines the extent of fast-electron pre-heat in implosions. Energetic electrons, accelerated by plasma waves, deposit their energy in the cold shell, raising its adiabat,

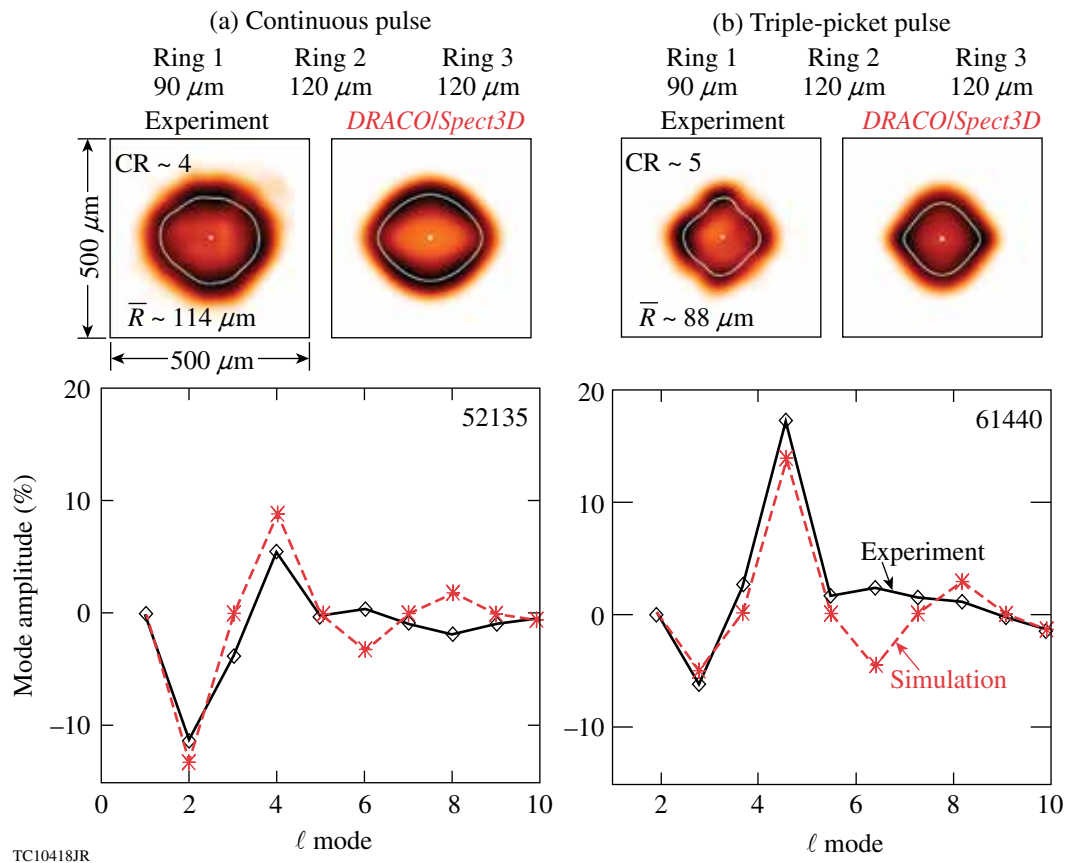


Figure 133.23

Experimental and simulated backlit images for the same pointing $\{90 \mu\text{m}, 120 \mu\text{m}, 120 \mu\text{m}\}$ but for the two different pulse shapes: (a) the high-intensity continuous pulse shape and (b) low-intensity triple-picket pulse shape. The white line indicates the contour of maximum absorption. The graphs show normalized Legendre-mode amplitudes (the ratio of mode amplitude to average radius \bar{R}) of the contour of maximum absorption.

making it more difficult to achieve the required compression. The extent of preheat is typically diagnosed by measuring energetic (“hard”) x rays (≥ 50 keV) produced by fast electrons.³¹ The threshold parameter for the TPD instability, defined as $\eta = I_{n/4} (10^{14} \text{ W/cm}^2) L_{n/4} (\mu\text{m}) / 233 T_{n/4}^e (\text{keV})$ (Ref. 30), where $I_{n/4}$, $L_{n/4}$, and $T_{n/4}^e$ are the laser intensity, density scale length, and the electron temperature at the quarter-critical surface, respectively, has been shown to correlate with the observed hard x-ray signal in OMEGA symmetric-drive implosions.³² However, the effect of this preheat on target performance in ignition-relevant OMEGA implosions is negligible.³³ The longer NIF scale lengths are suggestive of a higher threshold parameter and greater preheat from fast electrons; however, no clear physical mechanism links the threshold parameter to the observed hard x-ray signal. The threshold parameter has been defined in planar geometry for the absolute instability. TPD has also been shown to be convectively unstable³⁴ for the plasma conditions and profiles in direct-drive implosions, and this aspect is not included in the threshold parameter. Additionally, calculations of TPD indicate that this instability can become highly nonlinear and saturate.³⁵ Without detailed modeling of TPD, observations of hard x rays on the NIF are necessary to determine the extent of preheat.

In cross-beam energy transfer (CBET), incoming rays transfer their energy to outgoing rays through ion-acoustic waves.²⁸ This results in reduced laser-energy deposition and reduced hydrodynamic efficiency. The gain rate for CBET is $L^{-1} \sim (I_1 I_2) / [\nu_a^2 \eta^2 + (1 - \eta^2)^2]$ (Ref. 28), where I_1 and I_2 are the intensities of the two beamlets, ν_a is the damping rate of the ion-acoustic waves, and $\eta = \mathbf{k}_a \cdot \mathbf{u} - \omega_a / k_a c_a$ (the resonance condition where \mathbf{k}_a is the ion-acoustic wave vector, \mathbf{u} the fluid velocity, ω_a the ion-acoustic wave frequency, and c_a the ion-acoustic wave speed). Irradiating capsules with the relevant intensities (I_1 and I_2) is critical to understanding CBET effects. CBET reduces implosion velocity by $\sim 10\%$ in symmetric-drive OMEGA-scale implosions.²⁸ PD implosions indicate a reduced implosion velocity although the exact mechanism is not yet understood.¹¹ As presented earlier, however, symmetry in PD implosions is reproduced well with simulations that do not include CBET. This may be caused by either the negligible effect of CBET on symmetry in OMEGA-scale implosions or the relatively early time when the converging shell is viewed. When velocity scale lengths are long, as in the NIF-scale coronal plasma, the resonance condition for CBET is satisfied over a larger volume. This likely results in a greater level of CBET. NIF experiments are again important in identifying the extent of CBET.

Room-temperature CH implosions are planned for initial NIF experiments [Fig. 133.24(a)]. The first set of experiments are planned at lower intensities where LPI effects such as TPD and CBET are less important, enabling one to validate models in *DRACO* that do not contain these LPI effects. Future experiments will probe higher-intensity implosions to develop and validate models in that regime and identify mitigating strategies if required. To obtain the scale of the initial set of implosions, consider the scaling law $E \sim R_t^3$, which retains the same laser energy density per target volume, where E is the laser energy and R_t is the target radius. Using OMEGA energies of 25 kJ

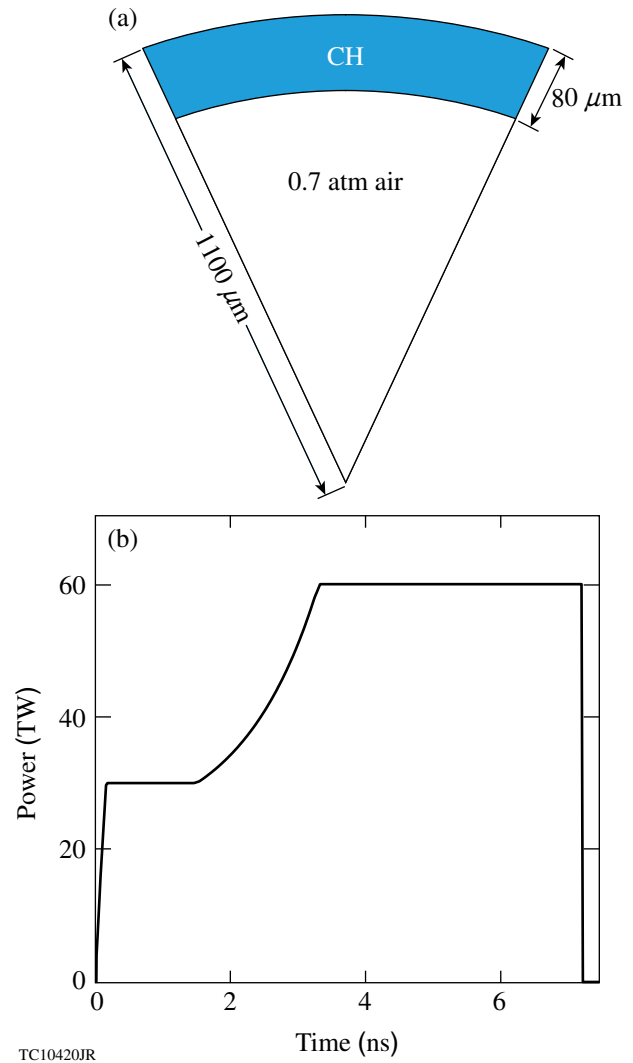


Figure 133.24

(a) Schematic of the target for early NIF experiments; (b) pulse shape from the 1-D design.

and the desired target radius of $\sim 1100 \mu\text{m}$ (this is determined by the NIF phase plates³⁶), these implosions must be driven with $\sim 350 \text{ kJ}$. Using $P \sim R_t^2$ yields a peak power of $P \sim 50 \text{ TW}$ and $T \sim R_t$ yields a pulse length of $T \sim 7.5 \text{ ns}$. The laser pulse shape [Fig. 133.24(b)]—a low foot to a continuous rise, similar to the OMEGA pulse shape described earlier—sets the target at a low adiabat of ~ 3 . These early experiments will use the existing NIF hardware including phase plates and single-beam smoothing. Beams are defocused³⁷ to achieve the optimal symmetry in the simulation. Beam phase fronts for the near field³⁶ are forward propagated using Fourier transforms to obtain the on-target beam shapes using the code *Waasikwa*.³⁸ The laser-related parameters of the design are shown in Table 133.V. In this reprinted configuration, some quads (a set of four beams form a quad) from the 44.5° cone are moved to 46° , while others are moved to 69° . Beams are repointed in azimuth to locations defined in Ref. 4. While this achieves excellent uniformity in the polar angle, it introduces an $\sim 10\%$ peak-to-valley, $\ell = 4$ variation in azimuth of the absorption because of the limited (four in each hemisphere) quads illuminating near a polar angle of 69° . This azimuthal variation can be reduced to 4% or lower with an $\ell = 8$ variation instead by splitting the 44.5° quads with two of the beams pointed to 46° and the remaining two to 69° . This splitting of the quads is not used in this work but is being investigated for future designs.

The on-target intensity from each of the rings is shown in Fig. 133.25. Rings 1 and 2 primarily irradiate the target near the pole, whereas the re-shifted Rings 3a, 3b, and 4 irradiate more toward the equator. The overlapped on-target intensity is higher near the equator. This is necessary to compensate for the reduced hydrodynamic efficiency from the more-oblique beams. Shock breakout is nearly uniform with this configuration of beam pointing, laser defocus, and pulse shapes except near the equator (Fig. 133.26). This significantly reduces core temperatures by injecting a jet of shell material into the hot spot

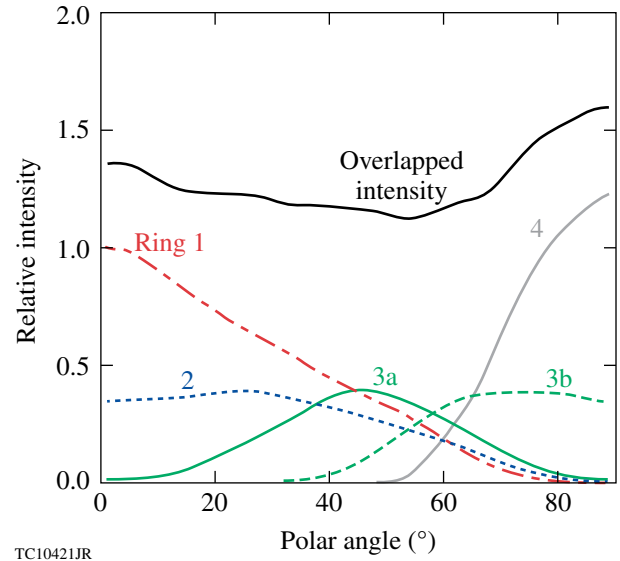


Figure 133.25

Intensity on target for the different rings at time $t = 0$. Rings 1 and 2 have peak irradiances near the pole. The shifting of Rings 3a, 3b, and 4 results in higher intensities toward the equator. The overlapped intensity is shown in black. Beams have been defocused and repointed (Table 133.V) to achieve this irradiation profile.

and radiatively cooling it. This can be corrected by designing an appropriate beam profile, as has been done for the ignition design, with the secondary ellipse on the equatorial beams.

For given pointing and defocus parameters, shell symmetry can be changed from spherical to prolate and oblate by changing the temporal pulse shapes, while maintaining the overall energy on target at $\sim 350 \text{ kJ}$ (see Fig. 133.27). The foot portion of the pulse, which determines the shock strength, is held constant among the three cases. Therefore, adjustments to the shape of the imploded shell can be made by varying the peak-power portions of the pulse shapes.

Table 133.V: The repointing and beam defocus used for the NIF design presented in the text. The pointing shift is as defined in Fig. 133.17: $\Delta r = R_t \times \sin(\theta_r - \theta)$, where R_t is the target radius.

Rings	Original port angle ($^\circ$) θ	Repointed angle ($^\circ$) θ_r	Pointing shift (Δr) (μm)	Number of quads (northern + southern)	Defocus distance (cm)
1	23.5	23.5	0	8	1.0
2	30.0	35.0	96	8	1.0
3a	44.5	46.0	29	8	1.5
3b	44.5	69.0	456	8	1.0
4	50.0	86.0	647	16	1.0

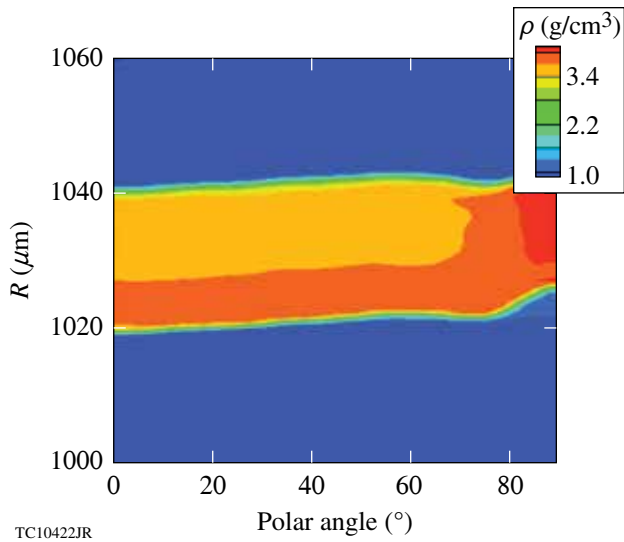


Figure 133.26
Mass-density contour at shock breakout (1.5 ns) versus radius and polar angle. The shock is largely uniform except near the equator.

Symmetry in the early stages of the implosion will be diagnosed using gated x-ray framing camera images of self-emission.³⁹ Photon energies $h\nu \geq 2$ keV from self-emission preferentially diagnose the imploding capsule outside the ablation surface.³⁹ For the three shell shapes, simulated images are shown in Fig. 133.27 at 7.2 ns—the latest time of observation corresponding to the end of the laser pulse. The *DRACO* simulations are post-processed with *Spect3D* including the pinhole diameter (100 μm), which is expected to be used in the initial experiments. Observable differences are predicted, as seen from Fig. 133.28, where the normalized amplitude of Legendre mode $\ell = 2$ is plotted versus time. The shaded regions include results from three simulations for each shape, where other long-wavelength nonuniformities⁴ such as beam mistiming (30-ps rms), beam mispointing (50- μm rms), and energy imbalance (8% rms) are included in the simulation. The deliberate asymmetries imposed in the PD designs dominate over the other nonuniformity seeds.

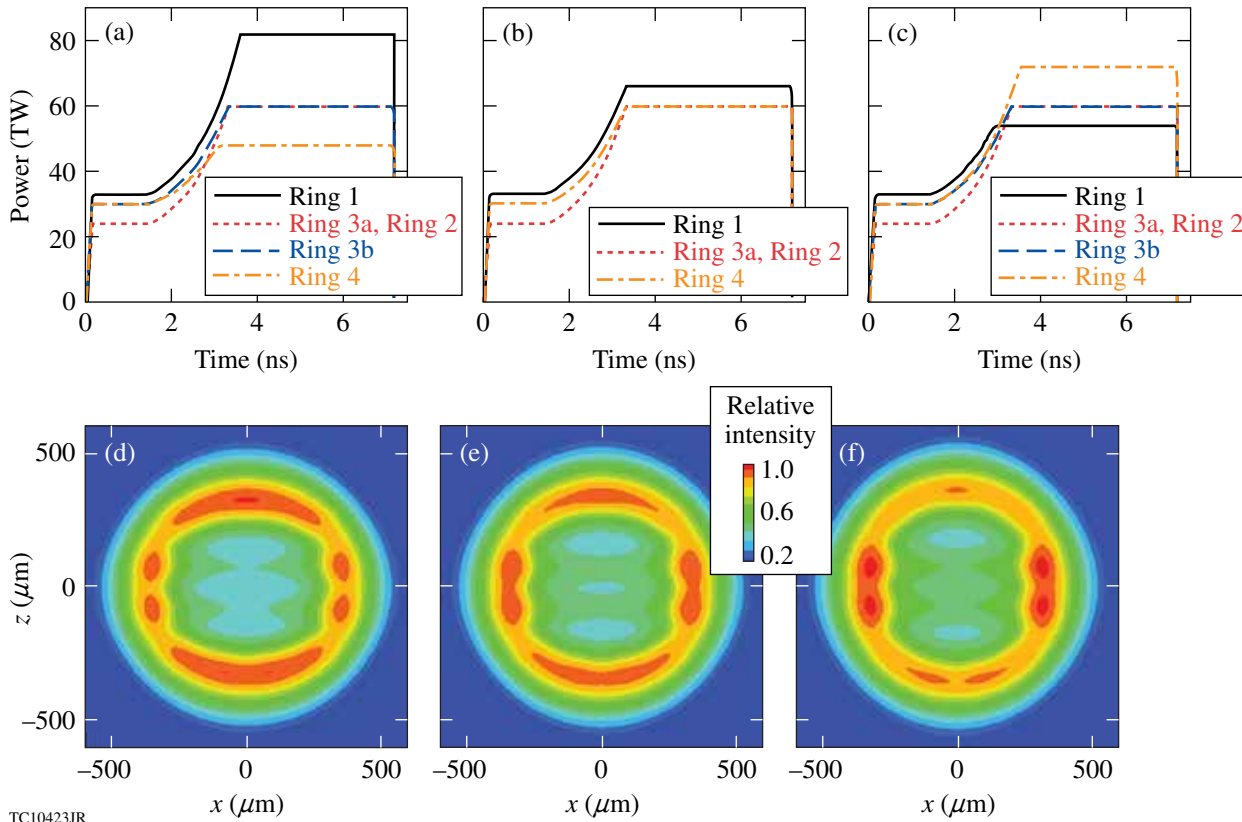


Figure 133.27
[(a)–(c)] Variations in pulse shapes used to achieve different shapes of the converging shell: (a) prolate, (b) spherical, and (c) oblate. The peak power of the pulse is varied with the shock strengths kept the same. [(d)–(f)] Corresponding x-ray gated framing-camera images from self-emission for $h\nu \geq 2$ keV.

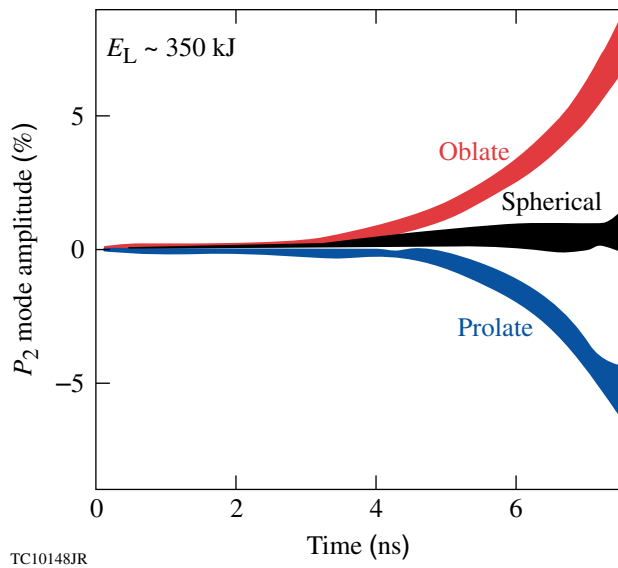


Figure 133.28

Relative amplitude (ratio of amplitude of Legendre mode $\ell = 2$ to shell position) versus time for the three shapes in Fig. 133.27. The shaded areas correspond to uncertainties associated with errors in beam timing, pointing, and energy balance.

Conclusions

The goal of OMEGA and NIF experiments is to validate physics models used to design PD ignition capsules and implement mitigating strategies for laser–plasma interactions. Laser-energy deposition and heat conduction are physics issues that need to be addressed at both OMEGA and NIF scales. In addition, it will be critical to understand issues related to preheat from energetic electrons produced by two-plasmon decay at the NIF scale. OMEGA PD experiments with emphasis on adiabat and symmetry were presented and observations compared with *DRACO* simulations. Two different pulse shapes were studied and it was found that areal density and symmetry are modeled well. Near-term PD experiments on OMEGA will be used to study PD target performance at ignition-relevant intensities. Initial NIF experiments are also discussed. The goal of these early experiments is to understand and address issues relating to the effect of two-plasmon decay on preheat and cross-beam energy transfer on implosion energetics and potentially symmetry.

ACKNOWLEDGMENT

This work was supported by the U.S. Department of Energy Office of Inertial Confinement Fusion under Cooperative Agreement No. DE-FC52-08NA28302, the University of Rochester, and the New York State Energy Research and Development Authority. The support of DOE does not constitute an endorsement by DOE of the views expressed in this article.

REFERENCES

1. S. Skupsky, J. A. Marozas, R. S. Craxton, R. Betti, T. J. B. Collins, J. A. Delettrez, V. N. Goncharov, P. W. McKenty, P. B. Radha, T. R. Boehly, J. P. Knauer, F. J. Marshall, D. R. Harding, J. D. Kilkenny, D. D. Meyerhofer, T. C. Sangster, and R. L. McCrory, *Phys. Plasmas* **11**, 2763 (2004).
2. E. Moses, presented at The Seventh International Conference on Inertial Fusion Sciences and Applications, Bourdeaux-Lac, France, 12–16 September 2011.
3. T. J. B. Collins, J. A. Marozas, K. S. Anderson, R. Betti, R. S. Craxton, J. A. Delettrez, V. N. Goncharov, D. R. Harding, F. J. Marshall, R. L. McCrory, D. D. Meyerhofer, P. W. McKenty, P. B. Radha, A. Shvydky, S. Skupsky, and J. D. Zuegel, *Phys. Plasmas* **19**, 056308 (2012).
4. T. J. B. Collins, J. A. Marozas, and P. W. McKenty, *Bull. Am. Phys. Soc.* **57**, 155 (2012).
5. M. C. Herrmann, M. Tabak, and J. D. Lindl, *Nucl. Fusion* **41**, 99 (2001).
6. Lord Rayleigh, *Proc. London Math Soc.* **XIV**, 170 (1883); G. Taylor, *Proc. R. Soc. London Ser. A* **201**, 192 (1950).
7. C. D. Zhou and R. Betti, *Phys. Plasmas* **14**, 072703 (2007).
8. P. B. Radha, C. Stoeckl, V. N. Goncharov, J. A. Delettrez, D. H. Edgell, J. A. Frenje, I. V. Igumenshchev, J. P. Knauer, J. A. Marozas, R. L. McCrory, D. D. Meyerhofer, R. D. Petrasso, S. P. Regan, T. C. Sangster, W. Seka, and S. Skupsky, *Phys. Plasmas* **18**, 012705 (2011).
9. T. C. Sangster, V. N. Goncharov, R. Betti, T. R. Boehly, R. Epstein, C. Forrest, V. Yu. Glebov, S. X. Hu, I. V. Igumenshchev, D. H. Froula, R. L. McCrory, D. D. Meyerhofer, P. B. Radha, W. Seka, W. T. Shmayda, S. Skupsky, C. Stoeckl, J. A. Frenje, D. T. Casey, and M. Gatu-Johnson, *Bull. Am. Phys. Soc.* **57**, 200 (2012).
10. *LLE Review Quarterly Report* **130**, 72, Laboratory for Laser Energetics, University of Rochester, Rochester, NY, LLE Document No. DOE/NA/28302-1058 (2012).
11. P. B. Radha, J. A. Marozas, F. J. Marshall, A. Shvydky, T. J. B. Collins, V. N. Goncharov, R. L. McCrory, P. W. McKenty, D. D. Meyerhofer, T. C. Sangster, and S. Skupsky, *Phys. Plasmas* **19**, 082704 (2012).
12. F. J. Marshall, P. W. McKenty, J. A. Delettrez, R. Epstein, J. P. Knauer, V. A. Smalyuk, J. A. Frenje, C. K. Li, R. D. Petrasso, F. H. Séguin, and R. C. Mancini, *Phys. Rev. Lett.* **102**, 185004 (2009).
13. P. B. Radha, F. J. Marshall, T. R. Boehly, T. J. B. Collins, R. S. Craxton, R. Epstein, V. N. Goncharov, J. A. Marozas, R. L. McCrory, P. W. McKenty, D. D. Meyerhofer, T. C. Sangster, A. Shvydky, S. Skupsky, J. A. Frenje, and R. D. Petrasso, “Polar Drive on OMEGA,” submitted to the *European Physical Journal*.
14. V. N. Goncharov, T. C. Sangster, T. R. Boehly, S. X. Hu, I. V. Igumenshchev, F. J. Marshall, R. L. McCrory, D. D. Meyerhofer, P. B. Radha, W. Seka, S. Skupsky, C. Stoeckl, D. T. Casey, J. A. Frenje, and R. D. Petrasso, *Phys. Rev. Lett.* **104**, 165001 (2010); P. B. Radha, J. A. Marozas, F. J. Marshall, A. Shvydky, T. J. B. Collins, V. N. Goncharov, R. L. McCrory, P. W. McKenty, D. D. Meyerhofer, T. C. Sangster, and S. Skupsky, *Phys. Plasmas* **19**, 082704 (2012).

15. S. Skupsky, R. W. Short, T. Kessler, R. S. Craxton, S. Letzring, and J. M. Soures, *J. Appl. Phys.* **66**, 3456 (1989).
16. T. R. Boehly, V. A. Smalyuk, D. D. Meyerhofer, J. P. Knauer, D. K. Bradley, R. S. Craxton, M. J. Guardalben, S. Skupsky, and T. J. Kessler, *J. Appl. Phys.* **85**, 3444 (1999).
17. F. H. Séguin, C. K. Li, J. A. Frenje, D. G. Hicks, K. M. Green, S. Kurebayashi, R. D. Petrasso, J. M. Soures, D. D. Meyerhofer, V. Yu. Glebov, P. B. Radha, C. Stoeckl, S. Roberts, C. Sorce, T. C. Sangster, M. D. Cable, K. Fletcher, and S. Padalino, *Phys. Plasmas* **9**, 2725 (2002).
18. P. B. Radha, V. N. Goncharov, T. J. B. Collins, J. A. Delettrez, Y. Elbaz, V. Yu. Glebov, R. L. Keck, D. E. Keller, J. P. Knauer, J. A. Marozas, F. J. Marshall, P. W. McKenty, D. D. Meyerhofer, S. P. Regan, T. C. Sangster, D. Shvarts, S. Skupsky, Y. Srebro, R. P. J. Town, and C. Stoeckl, *Phys. Plasmas* **12**, 032702 (2005).
19. J. A. Marozas, F. J. Marshall, R. S. Craxton, I. V. Igumenshchev, S. Skupsky, M. J. Bonino, T. J. B. Collins, R. Epstein, V. Yu. Glebov, D. Jacobs-Perkins, J. P. Knauer, R. L. McCrory, P. W. McKenty, D. D. Meyerhofer, S. G. Noyes, P. B. Radha, T. C. Sangster, W. Seka, and V. A. Smalyuk, *Phys. Plasmas* **13**, 056311 (2006).
20. R. C. Malone, R. L. McCrory, and R. L. Morse, *Phys. Rev. Lett.* **34**, 721 (1975).
21. J. Delettrez, *Can. J. Phys.* **64**, 932 (1986).
22. R. A. Lerche, D. W. Phillion, and G. L. Tietbohl, *Rev. Sci. Instrum.* **66**, 933 (1995).
23. P. B. Radha, J. A. Delettrez, R. Epstein, S. Skupsky, J. M. Soures, S. Cremer, and R. D. Petrasso, *Bull. Am. Phys. Soc.* **44**, 194 (1999).
24. R. Betti and C. Zhou, *Phys. Plasmas* **12**, 110702 (2005).
25. J. J. MacFarlane *et al.*, *High Energy Density Phys.* **3**, 181 (2007).
26. R. A. Forties and F. J. Marshall, *Rev. Sci. Instrum.* **76**, 073505 (2005).
27. J. D. Lindl, *Inertial Confinement Fusion: The Quest for Ignition and Energy Gain Using Indirect Drive* (Springer-Verlag, New York, 1998), p. 154.
28. I. V. Igumenshchev, D. H. Edgell, V. N. Goncharov, J. A. Delettrez, A. V. Maximov, J. F. Myatt, W. Seka, A. Shvydky, S. Skupsky, and C. Stoeckl, *Phys. Plasmas* **17**, 122708 (2010).
29. J. A. Marozas and T. J. B. Collins, *Bull. Am. Phys. Soc.* **57**, 344 (2012).
30. A. Simon, R. W. Short, E. A. Williams, and T. Dewandre, *Phys. Fluids* **26**, 3107 (1983).
31. C. Stoeckl, R. E. Bahr, B. Yaakobi, W. Seka, S. P. Regan, R. S. Craxton, J. A. Delettrez, R. W. Short, J. Myatt, A. V. Maximov, and H. Baldis, *Phys. Rev. Lett.* **90**, 235002 (2003).
32. P. B. Radha, J. P. Knauer, T. C. Sangster, V. N. Goncharov, I. V. Igumenshchev, R. Betti, R. Epstein, D. D. Meyerhofer, and S. Skupsky, *Bull. Am. Phys. Soc.* **52**, 143 (2007).
33. C. Stoeckl, P. B. Radha, R. E. Bahr, J. A. Delettrez, D. H. Edgell, V. Yu. Glebov, V. N. Goncharov, I. V. Igumenshchev, T. C. Sangster, W. Seka, J. A. Frenje, and R. D. Petrasso, *Bull. Am. Phys. Soc.* **56**, 241 (2011).
34. M. N. Rosenbluth, *Phys. Rev. Lett.* **29**, 565 (1972).
35. D. A. Russell and D. F. DuBois, *Phys. Rev. Lett.* **86**, 428 (2001).
36. L. Divol, LLNL, private communication (2012).
37. A. M. Cok, R. S. Craxton, and P. W. McKenty, *Phys. Plasmas* **15**, 082705 (2008).
38. J. A. Marozas, S. P. Regan, J. H. Kelly, D. D. Meyerhofer, W. Seka, and S. Skupsky, *J. Opt. Soc. Am. B* **19**, 7 (2002).
39. D. T. Michel, C. Sorce, R. Epstein, N. Whiting, I. V. Igumenshchev, R. Jungquist, and D. H. Froula, *Rev. Sci. Instrum.* **83**, 10E530 (2012).

Cross-Beam Energy Transfer in Polar-Drive Implosions on OMEGA

In the direct-drive approach to inertial confinement fusion, laser beams directly illuminate a spherical target, depositing their energy in the coronal plasma. This energy is transported to higher densities where ablation occurs and material rapidly expands, driving the nuclear fuel toward the center of the capsule. Symmetric illumination is required to produce a spherically symmetric drive. Ideally, the target is illuminated by a sufficient number of beams, distributed symmetrically around the target, to provide an adequately uniform drive with sufficient pressure to achieve ignition.¹

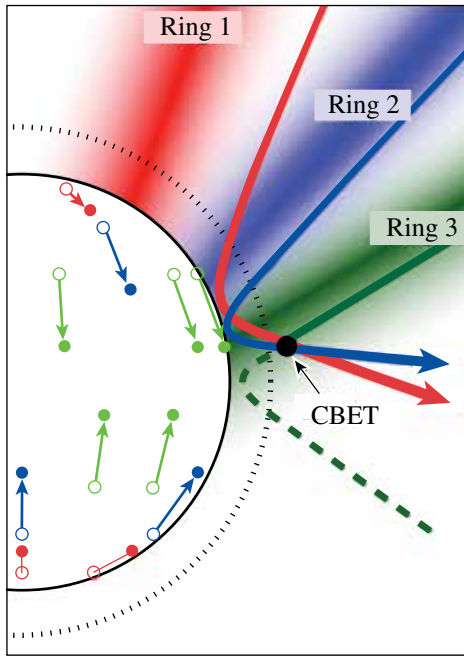
In the current x-ray drive configuration of the National Ignition Facility (NIF),² there are no laser beams near the equator of the target chamber and direct-drive experiments are performed in the polar-drive (PD) geometry.³ PD creates a uniform implosion by combining and repointing the NIF beams toward the target equator, employing phase plates designed to create specific on-target spot sizes, pulse shaping, and shimming of the target layers.⁴ The coupling of laser energy into the target can be decreased by cross-beam energy transfer (CBET)^{5–7} between the lasers.

CBET occurs when laser light seeds stimulated Brillouin scattering (SBS) in a plasma by crossing two or more laser beams. This low-gain SBS can drive ion-acoustic waves and transfer a significant amount of energy from one of the crossing beams to the other. Hydrodynamic one-dimensional (1-D) modeling of symmetric 60-beam direct-drive implosions on OMEGA that do not include CBET physics overpredict the laser drive by 10% to 20% as indicated by discrepancies with the observed bang times and time-dependent scattered-light spectra.^{8–10} Recently it was shown that decreasing the laser beams' radius with respect to the target radius reduces CBET and improves fusion yields.¹¹ The incorporation of CBET physics into the 1-D hydrodynamic modeling of symmetrically illuminated implosions produces good agreement with the observables, but the large scattering angles and three-dimensional (3-D) nature of the PD geometry has prevented previous CBET models from quantifying CBET in PD implosions.

CBET has been identified as a mechanism responsible for transferring significant amounts of energy between the NIF beams in indirect-drive hohlraum experiments.⁶ Independently varying the wavelength of the NIF beams to control CBET is used to tune the implosion symmetry.¹² CBET in indirect-drive experiments occurs at relatively low densities and the angle between crossing beams is small, so the models that post-process the hydrodynamic simulations to calculate CBET can use a paraxial approximation.^{6,7,13}

This article presents the first measurements of the effects of CBET in PD. The angular dependence of the unabsorbed light is measured to decrease from 1200 J/sr on the pole to 200 J/sr along the equator. These measurements and those of the unabsorbed light intensity and the spectra are reproduced by 3-D CBET modeling. These results indicate that CBET in PD reduces the absorbed energy by 10%. This reduction in absorption is consistent with the measurement of the bang time, which is ~180 ps later than predicted when CBET modeling is not included.¹⁴ Calculations indicate that the drive symmetry is reduced by energy transferred from the center of beams pointed near the equator to the outer edge of the beams pointed near the pole. This drive symmetry can be recovered by shifting the relative wavelength of the beams in each cone but the overall reduction in absorption is not ameliorated. The model predicts that CBET can be mitigated by using smaller beam spots.

The CBET calculations in this polar-drive geometry were carried out by post-processing two-dimensional (2-D) hydrodynamic simulations using a 3-D CBET model. The time-varying coronal plasma parameters were calculated by the code *DRACO*,¹⁵ where a Spitzer–Härm heat-transport model was used that limits the heat flow to a fraction ($f = 0.06$) of the free-streaming flux.¹⁶ The PD beam profiles in the CBET model are treated as the sum of many beamlets where the path and Doppler-shifted wavelength of each beamlet through the corona are determined by 3-D ray tracing (Fig. 133.29). This is a major difference between modeling CBET for polar drive and previous work modeling indirect-drive CBET, where the



E21825JR

Figure 133.29

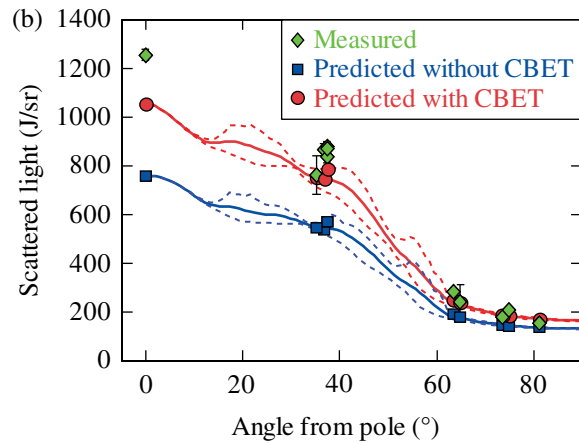
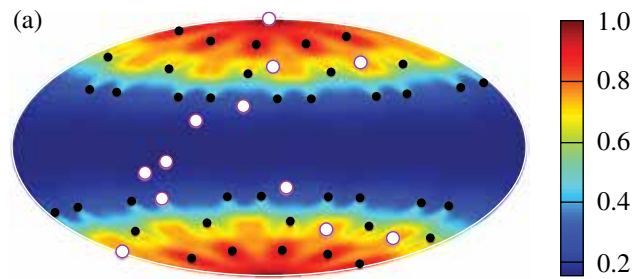
Pointing offsets for the beam rings for the polar-drive (PD) implosions on OMEGA used in this article: Ring 1 (red), Ring 2 (blue), and Ring 3 (green). Open circles show the pointing of each ring in symmetric drive (i.e., toward target chamber center); closed circles show the re-pointed PD geometry. The beamlets (rays) in the corona illustrate the effect of cross-beam energy transfer (CBET) on the laser illumination. The green Ring 3 beamlet directed toward the target equator is crossed by outgoing beamlets from Rings 1 and 2 before it reaches its nearest approach to the ablation surface, where it will be strongly absorbed. CBET scatters energy from this equatorial beamlet to the outgoing beamlets, reducing the energy deposition at the equator near the ablation surface.

refraction of the laser beams is ignored.¹³ The CBET at crossings between beamlets for all PD beams is calculated from the SBS spatial gain length in the strong damping limit.^{9,17}

The PD implosions used 40 ultraviolet ($\lambda_0 = 351$ nm) OMEGA laser beams.¹⁸ In the PD geometry, the beams are grouped into three rings with offset pointing toward the target equator as shown in Fig. 133.29. The laser beams were smoothed by polarization smoothing,¹⁸ distributed phase plates,¹⁹ and smoothing by spectral dispersion.²⁰ All beams used the same pulse shape and distributed phase plates with circular super-Gaussian ($n = 4$) beam profiles, where 95% of the power is within a diameter of $865 \mu\text{m}$. The beams were incident on spherical CH capsules with $27\text{-}\mu\text{m}$ -thick walls and a total diameter of $866 \mu\text{m}$. The targets were filled with 11.4 atm of D_2 .

The angular dependence of the unabsorbed light was measured using 12 calorimeters located around the target chamber [Fig. 133.30(a)]. Four of these locations couple the unabsorbed light to a 1.25-m spectrometer with a Rochester Optical Streak System via optical fibers. This system has a spectral resolution of 0.05 nm and a temporal resolution of 90 ps.

Figure 133.30(b) shows the time-integrated angular distribution of the light that is scattered (i.e., not absorbed) by the coronal plasma. A factor-of-6 more light is measured on the pole than the equator. This is in good agreement with calculations of the unabsorbed light when using the CBET model, and Fig. 133.30(b) shows that the unabsorbed light at all angles is significantly underestimated when the CBET model is not used.

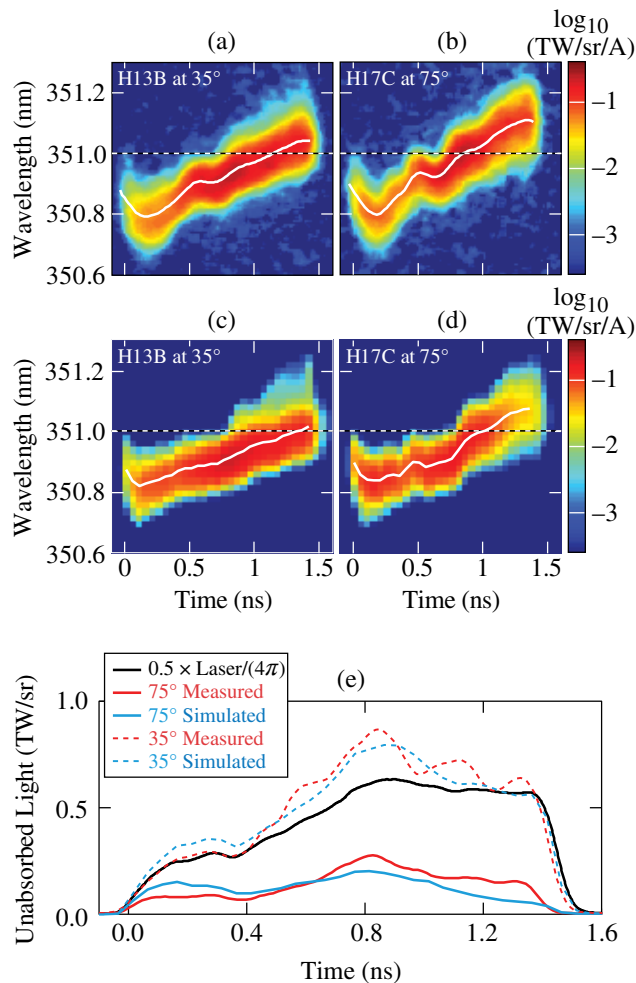


E21281JR

Figure 133.30

(a) Aitoff projection of the calculated distribution of the normalized time-integrated scattered light over the inner surface of the OMEGA target chamber. White circles show the locations of the scattered-light calorimeters in the OMEGA chamber. Black dots represent the beam ports. (b) Time-integrated, unabsorbed-light radiant intensity as a function of angle from the PD symmetry axis as predicted without CBET modeling (blue squares), predicted with CBET modeling (red circles), and measured (green diamonds). The error bars on the measurements are the standard deviation of multiple measurements from nominally identical PD implosions. The solid lines show the model calculations of the mean value of the radiant intensity, while the dashed lines show the calculated minimum/maximum range around the target azimuthally.

Figure 133.31 shows that, in addition to the total integrated scattered power, the CBET model accurately predicts the time-varying spectrally resolved details of unabsorbed light from the PD implosions. The measured spectra from two polar angles [Figs. 133.31(a) and 133.31(b)] show the variation in wavelength and power of the unabsorbed light. This variation is the result of the time-varying optical path length of the light traveling through the coronal plasma. The initial blue shift in the spectra occurs as the light propagates through a rapidly increasing electron density when the plasma is formed.²¹ The blue shift



E21538JR

Figure 133.31

Unabsorbed laser light spectra measured at (a) 35° and (b) 75° from the PD pole along with the respective simulated spectra [(c) and (d)]. (e) The time-varying radiant intensity of the measured (red curves) and simulated (blue curves) unabsorbed laser light. Shown for reference is the radiant intensity that would result if the total incident laser power (black curve) were spread evenly over 4π steradian (divided by 2 for convenient scaling).

results partially from the outward movement of the plasma's critical-density surface (a moving-mirror Doppler shift) and partially from the outward buildup of the coronal plasma that reduces the optical path length of the laser light because plasma has a smaller index of refraction than vacuum. As the plasma scale length reaches a steady state, the plasma's critical-density surface implodes, red shifting the unabsorbed light.

Figures 133.31(c) and 133.31(d) show the time-varying spectral intensity calculated by the CBET model. The important features present in the measured spectra are reproduced, indicating the accuracy of the hydrodynamic modeling used to calculate coronal plasma conditions. The discrepancy in the magnitude of the initial blue shift in the spectra is similar to that observed for symmetric drive implosions when a flux-limited heat-transport model was used. A nonlocal electron-transport model was required to accurately model the initial blue-shifted unabsorbed light for symmetric implosions.⁹ The flux-limited model predicts shorter density scale-lengths than the nonlocal model, resulting in a slower initial outward movement of the plasma's critical-density surface and less coronal plasma density along the laser light's optical paths. Both effects decrease the predicted initial blue shift of the unabsorbed light spectrum.

The time-varying radiant intensity (TW/sr) of the unabsorbed light shown in Fig. 133.31(e) is obtained by integrating the spectra over wavelength. The calculations are in good agreement with the measurements. The accuracy of the scattered-light predictions given by the CBET model allows one to draw conclusions about the effect of CBET on the drive energetics during a PD implosion and to suggest possible CBET mitigation strategies.

Calculations indicate that CBET reduces the absorption from 85% to 76% and that this reduction is disproportionately distributed among the rings. The closer the ring is pointed to the equator, the more it is affected by CBET. The absorption in Ring 1 (the most-polar ring) drops to 82%, while Ring 3 (the most-equatorial ring) has its absorption reduced to 72% by CBET. This is consistent with the measured bang time being ~180 ps later than predicted when CBET is not included in the hydrodynamics code.¹⁴

The location where CBET occurs in PD is illustrated in Fig. 133.32. For all three beam rings, CBET results in a net loss of energy from the center portion of the beam profiles. This central portion includes the beamlets with the smallest impact parameters that penetrate farthest into the coronal plasma. In

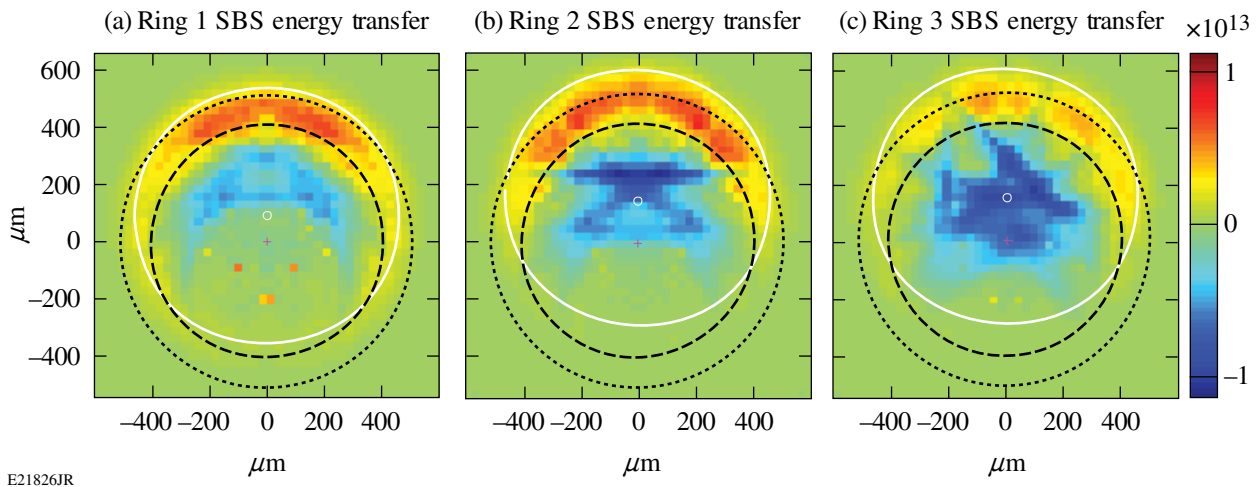


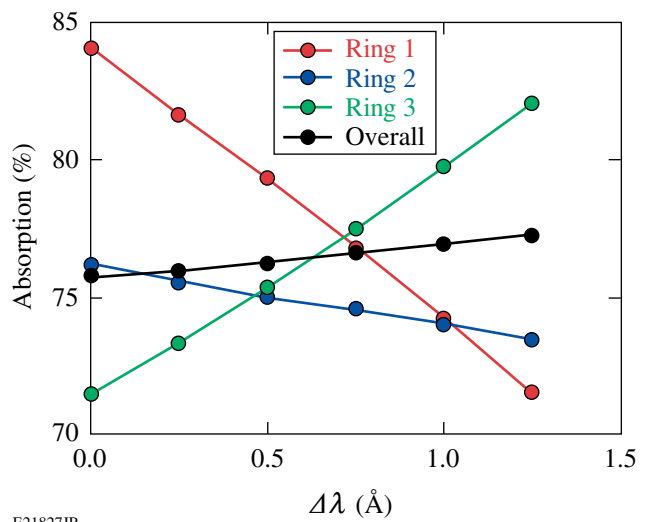
Figure 133.32

The normalized energy transferred for each OMEGA PD beam ring: (a) Ring 1, (b) Ring 2, and (c) Ring 3. The position of each pixel is the launch point of a beamlet, the sum of which represents the beam profile of one of the beams in an OMEGA PD beam ring. The magnitude of each pixel is the relative net energy transferred into (positive/red) or out of (negative/blue) a beamlet integrated along the path of each beamlet. The black curves show the position of the target’s critical surface (dashed) and quarter-critical surfaces (dotted) with respect to the launched position of the beamlets. The white curve is the 95% power contour of the laser-beam spot.

the absence of CBET, these beamlets deposit their energy closest to the ablation surface and would most efficiently drive the target. In contrast, beamlets with impact parameters outside the plasma’s critical-density radius gain a net amount of energy from CBET but are less efficiently absorbed. In effect, energy is transferred from the drive-efficient, small-impact-parameter beamlets to the less-efficient, higher-impact-parameter beamlets, resulting in reduced hydrodynamic efficiency.

The distribution of CBET over the beam profiles suggests a possible strategy to reducing its detrimental effect on driving the target: eliminating the high-impact-parameter beamlets that “steal” energy from the drive-efficient beamlets. The CBET model predicts that for the coronal plasma conditions in the OMEGA PD implosions, the overall absorption loss to CBET can be recovered using 30%-smaller beam radii. This improvement comes from a combination of reducing CBET and concentrating the beam energy into the more-efficient, low-impact-parameter beamlets. The effect of smaller spot sizes on implosion symmetry should be studied because PD implosions require some high-impact-parameter beamlets to direct energy toward the equator for symmetry.

Figure 133.33 illustrates the effect that varying the wavelength of the laser beams has on the energy absorbed from each ring. The predicted CBET among the rings is altered when laser



E21827JR

Figure 133.33

The absorption in each PD ring varies significantly when there is a difference in wavelength between the rings. Here $\Delta\lambda$ is the separation in wavelength between the rings. For example if $\Delta\lambda = 1 \text{ \AA}$, the wavelength of Ring 3 is 1 \AA greater than Ring 2, which has a wavelength 1 \AA greater than Ring 1.

beams of different rings have different wavelengths. The flow of energy is biased toward the beams in the rings with the longer wavelengths. When the wavelengths of the beams in all rings are equal ($\Delta\lambda = 0$), CBET between the beams in Rings 1 and 3

results in a net gain for the beams in Ring 1 and a net loss for Ring 3 beams. As the wavelength separation between the beams in different rings increases (with Ring 3's wavelength growing larger than Ring 1's), the net transfer between Rings 1 and 3 is reduced and eventually reverses until the beams in Ring 3 experience a net gain in energy from CBET with beams in Ring 1. At wavelength shifts greater than $\sim 0.75 \text{ \AA}$, the absorbed energy from beams in Ring 3 is greater than that from beams in Ring 1. The change in absorption for beams in Ring 2 is less pronounced. As $\Delta\lambda$ increases, the beams in Ring 2 take more energy from beams in Ring 1, which is offset by losing energy to beams in Ring 3. The overall energy absorption is nearly constant as $\Delta\lambda$ increases because gains by one ring are offset by losses in another. These results suggest that the power balance of the rings in a PD implosion can be controlled by independently setting the wavelengths of the rings with wavelength separations of the order of 1 \AA (Ref. 7). This makes it possible to control the symmetry of a PD implosion.

In summary, measurements of the angular dependence of the unabsorbed light during polar-drive implosions at the Omega Laser Facility have been recorded. The radiant intensity of the unabsorbed light decreases from 1200 J/sr on the pole to 200 J/sr along the equator. The measured unabsorbed light intensity and spectrum are in good agreement with predictions from a 3-D CBET model. The modeling shows that CBET reduces the overall laser absorption in PD by $\sim 10\%$. The ring of beams directed toward the PD equator is compromised most severely. The modeling provides insight into two possible CBET mitigation strategies. The location where the energy transfer occurs suggests that reducing the spot size will reduce the CBET losses. This is supported by modeling with small spot sizes where the laser absorption increased by $\sim 10\%$. The modeling shows that the flow of energy between the PD beam rings can be manipulated by varying the wavelength separation between the rings. This could be used to regulate the power balance between the rings and exert control over the implosion symmetry. These results will help guide upcoming polar-drive experiments on the NIF, where 1.5 MJ of laser energy will be used to implode ~ 2 -mm-diam capsules with the ultimate goal of producing fusion.⁴

ACKNOWLEDGMENT

We acknowledge the OMEGA operations team whose efforts enabled us to perform these polar-drive experiments. This work was supported by the U.S. Department of Energy Office of Inertial Confinement Fusion under Cooperative Agreement No. DE-FC52-08NA28302, the University of Rochester, and the New York State Energy Research and Development Authority. The support of DOE does not constitute an endorsement by DOE of the views expressed in this article.

REFERENCES

1. J. Nuckolls, L. Wood, A. Thiessen, and G. Zimmerman, *Nature* **239**, 139 (1972); V. N. Goncharov, T. C. Sangster, T. R. Boehly, S. X. Hu, I. V. Igumenshchev, F. J. Marshall, R. L. McCrory, D. D. Meyerhofer, P. B. Radha, W. Seka, S. Skupsky, C. Stoeckl, D. T. Casey, J. A. Frenje, and R. D. Petrasso, *Phys. Rev. Lett.* **104**, 165001 (2010).
2. E. I. Moses, *Fusion Sci. Technol.* **44**, 11 (2003).
3. S. Skupsky, J. A. Marozas, R. S. Craxton, R. Betti, T. J. B. Collins, J. A. Delettrez, V. N. Goncharov, P. W. McKenty, P. B. Radha, T. R. Boehly, J. P. Knauer, F. J. Marshall, D. R. Harding, J. D. Kilkenny, D. D. Meyerhofer, T. C. Sangster, and R. L. McCrory, *Phys. Plasmas* **11**, 2763 (2004).
4. T. J. B. Collins, J. A. Marozas, K. S. Anderson, R. Betti, R. S. Craxton, J. A. Delettrez, V. N. Goncharov, D. R. Harding, F. J. Marshall, R. L. McCrory, D. D. Meyerhofer, P. W. McKenty, P. B. Radha, A. Shvydky, S. Skupsky, and J. D. Zuegel, *Phys. Plasmas* **19**, 056308 (2012).
5. C. J. Randall, J. R. Albritton, and J. J. Thomson, *Phys. Fluids* **24**, 1474 (1981).
6. P. Michel *et al.*, *Phys. Rev. Lett.* **102**, 025004 (2009).
7. P. Michel *et al.*, *Phys. Rev. E* **83**, 046409 (2011).
8. W. Seka, D. H. Edgell, J. P. Knauer, J. F. Myatt, A. V. Maximov, R. W. Short, T. C. Sangster, C. Stoeckl, R. E. Bahr, R. S. Craxton, J. A. Delettrez, V. N. Goncharov, I. V. Igumenshchev, and D. Shvarts, *Phys. Plasmas* **15**, 056312 (2008).
9. I. V. Igumenshchev, D. H. Edgell, V. N. Goncharov, J. A. Delettrez, A. V. Maximov, J. F. Myatt, W. Seka, A. Shvydky, S. Skupsky, and C. Stoeckl, *Phys. Plasmas* **17**, 122708 (2010).
10. I. V. Igumenshchev, W. Seka, D. H. Edgell, D. T. Michel, D. H. Froula, V. N. Goncharov, R. S. Craxton, L. Divol, R. Epstein, R. Follett, J. H. Kelly, T. Z. Kosc, A. V. Maximov, R. L. McCrory, D. D. Meyerhofer, P. Michel, J. F. Myatt, T. C. Sangster, A. Shvydky, S. Skupsky, and C. Stoeckl, *Phys. Plasmas* **19**, 056314 (2012).
11. D. H. Froula, I. V. Igumenshchev, D. T. Michel, D. H. Edgell, R. Follett, V. Yu. Glebov, V. N. Goncharov, J. Kwiatkowski, F. J. Marshall, P. B. Radha, W. Seka, C. Sorce, S. Stagnitto, C. Stoeckl, and T. C. Sangster, *Phys. Rev. Lett.* **108**, 125003 (2012).
12. S. H. Glenzer *et al.*, *Science* **327**, 1228 (2010).
13. P. Michel *et al.*, *Phys. Plasmas* **17**, 056305 (2010).
14. P. B. Radha, J. A. Marozas, F. J. Marshall, A. Shvydky, T. J. B. Collins, V. N. Goncharov, R. L. McCrory, P. W. McKenty, D. D. Meyerhofer, T. C. Sangster, and S. Skupsky, *Phys. Plasmas* **19**, 082704 (2012).
15. P. B. Radha, V. N. Goncharov, T. J. B. Collins, J. A. Delettrez, Y. Elbaz, V. Yu. Glebov, R. L. Keck, D. E. Keller, J. P. Knauer, J. A. Marozas, F. J. Marshall, P. W. McKenty, D. D. Meyerhofer, S. P. Regan, T. C. Sangster, D. Shvarts, S. Skupsky, Y. Srebro, R. P. J. Town, and C. Stoeckl, *Phys. Plasmas* **12**, 032702 (2005).

16. R. C. Malone, R. L. McCrory, and R. L. Morse, *Phys. Rev. Lett.* **34**, 721 (1975).
17. J. Myatt, A. V. Maximov, W. Seka, R. S. Craxton, and R. W. Short, *Phys. Plasmas* **11**, 3394 (2004).
18. T. R. Boehly, V. A. Smalyuk, D. D. Meyerhofer, J. P. Knauer, D. K. Bradley, R. S. Craxton, M. J. Guardalben, S. Skupsky, and T. J. Kessler, *J. Appl. Phys.* **85**, 3444 (1999).
19. Y. Lin, T. J. Kessler, and G. N. Lawrence, *Opt. Lett.* **20**, 764 (1995).
20. S. Skupsky, R. W. Short, T. Kessler, R. S. Craxton, S. Letzring, and J. M. Squires, *J. Appl. Phys.* **66**, 3456 (1989).

Measured Hot-Electron Intensity Thresholds Quantified by a Two-Plasmon–Decay Resonant Common-Wave Gain in Various Experimental Configurations

Introduction

In inertial confinement fusion (ICF), a spherical capsule is imploded using multiple laser beams to produce an energetic fusion reaction by compressing nuclear fuel to high densities and temperatures.¹ In the direct-drive scheme,² the capsule is uniformly illuminated by overlapping beams, and in the indirect-drive scheme,³ the laser beams are first converted into x rays that then illuminate the capsule. In both schemes, the laser beams can drive the two-plasmon–decay (TPD) instability.^{4–8} When TPD is driven strongly, an extended spectrum of large-amplitude electron plasma waves (EPW's) is generated that accelerates electrons to high energies (~ 100 keV) (Refs. 9–12). These electrons can deposit their energy in the fuel (preheat), reducing the compression efficiency and potentially inhibiting ICF ignition. Although no experiments have definitively measured the effects of preheat, hydrodynamic simulations that include an *ad hoc* hot-electron model indicate low-adiabat ignition designs can survive $\sim 0.1\%$ of laser energy converted into hot electrons and coupled to the fusion fuel.¹³

The TPD instability results from the decay of an electromagnetic wave into two electron plasma waves.^{4,5} Phase matching, energy conservation, and the dispersion relations of the waves limit the instability to a small region near the quarter-critical density surface. Stability calculations of a single linearly polarized electromagnetic wave show that the absolute threshold of the instability is proportional to $I_s L_n / T_e$, where I_s is the laser-beam intensity, L_n is the plasma density scale length, and T_e is the electron temperature of the plasma at the quarter-critical density.⁶ More-recent particle-in-cell (PIC) simulations have shown the importance of convective mode in the nonlinear stage that also depends on $I_s L_n / T_e$ (Ref. 14). Multibeam experiments have shown that hot-electron production scales with the overlapped vacuum laser-beam intensity (I_{OVP}) (Ref. 15) independent of the number of beams used. This scaling is not expected if the laser beams drive TPD independently. To explain these results, a multibeam model was proposed where different laser beams share a common electron plasma wave.^{16,17} Recent experiments at the Omega Laser Facility^{18,19} showed that the overlapped intensity threshold for hot-electron

generation depends on the laser-beam and target geometries.²⁰ A model that calculates the homogeneous, multibeam, TPD growth rate shows that beams that share the same angle with respect to the common-wave vector can couple through the resonant common electron plasma wave and that this coupling occurs in the region in k space bisecting the laser beams.²¹ In this common-wave region, the TPD growth rate depends on the geometry and the polarization of the laser beams.

This article reports on the measured hot-electron fraction generated by TPD in planar experiments using one to four linearly polarized beams, 18 beams with polarization smoothing, and, in spherical experiments, 60 beams with polarization smoothing. The overlapped intensity threshold for hot-electron generation is different for each experimental configuration. These measured thresholds are compared with convective gains calculated with the resonant common-wave model.

The following sections describe (1) the various experimental configurations; (2) the experimental results, where the overlapped intensity threshold for hot-electron generation is observed to be different for the various experimental configurations; and (3) the multibeam TPD resonant common-wave growth rate for linearly polarized beams and beams with polarization smoothing. Next, the common-wave gain is shown to be consistent with observed variations in the TPD thresholds, followed by the conclusions.

Experimental Setup

The experiments discussed here were designed to measure the intensity thresholds for the production of hot electrons while varying different parameters in the common-wave gain. On OMEGA EP,¹⁹ the hot-electron fraction was measured in planar geometry as a function of the laser energy for one-, two-, and four-beam configurations to study the variation of the hot-electron production with a maximum normalized growth rate that depends on the polarization and geometry of the laser beams. The four-beam results were compared to OMEGA planar experiments, where 18 beams distributed in three cones were used to study the variation in the hot-electron production

with the number of beams that contribute to the common-wave TPD. The planar experiments are compared to OMEGA experiments in spherical geometry to measure the variation in the hot-electron production with the plasma parameters.

1. Laser Setup

a. OMEGA EP planar geometry. In the OMEGA EP experiments, four vertically polarized 351-nm beams intersected the target at an angle of 23° with respect to the target normal [Fig. 133.34(a)]. The focal spots of the beams were spatially overlapped to within $20\ \mu\text{m}$. The beams used 2-ns flattop laser pulses that were co-timed to within 50 ps. Two sets of distributed phase plates (DPP's)²² were used [860- μm full width at half maximum (FWHM) for Beams 1 and 2 and 800- μm FWHM for Beams 3 and 4] to produce an ~ 1 -mm-diam, ninth-order super-Gaussian intensity profile. A maximum single-beam energy of 2.0 kJ (2.6 kJ) was used on Beams 1 and 2 (3 and 4), resulting in peak single-beam intensities $I_{\text{max}} = 1.8 \times 10^{14}\ \text{W/cm}^2$ ($I_{\text{max}} = 2.6 \times 10^{14}\ \text{W/cm}^2$). Experiments were performed using one beam; two beams in a horizontal configuration (Beams 1 and 4), vertical configuration (Beams 1 and 3), and diagonal configuration (Beams 1 and 2); and four beams [Fig. 133.34(a)].

b. OMEGA planar geometry. In the OMEGA planar experiments, 18 beams at a wavelength of 351 nm intersected the

target in three cones of six beams at angles of 23° , 48° , and 63° with respect to the target normal [Fig. 133.34(b)]. The beams were spatially overlapped to within $20\ \mu\text{m}$. The beams used 2-ns flattop laser pulses that were co-timed to within 10 ps. All beams were smoothed by polarization smoothing (PS)²³ and DPP's (710- μm FWHM) to produce an ~ 1 -mm-diam, fourth-order super-Gaussian intensity profile. The single-beam energy ranged from 240 J to 380 J, providing a peak single-beam intensity ranging from $3.4 \times 10^{13}\ \text{W/cm}^2$ to $5.4 \times 10^{13}\ \text{W/cm}^2$.

c. OMEGA spherical geometry. In the OMEGA spherical experiments, 60 laser beams at 351 nm smoothed by PS and DPP's (710- μm FWHM) uniformly illuminated an 860- μm -diam spherical target [Fig. 133.34(c)]. The beams were pointed with an accuracy of $20\ \mu\text{m}$. The beams used 1-ns flattop laser pulses that were co-timed to within 10 ps. The 60 laser beams used a total energy of 13 kJ to 29.5 kJ to produce a spherically symmetric illumination of the target. The peak single-beam intensity was varied from $5 \times 10^{13}\ \text{W/cm}^2$ to $1.2 \times 10^{14}\ \text{W/cm}^2$.

2. Targets

a. Planar geometry. For the planar experiments on both OMEGA and OMEGA EP, the laser beams illuminated a 30- μm -thick CH layer deposited on 30 μm of Mo and backed with an additional 30 μm of CH. Hydrodynamic simulations using the two-dimensional (2-D) code *DRACO*²⁴ indicated that

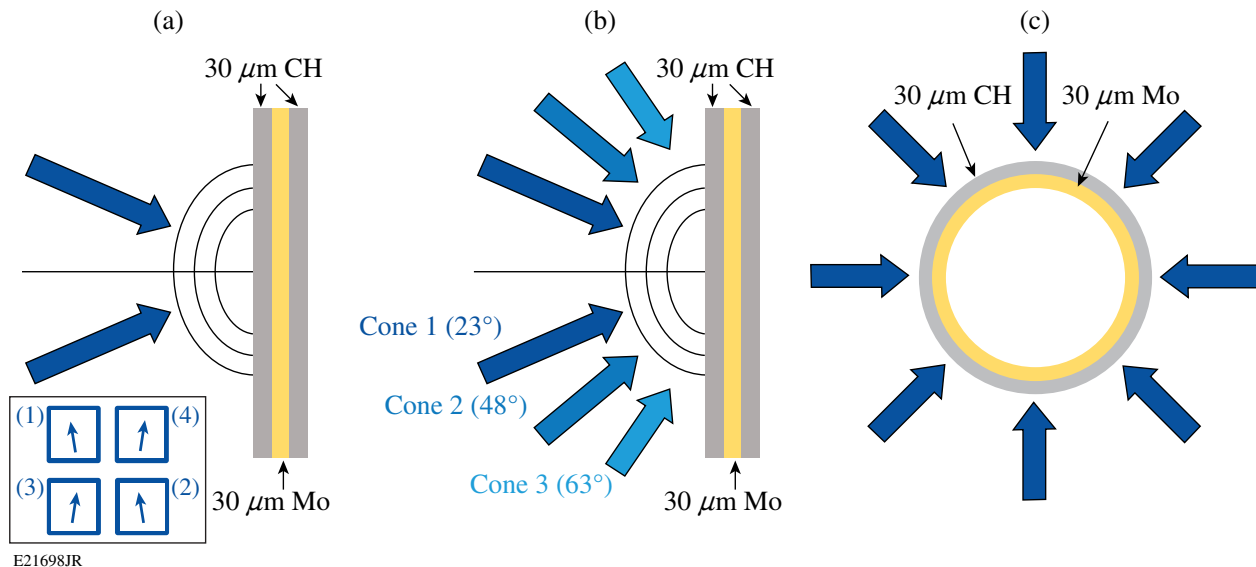


Figure 133.34

Schematic of the laser-beam configurations on (a) OMEGA EP, (b) OMEGA (planar geometry), and (c) OMEGA (spherical geometry). In OMEGA EP experiments, the polarizations of the beams are 8° from vertical [inset in (a)], and in OMEGA experiments, the beams used polarization smoothing.

the laser light interacted with the first layer, producing a CH plasma with density and temperature profiles that depended (for each configuration) only on the overlapped laser intensity. For the experimental conditions presented here, the hydrodynamic profiles near quarter-critical density reached steady state after about 1.5 ns. After this time, the calculated quantity $I_{\text{ovr,q}}L_{\text{n,q}}/T_{\text{e,q}}$ varied by less than 10% at the quarter-critical density (the subscript “q” refers to quantities at the quarter-critical density surface).

For the OMEGA EP experiments, the overlapped laser intensity was increased from $1.5 \times 10^{14} \text{ W/cm}^2$ to $7 \times 10^{14} \text{ W/cm}^2$, the density scale length ($L_{\text{n,q}}$) increased from 260 μm to 360 μm , and the electron temperature ($T_{\text{e,q}}$) increased from 1.5 keV to 2.5 keV; the ratio $L_{\text{n,q}}/T_{\text{e,q}}$ was nearly constant over this intensity range ($\approx 160 \mu\text{m/keV}$). The laser intensity at quarter-critical density was about half the vacuum intensity.

For the OMEGA planar experiments, the overlapped laser intensity was increased from $4 \times 10^{14} \text{ W/cm}^2$ to $6.5 \times 10^{14} \text{ W/cm}^2$, the density scale length ($L_{\text{n,q}}$) increased from 260 μm to 320 μm , and the electron temperature ($T_{\text{e,q}}$) increased from 2 keV to 2.4 keV; the ratio $L_{\text{n,q}}/T_{\text{e,q}}$ was nearly constant over this intensity range ($\approx 135 \mu\text{m/keV}$). The overlapped laser intensity at quarter-critical density was about half the vacuum overlapped intensity.

b. Spherical geometry. In the spherical experiments, the laser beams illuminated an 800- μm -diam, 30- μm -thick Mo shell coated with 30 μm of CH. Hydrodynamic simulations using the one-dimensional (1-D) code *LILAC*²⁵ showed that the laser light interacted only with the CH layer and the hydrodynamic profiles near quarter-critical density reached a steady state after about 0.5 ns. After this time, the calculated quantity $I_{\text{ovr,q}}L_{\text{n,q}}/T_{\text{e,q}}$ varied by less than 10%, where $I_{\text{ovr,q}} \equiv P_{\text{L,q}}/4\pi R_{\text{q}}^2$, $P_{\text{L,q}}$ is the laser power at the quarter-critical-density surface, and R_{q} is the radius of the quarter-critical-density surface. When the overlapped laser intensity was increased from $5 \times 10^{14} \text{ W/cm}^2$ to $12 \times 10^{14} \text{ W/cm}^2$, the density scale length ($L_{\text{n,q}}$) increased from 120 μm to 140 μm and the electron temperature ($T_{\text{e,q}}$) increased from 2.1 keV to 2.2 keV; the ratio $L_{\text{n,q}}/T_{\text{e,q}}$ was nearly constant over this intensity range ($\approx 60 \mu\text{m/keV}$). The overlapped laser intensity at quarter-critical density (570 μm) was about half the overlapped vacuum intensity.

3. Diagnostics

Two principal diagnostics were used to determine the amount of laser energy converted to hot electrons: an x-ray spectrometer

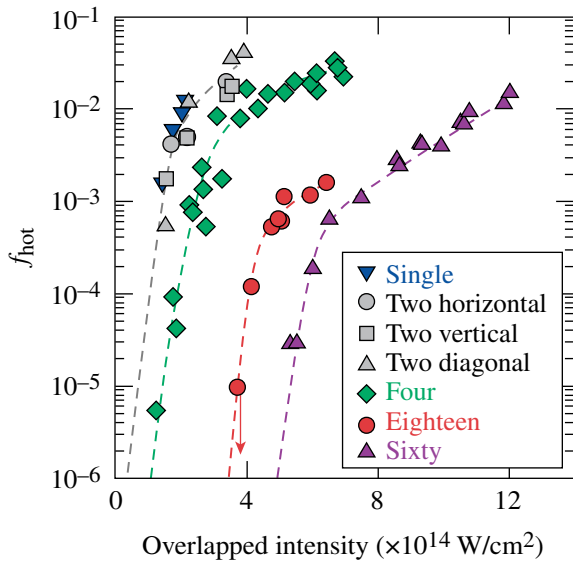
(XRS)^{26–28} and a hard x-ray detector (HXRD).²⁹ Monte Carlo simulations using the code *EGSnrc*³⁰ were used to determine the total hot-electron energy (E_{e}) given the measured hard x-ray temperature and the total energy in the K_{α} emission.²⁶

a. X-ray spectrometer. The XRS measures the energy emitted into the Mo K_{α} emission line ($E_{\text{K}_{\alpha}}$) using an absolutely calibrated planar LiF crystal spectrometer that views the target from the laser’s incident side at an angle of 63° from the target normal²⁶ on OMEGA EP, 37.4° from the target normal on OMEGA planar experiments, and along the target normal for spherical experiments. The Monte Carlo simulations show that electrons with energies less than 120 keV are stopped in the Mo. The 17.5-keV Mo K_{α} line is sufficiently energetic so that photoexcitation from the 2.5-keV coronal plasma region does not contribute to the K_{α} -emission measurement.

b. Hard x-ray detector. The hard x-ray detector consists of a three-channel filtered scintillator array that measures the x-ray radiation generated by the hot electrons in the Mo above ~ 40 keV, ~ 60 keV, and ~ 80 keV (Ref. 29). The hard x-ray detector views the back of the target at an angle of 40° from the target normal on OMEGA EP and 42° from the target normal on OMEGA planar experiments. The hard x-ray temperature is estimated using the exponentially decreasing x-ray energies measured by the three channels. The relative error in the measurement of the slope (T_{rad}) in the hard x-ray spectrum is 20%. Monte Carlo simulations indicate that the hard x-ray temperature is a good measure of the hot-electron temperature T_{hot} ($T_{\text{rad}} \simeq T_{\text{hot}}$) (Ref. 26).

Experimental Results

Figure 133.35 shows that for all configurations tested, the hot-electron fraction defined as the fraction of laser energy converted to hot electrons (f_{hot}) increases exponentially with the overlapped vacuum laser-beam intensities and, at high intensities, the increase is much slower. The rapid increase in hot-electron production at low intensities is used to determine an intensity threshold defined as the overlapped intensity when the hot-electron fraction is equal to 10^{-4} (near the detector threshold). For one and two linearly polarized beams in the horizontal, vertical, and diagonal configuration (OMEGA EP planar geometry), a similar evolution with the overlapped-laser-beam intensity is measured and a hot-electron–production threshold of $I_{\text{th}} \sim 10^{14} \text{ W/cm}^2$ is inferred. For the four-beam configuration (OMEGA EP planar geometry), the threshold dependence on the overlapped intensity is increased by a factor of 2 and a threshold of $I_{\text{th}} \sim 2 \times 10^{14} \text{ W/cm}^2$ is measured. A factor-of-2 further increase in the



E21699JR

Figure 133.35

Hot-electron fraction (f_{hot}) as a function of vacuum overlapped laser intensity. Single, two, and four correspond to OMEGA EP planar experiments where the beams are linearly polarized; 18 (60) corresponds to OMEGA planar (spherical) experiments where the beams have polarization smoothing. The dashed lines are drawn to guide the eye. In each case, the overlapped intensity at quarter-critical density is about half the vacuum overlapped intensity. For the 18-beam configuration, at an overlapped intensity of 4×10^{14} W/cm², the signal was lower than the diagnostic detection threshold (red arrow).

intensity threshold ($I_{\text{th}} \sim 4.2 \times 10^{14}$ W/cm²) is observed for the 18-beam configuration (OMEGA planar geometry). In spherical geometry, the intensity threshold is $\sim 3\times$ higher than for the four-beam configuration ($I_{\text{th}} \sim 6 \times 10^{14}$ W/cm²). These data underline the fact that the hot-electron intensity threshold depends strongly on the experimental configuration.

The measured rapid growth of the hot-electron fraction with the laser intensity is consistent with the exponential growth expected for convective TPD. This suggests that nonlinear mechanisms that may occur at low intensities are not sufficient to saturate the growth of the electron plasma waves. At higher intensities, the increase in the hot-electron fraction with laser intensity is reduced, suggesting that the TPD growth is affected by a nonlinear saturation mechanism.

Time-resolved data obtained with HXRD show that the hot-electron production occurs toward the end of the laser pulse. The instantaneous hot-electron fraction at the end of the pulse is typically a factor of ~ 2 higher than the value aver-

aged over the entire pulse.¹² These hot-electron measurements account for all electrons produced. In a fusion experiment, the hot-electron energy coupled to the core is expected to be significantly reduced by the divergence of the electrons angle and the variation in their energy.

Common-Wave Modeling

In this section, the resonant-TPD growth rate is calculated for multiple laser beams. The growth rate is shown to depend on the beam geometry, the beam polarization, and the sum of the intensities of the beams that share the same angle with the common electron plasma wave vector. For multiple laser beams with polarization smoothing, the maximum normalized growth rate is shown to be constant and independent of the geometry of the beams.

The multibeam coupling is relevant to calculations of both absolute growth or the convective TPD amplification. To interpret the experimental results described above, the convective gain was derived following the Rosenbluth method,^{14,31} which assumes that the common plasma wave propagates parallel to a linear density profile.

1. Multiple Linearly Polarized Beams

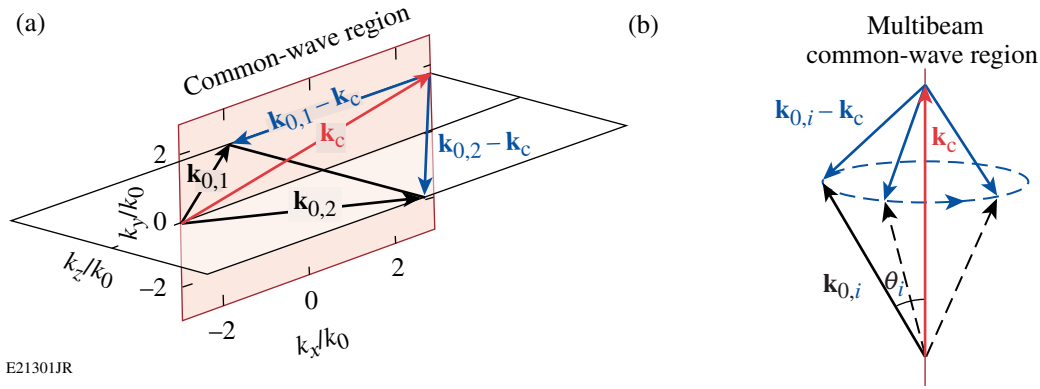
In the case of multiple laser beams driving a common electron plasma wave with frequency and wave vector (ω_c, \mathbf{k}_c), the dispersion relation for the common wave is $\omega_c^2 = \omega_{pe}^2 + 3\mathbf{k}_c^2 v_{\text{th},e}^2$ and for the corresponding daughter waves

$$(\omega_c - \omega_0)^2 = \omega_{pe}^2 + 3|\mathbf{k}_c - \mathbf{k}_{0,i}|^2 v_{\text{th},e}^2,$$

where $v_{\text{th},e}$ is the electron thermal velocity and ω_0 and $\mathbf{k}_{0,i}$ (with a magnitude k_0 independent of i) are the frequency and the wave vector of beam i . A common-wave region is defined where a resonant process exists and is determined by satisfying the dispersion relations for all laser beams and electron plasma waves leading to

$$\theta_i = \text{const}, \text{ for } i = 1 \dots n, \quad (1)$$

where θ_i is the angle between $\mathbf{k}_{0,i}$ and \mathbf{k}_c . All laser beams that drive a resonant common electron plasma wave must share the same angle with the common wave. For a two-beam configuration, Fig. 133.36(a) shows that this condition defines a plane in k space bisecting the wave vectors of the two laser beams. For more than two symmetrically oriented laser beams, Fig. 133.36(b) shows that this condition restricts the resonant common waves to a line.



E21301JR

Figure 133.36

(a) The common-wave region for two beams is given by a plane that bisects the wave vectors ($\mathbf{k}_{0,1}, \mathbf{k}_{0,2}$) of the laser beams (red plane). (b) A common electron plasma wave (EPW) can be driven only by multiple laser beams that share the same angle to the common-wave vector (θ_i) to satisfy the dispersion relation for each daughter EPW ($|\mathbf{k}_{0,i} - \mathbf{k}_c| = \text{const}$).

The dispersion relation for the common wave is derived following the TPD linear theory for the conditions where the collision frequency is much smaller than the growth rate

$$D(\omega_c, \gamma, |\mathbf{k}_c|) = - \sum_i \frac{(\gamma_{0,i}^2)^{\text{SB}}}{D(\omega_c - \omega_0, \gamma, |\mathbf{k}_c - \mathbf{k}_{0,i}|)}, \quad (2)$$

where the superscript SB refers to single beam, γ is the temporal growth rate,

$$D(\omega, \gamma, |\mathbf{k}|) = \left\{ \left[1 - \omega_{\text{pe}}^2 / \omega^2 (1 + 3k^2 \lambda_{\text{De}}^2) \right] \omega / 2 + i\gamma \right\}$$

is the dispersion relation, $\lambda_{\text{De}} = v_{\text{th},e} / \omega_{\text{pe}}$ is the Debye length, and ω_{pe} is the electron plasma frequency. The single-beam growth rate is given by $(\gamma_{0,i}^2)^{\text{SB}} = f_c (\gamma_{0,i}^2)_{\text{max}}^{\text{SB}} \cos^2 \alpha$, where α is the angle between the electric-field polarization vector and the common-wave vector and

$$f_c = \left[(k_c^2 - |\mathbf{k}_c - \mathbf{k}_0|^2) / k_0 |\mathbf{k}_c - \mathbf{k}_0| \right]^2.$$

The maximum single-beam growth rate squared is

$$(\gamma_{0,\text{max}}^2)^{\text{SB}} = 2 / (cn_e m_e) (k_0/2)^2 I_i,$$

where c is the light velocity, m_e is the electron mass, $n_c = m_e \omega_0^2 / 4\pi e^2$ is the critical density, and e is the electron charge.

To evaluate the maximum value of the growth rate, the minimum value of $D(\omega, \gamma, |\mathbf{k}_c - \mathbf{k}_{0,i}|)$ is determined by ensuring that the dispersion relations for all daughter

waves are satisfied [i.e., Eq. (1) is satisfied]. It follows that $D(\omega_c - \omega_0, \gamma, |\mathbf{k}_c - \mathbf{k}_{0,i}|) = \gamma = \text{const}$ and the temporal growth rate is given from Eq. (2) by

$$(\gamma_0^2)^{\text{MB}} = \sum_i (\gamma_{0,i}^2)^{\text{SB}}. \quad (3)$$

The common-wave growth rate is normalized to the maximum single-beam growth rate calculated for the overlapped intensity of the beams contributing to the common wave (I_Σ):

$$(\Gamma_0^2)^{\text{MB}} = \frac{(\gamma_0^2)^{\text{MB}}}{(\gamma_0^2)_{\text{max}}^{\text{SB}, I_\Sigma}} = f_c \sum_i \cos^2(\alpha_i) \beta_i, \quad (4)$$

where $\beta_i = I_i / I_\Sigma$, I_i is the intensity of the laser beam i , and α_i is the angle between the electric-field polarization vector and the common-wave vector. To determine the dominant common electron plasma wave, a maximum normalized growth rate $[(\Gamma_0^2)_{\text{max}}^{\text{MB}}]$ is calculated that depends only on the geometry and polarizations of the laser beams. The convective gain is given by

$$G_c = 6 \times 10^{-2} \frac{I_\Sigma L_n \lambda_0}{T_e} (\Gamma_0^2)_{\text{max}}^{\text{MB}}, \quad (5)$$

where I_Σ is in units of 10^{14} W/cm², L_n is in μm , T_e is in keV, and λ_0 is the laser wavelength in μm .

2. Multibeams with Polarization Smoothing

For more than two beams, the common-wave region defines a line [I_c displayed in Figs. 133.37(a) and 133.37(b)] and the growth rate for multiple beams is equal to the sum of the

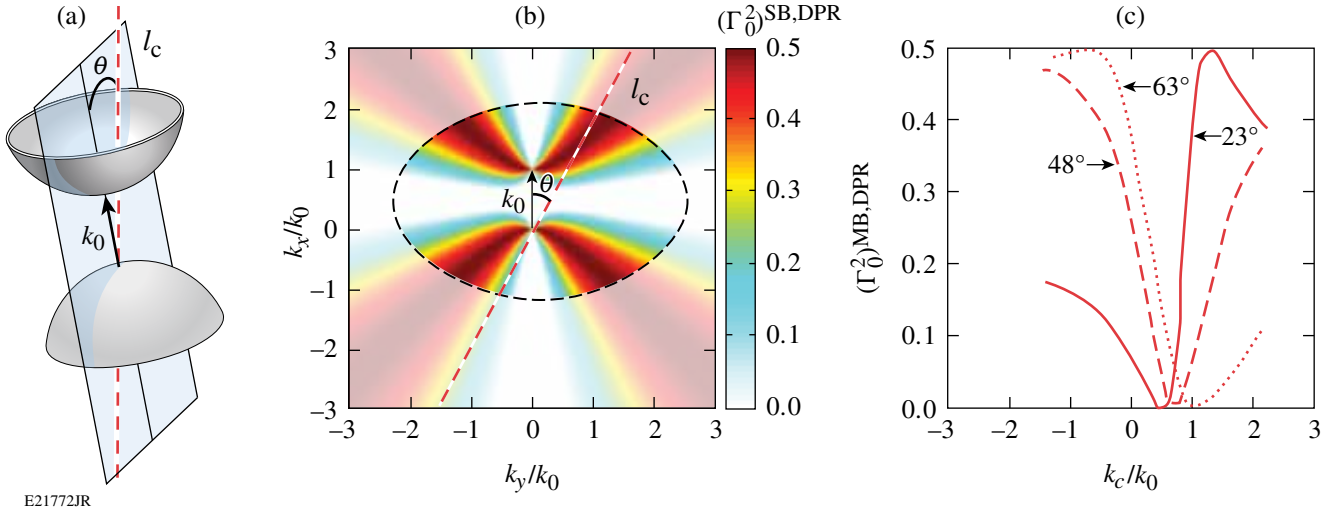


Figure 133.37

(a) A 3-D representation of the maximum growth rate for a single beam with polarization smoothing (gray hyperboloids). Multiple beams with polarization smoothing can couple through the common wave along the common-wave line (l_c , red dashed line) at an angle θ . (b) Normalized single-beam with polarization smoothing growth rate in the plane (\mathbf{k}_0, l_c). The Landau cutoff ($k\lambda_{De} = 0.25$, where k is the maximum value between k_c and $|\mathbf{k}_c - \mathbf{k}_0|$) for $T_e = 2$ keV is represented with a black dashed line. The normalized multibeam growth rate is equal to the single-beam growth rate along l_c . (c) Normalized multibeam growth rate calculated along the common-wave line for $\theta = 23^\circ$ (solid red line), $\theta = 48^\circ$ (dashed red line), and $\theta = 63^\circ$ (dotted red line). The cutoff for small and large \mathbf{k}_c corresponds to the Landau cutoff calculated for $T_e = 2$ keV.

growth rate for a single beam along this line [applying Eq. (3)]. Since the growth rate is azimuthally symmetric around \mathbf{k}_0 for each beam (Appendix A) and Eq. (1) must be satisfied, the growth rate along l_c is equal for each beam. The growth rate for multiple beams is given by the single-beam growth rate times the number of beams (N_Σ) that can drive the common wave $\left[(\gamma_0^2)^{\text{MB,PS}} = N_\Sigma (\gamma_0^2)^{\text{SB,PS}} \right]$. The multibeam growth rate is normalized to the maximum single-beam growth rate $\left[(\gamma_0^2)_{\text{max}}^{\text{SB,IS}} = N_\Sigma (\gamma_0^2)_{\text{max}}^{\text{SB,IS}} \right]$, resulting in a factor that depends only on the beam geometry

$$(\Gamma_0^2)^{\text{MB,PS}} = (\Gamma_0^2)^{\text{SB,PS}} = \frac{1}{2} f_c \sin^2 \theta. \quad (6)$$

To determine the maximum normalized growth rate, the common-wave line is plotted over the top of the single-beam growth rate calculated in the plane (\mathbf{k}_0, l_c) [Fig. 133.37(b)]. The multibeam normalized growth rate along the common-wave line is plotted in Fig. 133.37(c) for three angles. For most conditions, the common-wave line crosses the maximum normalized single-beam growth rate: for small values of θ [solid red curve in Fig. 133.37(c)], the common-wave line crosses the upper hyperbola and for large values of θ [dotted red line in Fig. 133.37(c)], the common-wave line crosses the lower hyperbola. In these two cases, the maximum normalized

multibeam growth rate with PS is $(\Gamma_0^2)_{\text{max}}^{\text{MB,PS}} = 0.5$. When the common-wave line does not intersect the hyperbola, the maximum normalized multibeam growth rate is slightly reduced [dashed red line in Fig. 133.37(c)]. The range of angles where the common-wave line does not cross the hyperbolas is given by the Landau cutoff and is, in general, small. The common-wave gain for multibeams with PS is given by

$$G_c^{\text{PS}} = 3 \times 10^{-2} \frac{I_\Sigma L_n \lambda_0}{T_e} \quad (7)$$

and, contrary to the gain in the case of polarized beams, does not depend on the geometry of the beams except as noted above. These results are consistent with the initial experiments that demonstrate multibeam effects on hot-electron generation.¹⁵

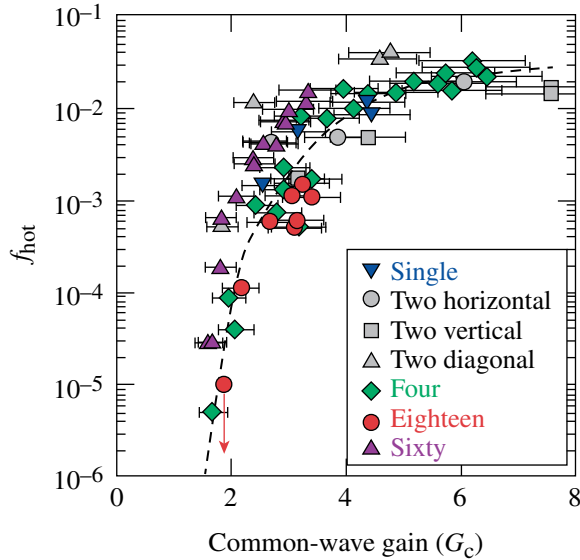
Interpretation of Experimental Results

In this section, the experimental results are discussed in the context of the common-wave model, where each experimental configuration was designed to vary a different parameter in the gain $\left[(\Gamma_0^2)_{\text{max}}^{\text{MB}}, N_\Sigma / N_{\text{beam}}, \text{ and } L_{n,q} / T_{e,q} \text{ (Table 133.VI)} \right]$. Figure 133.38 shows that the common-wave gain reproduces the measured hot-electron intensity thresholds shown in Fig. 133.35. For all laser-beam configurations, a gain threshold of ~ 2 is observed and a saturation is measured for $G_c \gtrsim 3$. This thresh-

Table 133.VI: List of parameters defining the common-wave gain that were varied during the experiments. N_Σ is the number of beams that share an equivalent angle with the common electron plasma wave [see Eq. (3)] with the largest growth rate, $L_{n,q}/T_{e,q}$ is in units of $\mu\text{m}/\text{keV}$; $(I_{\Sigma,q})_{\text{th}}^{\text{MB}}$ is in units of $10^{14} \text{ W}/\text{cm}^2$.

Configuration	N_{beam}	$(\Gamma_0^2)_{\text{max}}^{\text{MB}}$	N_Σ	$L_{n,q}/T_{e,q}$	$(I_{\Sigma,q})_{\text{th}}^{\text{MB}}$
Single	1	1.0	1	175	0.5
Two vertical	2	1.0	2	175	0.5
Two horizontal	2	0.8	2	175	0.7
Two diagonal	2	0.6	2	175	0.9
Four	4	0.5	4	175	1.1
Eighteen	18	0.5	6	135	1.4
Sixty	60*	0.5	6	60	3.1

*The number of beams that contribute in spherical geometry on OMEGA to the total overlapped intensity is ~ 20 .



E21699JR2

Figure 133.38
The hot-electron fraction is plotted as a function of the common-wave gain for each experimental configuration tested.

old is about $5\times$ lower than required for significant convective amplification from thermal noise. This discrepancy could be attributed to enhanced Langmuir wave noise, modified density profiles,³² or laser speckles.³³

The experimental results can be used to calculate an intensity threshold for hot-electron production from Eq. (5), when the convective gain is equal to 2, given by

$$(I_{\Sigma,q})_{\text{th}}^{\text{MB}} = \frac{94}{(L_{n,q}/T_{e,q})(\Gamma_0^2)_{\text{max}}^{\text{MB}}}. \quad (8)$$

The intensity threshold for the different configurations is computed in Table 133.VI.

1. Beam Geometry and Polarization

On OMEGA EP, the maximum normalized growth rate was varied between the different configurations by changing the beam geometry and polarization while the other parameters remained constant (Table 133.VI). For the one- and two-beam configurations, a similar hot-electron production as a function of intensity is observed (Fig. 133.35). This demonstrates that for the two-beam configuration, the TPD is driven by a multi-beam process. For the four-beam configuration, the observed factor-of-2 increase in the intensity threshold (Fig. 133.35) is explained by the factor-of-2 decrease in the maximum normalized growth rate (Eq. 4) (Ref. 21).

The spectrum in k space where the normalized growth rate is maximum is larger for the single-beam configuration than for the two-beam configuration, whereas the maximum normalized growth rate is similar. The fact that the hot-electron fraction produced by the one-beam and two-beam configurations is similar suggests that the k -space volume of the large EPW's plays a minor role in the generation of hot electrons and that the hot-electron production depends, to first order, on the maximum normalized growth rate.

2. Number of Contributing Beams

In the 18-beam configuration on OMEGA, only a third of the beams contribute to the common-wave process, and the intensity that contributes to the maximum growth rate is reduced by 50% from the total overlapped intensity at the quarter-critical density. This is the primary explanation for the experimentally observed increase in the overlapped intensity threshold

(Fig. 133.35), where the beams are arranged in three cones of six at three different angles. As a result of the common-wave condition [Eq. (1)], each cone drives a different common wave and the coupling that dominates the TPD growth is the one with the largest growth rate. Since the beams were smoothed by polarization smoothing in this experiment, the coupling with the largest growth rate corresponds to the cone that has the highest intensity at the quarter-critical density. *LILAC* simulations indicate that the beams in the 23° cone have the highest intensity at the quarter-critical density ($I_{\Sigma,q}^{23^\circ} = 0.6 I_{\text{OVR},q}$, $I_{\Sigma,q}^{48^\circ} = 0.3 I_{\text{OVR},q}$, and $I_{\Sigma,q}^{63^\circ} = 0.1 I_{\text{OVR},q}$). This result is consistent with the experiments reported in Ref. 8, where the hot-electron generation was shown to depend only on the intensity of the beams of a single cone.

3. Plasma Parameters

The difference in the 18-beam and 60-beam thresholds observed in Fig. 133.35 is primarily a result of the difference in the plasma parameters, $L_{n,q}/T_{e,q}$ (Table 133.VI). For the spherical results, the maximum number of beams that are symmetrically oriented is six, arranged in a hexagon [a nine-beam coupling also exists but the large angle between the target normal and the beams (63°) significantly reduces their intensity at quarter-critical density]. As in the OMEGA planar experiments, the beams in the 23° cone produce the largest common-wave gain.

Conclusions

These experimental results indicate that the hot-electron threshold depends on the hydrodynamic parameters at the quarter-critical density, the configuration of the laser beams, and the sum of the intensity of the beams that share the same angle with the common-wave vector. A TPD model where multiple laser beams can share a common electron plasma wave has been presented. The resonant common-wave process occurs only when the multiple laser beams share the same angle with the common EPW. This creates a common-wave region where a maximum growth rate defines the dominant EPW, independent of the plasma conditions. To compare with the experimental results, the maximum common-wave growth rate is used to calculate a convective gain.

The experiments were designed to measure the threshold for hot-electron production while varying the different parameters [N_Σ , $(\Gamma_0^2)_{\text{max}}^{\text{MB}}$, I_s , L_n/T_e] in the common-wave gain. A significant increase in the hot-electron intensity threshold was observed when the maximum normalized growth rate was reduced by using four beams compared to one or two beams. A further reduction was observed when the number of beams that

can contribute to the common wave was reduced by distributing 18 beams into three cones. The overlapped intensity threshold was observed to be different for the various experimental configurations and is explained by the common-wave TPD model.

The common-wave theory is consistent with the initial experiments that first demonstrated multibeam effects on hot-electron generation.¹⁵ In these experiments, the hot-electron fraction was shown to be independent of the number of beams. The beams that were varied were from the same cone and therefore shared the same common plasma wave. These results can be applied to the indirect-drive experiments reported in Ref. 8 that showed the dependence of hot-electron generation on the intensity of the beams in a single cone.

ACKNOWLEDGMENT

This work was supported by the U.S. Department of Energy Office of Inertial Confinement Fusion under Cooperative Agreement No. DE-FC52-08NA28302, the University of Rochester, and the New York State Energy Research and Development Authority. The support of DOE does not constitute an endorsement by DOE of the views expressed in this article.

Appendix A: Single Beam with Polarization Smoothing

Polarization smoothing employs a birefringent crystal that separates the incident linearly polarized laser beam into two beams with orthogonal polarizations propagating at a slight angle ($\sim 40 \mu\text{rad}$) with respect to each other. The angle is small compared to the f number (25 mrad) of the laser beam so that the k -vectors of the two beams can be treated equivalently. From the normalized common-wave growth rate [Eq. (4)] and the fact that the intensity is equivalent between the two polarizations ($I_\parallel = I_\perp = I_\Sigma/2$), the normalized growth rate for a single beam with a PS is given by

$$\begin{aligned} (\Gamma_0^2)^{\text{SB,PS}} &= f_c \left[\frac{I_\parallel}{I_\Sigma} \cos^2(\alpha_\parallel) + \frac{I_\perp}{I_\Sigma} \cos^2(\alpha_\perp) \right] \\ &= 0.5 f_c \sin^2(\theta), \end{aligned} \quad (\text{A1})$$

where \parallel (\perp) refers to the parallel (perpendicular) polarized beam, and from Fig. 133.39, it is apparent that

$$\begin{aligned} \cos^2(\alpha_\parallel) + \cos^2(\alpha_\perp) &= \frac{(\mathbf{k}_c \cdot \mathbf{e}_\parallel)^2 + (\mathbf{k}_c \cdot \mathbf{e}_\perp)^2}{k_c^2} \\ &= \frac{\mathbf{k}_c^2}{k_c^2} = \sin^2 \theta, \end{aligned} \quad (\text{A2})$$

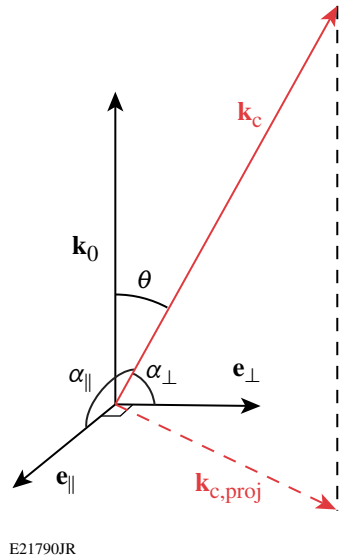


Figure 133.39
The projection of the common-wave vector \mathbf{k}_c in the plane $(\mathbf{e}_{\parallel}, \mathbf{e}_{\perp})$ for a single beam with a polarization smoothing (PS).

where \mathbf{e}_{\parallel} (\mathbf{e}_{\perp}) is the polarization vector of the parallel (perpendicular) polarized beam and $\mathbf{k}_{c,\text{proj}}$ is the projection of \mathbf{k}_c onto the plane $(\mathbf{e}_{\parallel}, \mathbf{e}_{\perp})$.

Equation (A1) shows that for a single beam with polarization smoothing, the growth rate in k space is symmetric around \mathbf{k}_0 (f_c depends only on $|\mathbf{k}_c|$, $|\mathbf{k}_0|$, and $|\mathbf{k}_c - \mathbf{k}_0|$). When \mathbf{k}_c is in the plane $(\mathbf{k}_0, \mathbf{e}_{\parallel})$, the term $\mathbf{k}_c \cdot \mathbf{e}_{\perp}$ cancels out and the normalized growth rate is simply equal to half the normalized growth rate for a beam with parallel polarization calculated in the polarization plane. Due to symmetry, the maximum growth rate is 0.5 and in k space defines two hyperboloids [Fig. 133.37(a)]. In each plane that contains \mathbf{k}_0 , the growth rate is equal to half the growth rate calculated for a linearly polarized single beam calculated in the polarization plane [Fig. 133.37(b)].

REFERENCES

1. J. Nuckolls *et al.*, *Nature* **239**, 139 (1972).
2. R. L. McCrory, D. D. Meyerhofer, R. Betti, R. S. Craxton, J. A. Delettrez, D. H. Edgell, V. Yu. Glebov, V. N. Goncharov, D. R. Harding, D. W. Jacobs-Perkins, J. P. Knauer, F. J. Marshall, P. W. McKenty, P. B. Radha, S. P. Regan, T. C. Sangster, W. Seka, R. W. Short, S. Skupsky, V. A. Smalyuk, J. M. Soures, C. Stoeckl, B. Yaakobi, D. Shvarts, J. A. Frenje, C. K. Li, R. D. Petrasso, and F. H. Séguin, *Phys. Plasmas* **15**, 055503 (2008).
3. J. D. Lindl *et al.*, *Phys. Plasmas* **11**, 339 (2004).
4. M. V. Goldman, *Ann. Phys.* **38**, 117 (1966).
5. C. S. Liu and M. N. Rosenbluth, *Phys. Fluids* **19**, 967 (1976).
6. A. Simon, R. W. Short, E. A. Williams, and T. Dewandre, *Phys. Fluids* **26**, 3107 (1983).
7. W. Seka, D. H. Edgell, J. F. Myatt, A. V. Maximov, R. W. Short, V. N. Goncharov, and H. A. Baldis, *Phys. Plasmas* **16**, 052701 (2009).
8. S. P. Regan, N. B. Meezan, L. J. Suter, D. J. Strozzi, W. L. Krueer, D. Meeker, S. H. Glenzer, W. Seka, C. Stoeckl, V. Yu. Glebov, T. C. Sangster, D. D. Meyerhofer, R. L. McCrory, E. A. Williams, O. S. Jones, D. A. Callahan, M. D. Rosen, O. L. Landen, C. Sorce, and B. J. MacGowan, *Phys. Plasmas* **17**, 020703 (2010).
9. D. W. Phillion *et al.*, *Phys. Rev. Lett.* **49**, 1405 (1982).
10. J. F. Myatt, J. Zhang, J. A. Delettrez, A. V. Maximov, R. W. Short, W. Seka, D. H. Edgell, D. F. DuBois, D. A. Russell, and H. X. Vu, *Phys. Plasmas* **19**, 022707 (2012).
11. R. Yan, C. Ren, J. Li, A. V. Maximov, W. B. Mori, Z. M. Sheng, and F. S. Tsung, *Phys. Rev. Lett.* **108**, 175002 (2012).
12. D. H. Froula, B. Yaakobi, S. X. Hu, P.-Y. Chang, R. S. Craxton, D. H. Edgell, R. Follett, D. T. Michel, J. F. Myatt, W. Seka, R. W. Short, A. Solodov, and C. Stoeckl, *Phys. Rev. Lett.* **108**, 165003 (2012).
13. *LLE Review Quarterly Report* **79**, 131, Laboratory for Laser Energetics, University of Rochester, Rochester, NY, LLE Document No. DOE/SF/19460-317, NTIS Order No. DE2002762802 (1999). (Copies may be obtained from the National Technical Information Service, Springfield, VA 22161.)
14. R. Yan, A. V. Maximov, C. Ren, and F. S. Tsung, *Phys. Rev. Lett.* **103**, 175002 (2009).
15. C. Stoeckl, R. E. Bahr, B. Yaakobi, W. Seka, S. P. Regan, R. S. Craxton, J. A. Delettrez, R. W. Short, J. Myatt, A. V. Maximov, and H. Baldis, *Phys. Rev. Lett.* **90**, 235002 (2003).
16. A. V. Maximov, J. Myatt, R. W. Short, W. Seka, and C. Stoeckl, *Bull. Am. Phys. Soc.* **52**, 195 (2007).
17. R. W. Short, *Bull. Am. Phys. Soc.* **53**, 245 (2008).
18. T. R. Boehly, D. L. Brown, R. S. Craxton, R. L. Keck, J. P. Knauer, J. H. Kelly, T. J. Kessler, S. A. Kumpan, S. J. Loucks, S. A. Letzring, F. J. Marshall, R. L. McCrory, S. F. B. Morse, W. Seka, J. M. Soures, and C. P. Verdon, *Opt. Commun.* **133**, 495 (1997).
19. J. H. Kelly, L. J. Waxer, V. Bagnoud, I. A. Begishev, J. Bromage, B. E. Kruschwitz, T. J. Kessler, S. J. Loucks, D. N. Maywar, R. L. McCrory, D. D. Meyerhofer, S. F. B. Morse, J. B. Oliver, A. L. Rigatti, A. W. Schmid, C. Stoeckl, S. Dalton, L. Folsbee, M. J. Guardalben, R. Jungquist, J. Puth, M. J. Shoup III, D. Weiner, and J. D. Zuegel, *J. Phys. IV France* **133**, 75 (2006).
20. D. H. Froula, D. T. Michel, I. V. Igumenshchev, S. X. Hu, B. Yaakobi, J. F. Myatt, D. H. Edgell, R. Follett, V. Yu. Glebov, V. N. Goncharov, T. J. Kessler, A. V. Maximov, P. B. Radha, T. C. Sangster, W. Seka, R. W. Short, A. A. Solodov, C. Sorce, and C. Stoeckl, *Plasma Phys. Control. Fusion* **54**, 124016 (2012).

21. D. T. Michel, A. V. Maximov, R. W. Short, S. X. Hu, J. F. Myatt, W. Seka, A. A. Solodov, B. Yaakobi, and D. H. Froula, *Phys. Rev. Lett.* **109**, 155007 (2012).
22. T. J. Kessler, Y. Lin, J. J. Armstrong, and B. Velazquez, in *Laser Coherence Control: Technology and Applications*, edited by H. T. Powell and T. J. Kessler (SPIE, Bellingham, WA, 1993), Vol. 1870, pp. 95–104.
23. T. R. Boehly, V. A. Smalyuk, D. D. Meyerhofer, J. P. Knauer, D. K. Bradley, R. S. Craxton, M. J. Guardalben, S. Skupsky, and T. J. Kessler, *J. Appl. Phys.* **85**, 3444 (1999).
24. P. B. Radha, T. J. B. Collins, J. A. Delettrez, Y. Elbaz, R. Epstein, V. Yu. Glebov, V. N. Goncharov, R. L. Keck, J. P. Knauer, J. A. Marozas, F. J. Marshall, R. L. McCrory, P. W. McKenty, D. D. Meyerhofer, S. P. Regan, T. C. Sangster, W. Seka, D. Shvarts, S. Skupsky, Y. Srebro, and C. Stoeckl, *Phys. Plasmas* **12**, 056307 (2005).
25. J. Delettrez, *Can. J. Phys.* **64**, 932 (1986).
26. B. Yaakobi, P.-Y. Chang, A. A. Solodov, C. Stoeckl, D. H. Edgell, R. S. Craxton, S. X. Hu, J. F. Myatt, F. J. Marshall, W. Seka, and D. H. Froula, *Phys. Plasmas* **19**, 012704 (2012).
27. B. Yaakobi, C. Stoeckl, T. Boehly, D. D. Meyerhofer, and W. Seka, *Phys. Plasmas* **7**, 3714 (2000).
28. B. Yaakobi, C. Stoeckl, W. Seka, J. A. Delettrez, T. C. Sangster, and D. D. Meyerhofer, *Phys. Plasmas* **12**, 062703 (2005).
29. C. Stoeckl, V. Yu. Glebov, D. D. Meyerhofer, W. Seka, B. Yaakobi, R. P. J. Town, and J. D. Zuegel, *Rev. Sci. Instrum.* **72**, 1197 (2001).
30. I. Kawrakow *et al.*, NRC, Ottawa, Canada, NRCC Report PIRS-701 (May 2011).
31. M. N. Rosenbluth, *Phys. Rev. Lett.* **29**, 565 (1972).
32. D. R. Nicholson and A. N. Kaufman, *Phys. Rev. Lett.* **33**, 1207 (1974).
33. G. Laval, R. Pellat, and D. Pesme, *Phys. Rev. Lett.* **36**, 192 (1976).

Mitigation of Cross-Beam Energy Transfer: Implications of Two-State Optical Zooming on OMEGA

Introduction

Two approaches to inertial confinement fusion (ICF)¹ employ megajoule-class laser systems^{2,3} to compress a fusion capsule to thermonuclear burn conditions. For the indirect-drive approach,⁴ the laser beams heat a radiation cavity, crossing in a low-density plasma on their path to the cavity wall; for the direct-drive approach,^{5,6} the laser beams directly illuminate the fusion capsule and laser rays cross in higher-density coronal plasma. In both ignition schemes, crossing laser beams can excite ion-acoustic waves that facilitate the energy transfer away from regions of interest.^{7–11}

For indirect-drive-ignition experiments, cross-beam energy transfer (CBET) removes significant energy from the beams directed near the equator of the capsule, compromising the symmetry of the implosion.¹⁰ By changing the relative frequency between the laser beams, CBET has been mitigated and frequency shifts are now used to control the symmetry of the fusion capsule at the National Ignition Facility.^{12–14}

Direct-drive implosions on the OMEGA laser¹⁵ use three ~100-ps-long laser pulses (“pickets”) to launch shocks into the target, setting the implosion onto a low adiabat.⁶ These picket pulses are followed by a high-intensity drive pulse that compresses the fuel. During the drive, experiments have shown that CBET can reduce the hydrodynamic coupling by linking the scattered-light spectra to a lack of energy penetrating to the critical surface.^{16,17} Laser light in the edge of the laser beams propagating past the target beats with the incident laser light from the opposing beams and excites ion-acoustic waves. The enhanced ion-acoustic waves scatter light primarily from the central rays of the incident laser beams to the outgoing rays.

Studies have shown that reducing the diameter of the laser beams by 30% can restore 70% of the energy lost to CBET at the cost of reduced hydrodynamic stability.¹⁸ Simulations indicate no deleterious effects on hydrodynamic stability when the laser-beam diameters are reduced after a significant thermal conduction zone has been generated (two-state zooming). Zooming is predicted to increase the hydrodynamic efficiency,

allowing OMEGA to drive more-stable implosions at higher velocities and ignition-relevant, one-dimensional (1-D) yields.¹⁹

Potential schemes to achieve zooming of the focal spot on target involve modifications to the spatial coherence of the laser that cause broadening in the far field of the beam.²⁰ Two primary options for implementing zooming on OMEGA were investigated: (1) time-dependent phase conversion and (2) increased deflection from two-dimensional (2-D) smoothing by spectral dispersion (SSD).²¹ The most-practical method for implementing zooming on OMEGA appears to be time-dependent phase conversion. It is predicted to increase the absorption and allow for designs that include 9.5 μm of carbon–deuterium (CD) polymer and 66- μm -thick deuterium–tritium (DT) shells to be driven at $\sim 3.2 \times 10^7$ cm/s and produce ignition-scalable 1-D yields of 7.8×10^{13} —a factor of ~ 2.5 larger yields than produced without zooming. Implementing time-dependent phase conversion on OMEGA will require zooming phase plates (ZPP’s) and co-propagating dual-driver lines.

1. Zooming Phase Plates

A new phase-plate design, referred to as a zooming phase plate (ZPP), in conjunction with a time-dependent near-field profile will produce a larger laser spot during the pickets and a smaller laser spot during the main drive. The ZPP would contain a radial transition where the central area produces a larger, low-order super-Gaussian focal spot, while the outer area produces a smaller, high-order super-Gaussian focal spot. This configuration requires a smaller-diameter beam during the pickets and a mid-section cutout of the near field during the drive pulse, as shown in Fig. 133.40(a). OMEGA operates near its maximum stored-energy capacity, requiring that the diameter of the laser beams during the drive fill the complete aperture [Fig. 133.40(b)]. The OMEGA-limited near-field profiles combined with the proposed ZPP’s produce laser spots with low-intensity wings.

2. Co-Propagating Dual-Driver Lines

To produce the required two-state near-field profile, a co-propagating dual-driver configuration is required. The picket

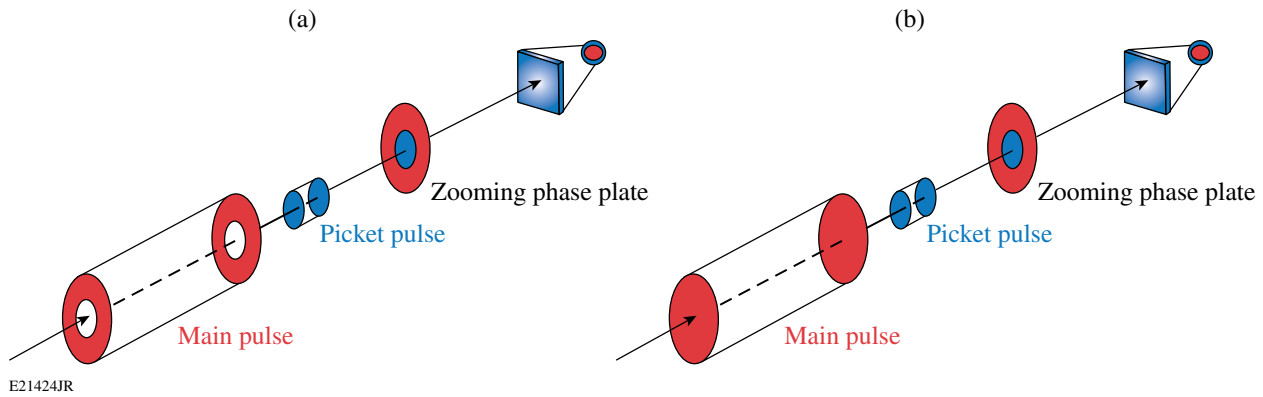


Figure 133.40

The (a) optimum and (b) OMEGA-limited near-field profiles for implementing radially varying ZPP's to produce large-diameter laser spots during the pickets (blue) and small-diameter spots during the drive pulse (red).

driver with SSD would pass through an apodizer, forming a beam of half the standard diameter. The second main-pulse driver would propagate without SSD through its own apodizer, forming a full-diameter beam [Fig. 133.40(b)].

Introducing a dual-driver configuration will provide the following:

- a 14-cm-diam beam during the pickets ($1.5\text{-}\text{\AA} \times 3\text{-}\text{\AA}$ SSD) and a full-aperture, 28-cm-diam beam (no SSD) during the main drive;
- an $\sim 10\%$ increase in on-target energy as a result of better frequency-conversion efficiency; and
- a proof-of-principle dynamic bandwidth reduction for the National Ignition Facility (NIF).

Implementing zooming using the proposed method presents two main concerns: (1) The small-diameter beams required during the pickets will increase intensity modulations in the imprint spectrum by a factor of 1.5 to 2. The impact of this increased imprint will be investigated but recent mitigation studies have demonstrated a factor-of-2 imprint reduction when using doped ablaters.^{22,23} (2) Zooming increases the single-beam intensities ($\sim 2\times$) during the drive. This may be above the backscatter intensity thresholds and lead to larger levels of hot electrons produced by two-plasmon decay.

This article is organized as follows: The target-physics implications of CBET and the initial results that are the foundation for a CBET mitigation scheme are described; a CBET mitigation scheme for direct-drive implosions, reviews of the physics considerations, and requirements for implementing this scheme on OMEGA are presented; proposed physics studies

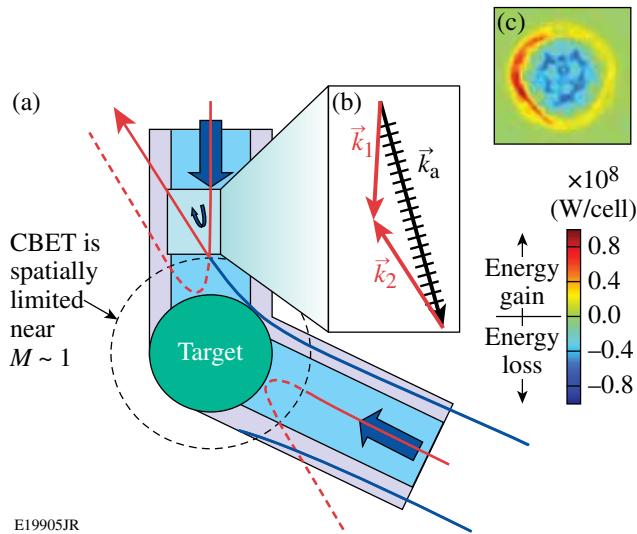
to be completed prior to implementing the scheme are summarized; implementation of zooming on OMEGA is discussed; and the findings are summarized. An appendix presents an alternative concept for zooming (increased deflection from 2-D SSD) and the related calculations used to assess its feasibility.

Target Physics

1. Implications of Cross-Beam Energy Transfer in Direct Drive

The direct-drive approach to inertial confinement fusion requires that the laser beams efficiently deposit their energy in the coronal plasma where the energy is transported through the conduction zone to the ablation surface, producing the pressure that drives the implosion. This ablation pressure (P_a) determines the minimum laser energy required for ignition ($E_{\min} \propto P_a^{-2}$) (Ref. 24). Reducing the diameter of the laser beams increases the ablation pressure because it increases the energy in the central portions of the laser beams that propagate most normal to the target surface and deposit their energy closest to the ablation surface. This is balanced by the required increase in the diameter of the laser beams to minimize the illumination nonuniformities on target.

CBET is a mechanism that reduces the ablation pressure in direct-drive implosions.^{11,16–18} It reduces the incident energy in the central portion of the laser beams, making it possible for the incoming light to bypass the highest-absorption region near the critical surface (Fig. 133.41), significantly reducing the hydrodynamic efficiency.¹⁷ Laser light in the edge of the laser beams (\vec{k}_2) propagating past the target seeds stimulated Brillouin scattering (SBS) using light from the opposing laser beams (\vec{k}_1) and drives ion-acoustic waves (\vec{k}_a). The ion-acoustic waves scatter light primarily from the central rays of the incident laser beams to the lower-energy outgoing rays.



E19905JR

Figure 133.41

(a) Light rays propagating past the target (blue) interact with light rays in the central region of another beam (red). (b) The interacting light rays seed an ion-acoustic wave near the Mach-1 surface (dashed curves). The ion-acoustic wave scatters light before it can penetrate deep into the target. (c) A calculation of the total energy transferred (gain/lost) integrated along the path of a ray into and out of the target. The calculation shows that energy in the central rays propagating into the target is reduced by CBET, while the energy in the edges of the beam propagating away from the target is increased.²⁵

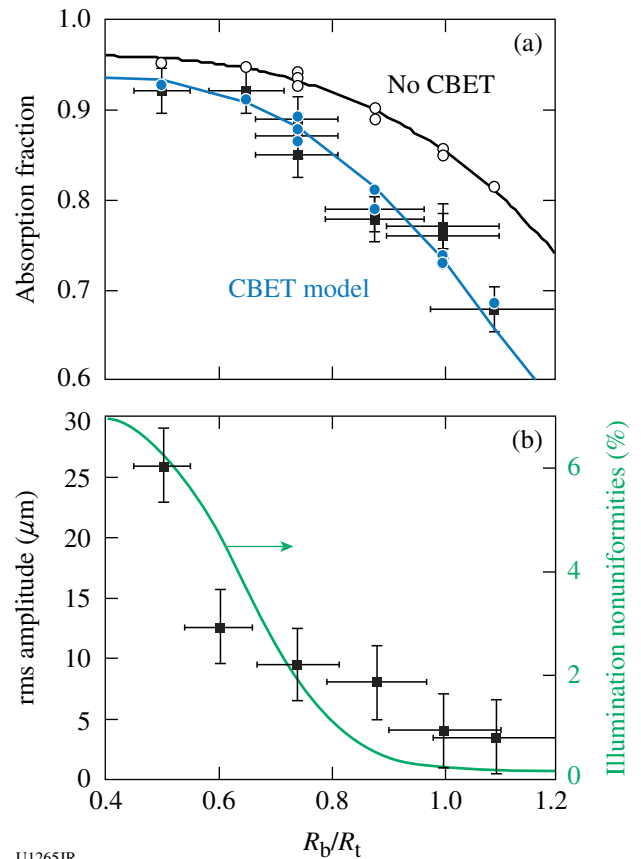
Simulations of direct-drive implosions using the 1-D radiation–hydrodynamics code *LILAC*²⁶ that include CBET modeling indicate that the ablation pressure is reduced by $\sim 40\%$, lowering the implosion velocity ($v_{\text{imp}} \propto P_a$), the hot-spot pressure ($P_{\text{hs}} \propto P_a^{1/3}$), the areal density ($\rho R \propto \sqrt{P_a}$), and negatively impacting the stability of the implosion as inferred from the in-flight aspect ratio (IFAR $\propto P_a^{-2/5}$) (Ref. 24). The loss in ablation pressure limits OMEGA cryogenic implosions, reducing the 1-D yield by nearly an order of magnitude.

The implosion velocity calculated for a 1.5-MJ, symmetric, direct-drive–ignition design⁶ is reduced from 4.0×10^7 to 3.3×10^7 cm/s (Ref. 19). CBET significantly increases the minimum energy required for ignition and 1-D simulations suggest that the ignition margin cannot be recovered by increasing the on-target laser energy while maintaining a constant overlapped intensity. Increasing the laser energy to account for the lost ablation pressure requires an increased laser-beam radius that results in longer scale lengths and increased CBET. The increased energy does not recover the loss in hot-spot pressure, suggesting that the implosions must be driven at higher velocities, further reducing their hydrodynamic stability.

2. Mitigation of Cross-Beam Energy Transfer (Zooming)

Experiments have demonstrated that reducing the laser-beam diameters with respect to the target diameter can reduce CBET at the cost of increased illumination nonuniformities (Fig. 133.42).¹⁸ To mitigate CBET and maintain sufficient illumination uniformity, a two-state zooming has been proposed.¹⁹ During the critical time for seeding nonuniformities, the radii of the laser beams R_b are equal to the target radius R_t ($R_b/R_t = 1$), minimizing the low-frequency laser imprint. Once a conduction zone is long enough to suitably smooth laser imprint, the diameters of the laser beams are reduced and CBET can be mitigated.

LILAC simulations show that implementing zooming by reducing the 95% encircled energy radii of the laser beams after the third picket from $R_b = 430 \mu\text{m}$ ($R_b/R_t = 1.0$) to $R_b = 365 \mu\text{m}$



U1265JR

Figure 133.42

The measured (a) absorbed light (squares) and (b) rms deviation from the average shell radius (squares, left axis), along with the calculated illumination nonuniformities (right axis) are plotted as functions of the ratio between the laser-beam and target radii, where R_b is the 95% encircled energy radius. The calculated absorption is shown in (a) for simulations with (blue solid circles) and without CBET modeling (open circles) for an overlapped intensity of 4.5×10^{14} W/cm² (Ref. 17).

($R_b/R_t = 0.85$) recovers 35% of the absorption lost to CBET and the implosion velocity for less-massive targets ($10 \mu\text{m}$ of CD + $44\text{-}\mu\text{m}$ -thick DT shells) reaches values of $3.7 \times 10^7 \text{ cm/s}$ [Fig. 133.43(a)]. Further reducing the radii of the laser beams to $R_b = 300 \mu\text{m}$ ($R_b/R_t = 0.7$) recovers 70% of the energy lost to

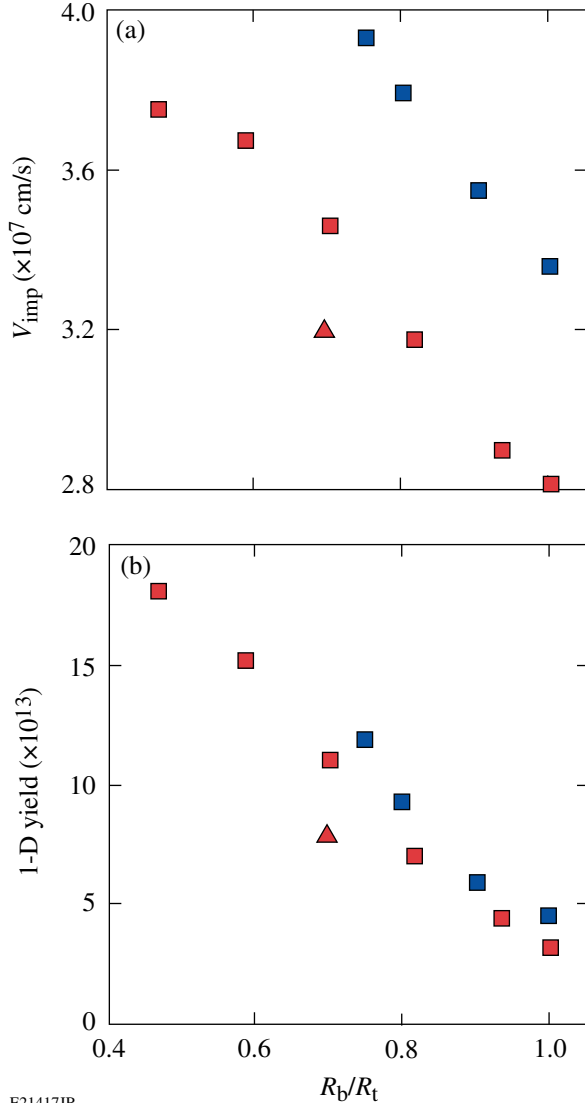
CBET. Figure 133.43 shows that this increased absorption leads to an increased implosion velocity and a factor-of-3 increase in the 1-D predicted neutron yield.

For these simulations (square symbols), the ZPP profiles are given by

$$I_i = P \frac{\exp\left[-\left(r/r_i\right)^{m_i}\right]}{\int \exp\left[-\left(r/r_i\right)^{m_i}\right] r dr},$$

where P is the laser power, i indicates the parameter during the pickets ($i = p$) or main drive ($i = d$), $m_p = 4$, $r_p = 353 \mu\text{m}$ (corresponding to $R_b/R_t = 1$, where R_b is the 95% encircled-energy radius), $m_d = 4$, and r_d was varied from $182 \mu\text{m}$ ($R_b/R_t = 0.5$) to $353 \mu\text{m}$ ($R_b/R_t = 1$).

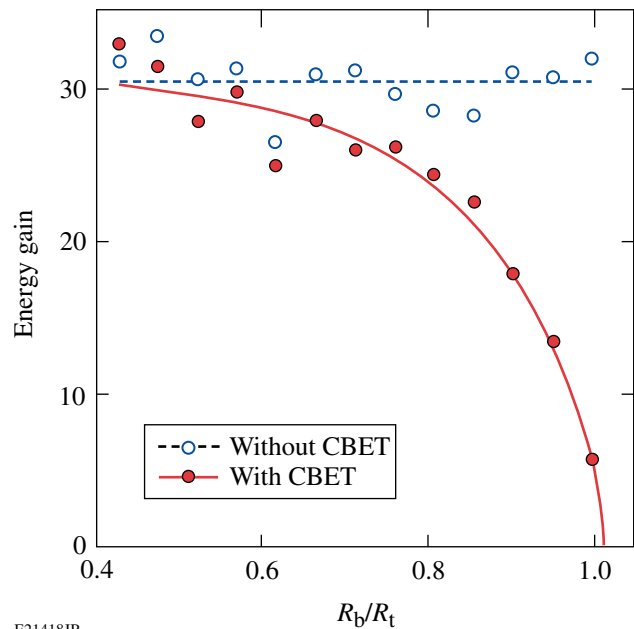
For the 1.5-MJ symmetric direct-drive-ignition design,⁶ zooming can recover a significant portion of the ablation pressure lost to CBET.¹⁹ Figure 133.44 shows that reducing the diameter of the laser beams by 30% is sufficient to recover 90% of the calculated 1-D gain when simulated without including CBET. For a fixed ignition margin ($E_{KE}/E_{\min} \propto \text{IFAR}^3 P_a^3$,



E21417JR

Figure 133.43

The calculated (a) implosion velocity and (b) 1-D yield are plotted as functions of the normalized laser-beam radius for the main drive pulse for two typical low-adiabat OMEGA cryogenic conditions. Low-mass targets ($10 \mu\text{m}$ of CD + $44\text{-}\mu\text{m}$ -thick DT shells) (blue) and higher-mass targets ($9.5 \mu\text{m}$ of CD + $66\text{-}\mu\text{m}$ -thick DT shells) (red) corresponding to OMEGA shots 66612 and 55722, respectively, with optimal zooming profiles (squares) are shown. The predictions using the proposed OMEGA zooming scheme (triangles) are shown. The total energy on target was $\sim 25 \text{ kJ}$, corresponding to an overlap intensity $I_{\text{ovr}} = 8.8 \times 10^{14} \text{ W/cm}^2$.



E21418JR

Figure 133.44

The 1-D gain is calculated for a series of symmetric simulations where the ratio of the laser-beam radius to the target radius ($R_t = 1.7 \text{ mm}$) is varied. The design parameters are taken from Ref. 6.

where IFAR is a measure of the target stability), this increased ablation pressure increases the stability of the implosions ($\text{IFAR} \propto 1/P_a$), providing a more-robust design.

Implications of Zooming on Direct-Drive Implosions

The following section presents the proposed zooming scheme, defines the zooming laser-spot profiles (consistent with OMEGA capabilities), and addresses both the hydrodynamic efficiency (1-D physics) and the hydrodynamic stability (2-D physics) of the OMEGA cryogenic direct-drive target design. Specifically, the hydrodynamic efficiency is increased by the reduced diameter of the laser beams (i.e., reduced CBET) and the increased energy in the normal rays (i.e., energy deposition closer to the ablation surface). The hydrodynamic efficiency may be reduced if the increased single-beam laser intensity exceeds the backscatter thresholds. The hydrodynamic stability is potentially affected by the reduced diameter of the laser beams during the main drive (low mode) and the reduced power spectrum during the pickets (high-frequency imprint).

1. Proposed Focal-Zooming Scheme

a. Time-dependent near field. The basic construct for the time-dependent near-field profile involves a sub-aperture beam for the initial pickets with a full-size beam for the main pulse. The area of each beam depends on three considerations: beam intensity to prevent laser damage, controlled power spectrum to obtain irradiation uniformity, and the stored energy in the beamline.

Based on the maximum required picket power (~ 0.12 TW/beam) and the currently allowed intensity, the minimum sub-aperture beam diameter during the pickets is 14 cm. This sub-aperture beam is half of the nominal diameter and would limit the total energy on target to 75% of the maximum OMEGA energy if an annular main drive pulse were used. The proposed OMEGA zooming scheme will implement a full-aperture beam during the main drive [Fig. 133.40(b)].

b. Zooming phase plates. The proposed zooming approach is made possible by designing a ZPP containing a central region that produces a larger focal spot, while its outer annular region produces a smaller, high-order focal spot. During the picket pulses, a small-diameter beam propagates through the center region of the ZPP, producing a large focal spot. This configuration produces a small central focal spot on top of a lower-intensity larger profile defined by the center of the ZPP. The design methodology for this ZPP involves using a deeper surface relief in the central region, with a smaller one in the annular region of the phase plate. A slowly varying, continu-

ous surface relief is required to reduce the near-field irradiance modulation imposed on the optics at the end of the laser.

The laser profiles consistent with the OMEGA capabilities (“OMEGA ZPP”) are shown in Fig. 133.45. The laser profiles during the pickets are defined by the central 14-cm diameter of the ZPP. Their intensity profiles are given by

$$I_p = P \frac{\exp\left[-\left(r/r_p\right)^{m_p}\right]}{\int \exp\left[-\left(r/r_p\right)^{m_p}\right] r dr},$$

where $m_p = 4$ and $r_p = 365 \mu\text{m}$ (corresponding to a 95% encircled energy radius $R_b = 430 \mu\text{m}$).

After the third picket, the OMEGA beams will use the full aperture (28-cm diameter). The outer ring of the ZPP will produce a high-order super-Gaussian profile. The profile during the drive will consist of the sum of the two profiles, where 3/4 of the total laser power will be within the higher-order profile and 1/4 in the lower-order profile,

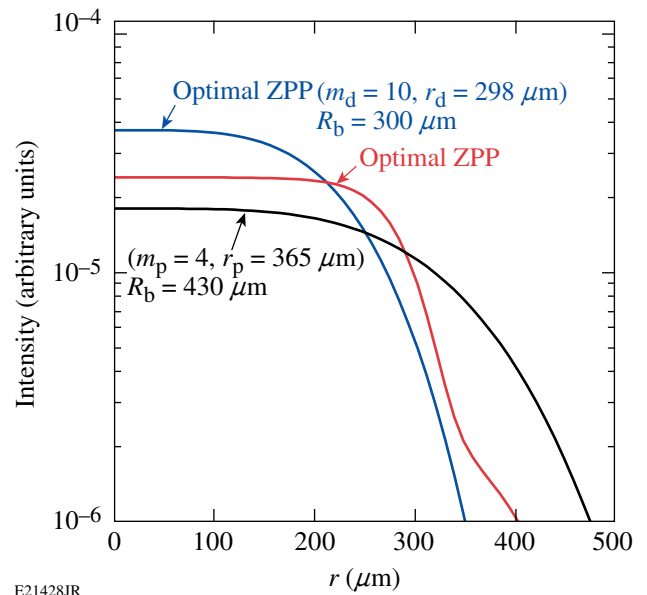


Figure 133.45

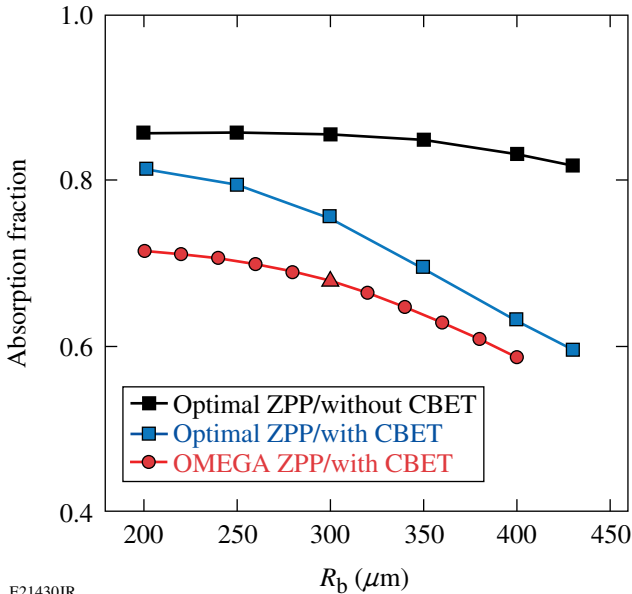
The proposed OMEGA ZPP profiles of the laser beams during the pickets (black curve) and during the main drive (red curve). The more-optimal ZPP profile $R_b/R_t = 0.7$ (blue curve) is shown for $R_b = 300 \mu\text{m}$. The profiles are normalized to the laser power.

$$I_d = P \left\{ \frac{1}{4} \frac{\exp[-(r/r_p)^{m_p}]}{\int \exp[-(r/r_p)^{m_p}] r dr} + \frac{3}{4} \frac{\exp[-(r/r_d)^{m_d}]}{\int \exp[-(r/r_d)^{m_d}] r dr} \right\},$$

where $m_d = 10$ and $r_d = 298 \mu\text{m}$ (corresponding to a 95% encircled energy radius of $R_b = 300 \mu\text{m}$). The lower-order profile is determined by the picket profile but is slightly modified as a result of turning SSD off (not included in this analysis). With the current rectangular SSD kernel ($1.5 \text{ \AA} \times 3.0 \text{ \AA}$), the laser spots during the drive will be slightly elliptical unless compensated for by the ZPP. The ZPP's will be designed to account for the slight ellipticity introduced by the distributed polarization rotators (see Appendix A.1).

2. Hydrodynamic Efficiency (1-D Physics)

a. Cross-beam energy transfer. Figure 133.46 shows results from hydrodynamic simulations with (blue squares) and without CBET (black squares). For the nominal laser beam radii ($R_b/R_t = 1$), CBET reduces the absorption from 82% to 60%. Using the more-optimal ZPP profiles and reducing their radii to $R_b = 300 \mu\text{m}$ ($R_b/R_t = 0.7$), the system recovers more than



E21430JR

Figure 133.46

A comparison of the absorption calculated when including CBET for the zooming configurations with the more-optimal ZPP (squares) and the OMEGA ZPP scheme (circles). The proposed OMEGA zooming profile is shown (triangle). For comparison, simulations without CBET using the more-optimal ZPP scheme are shown (black squares). The overlapped intensity is $8 \times 10^{14} \text{ W/cm}^2$ in all simulations. Shot parameters correspond to OMEGA shot 55722.

70% of the absorbed energy lost to CBET. This is compared with hydrodynamic simulations that use the proposed OMEGA ZPP profiles. For the OMEGA ZPP profile (triangle), CBET is reduced and recovers 35% of the absorbed energy lost to CBET. The residual wings in the laser-beam profiles during the drive (Fig. 133.45) limit the ability of zooming to completely mitigate CBET. The OMEGA ZPP configuration increases the velocity of the thick-target design ($9.5 \mu\text{m}$ of CD + $66 \mu\text{m}$ of DT) from $2.8 \times 10^7 \text{ cm/s}$ ($R_b/R_t = 1$) to $3.2 \times 10^7 \text{ cm/s}$ and the corresponding 1-D predicted neutron yield increases from 3.4×10^{13} to 7.8×10^{13} (Fig. 133.43). For a less-massive target ($10 \mu\text{m}$ of CD + a $44\text{-}\mu\text{m}$ -thick DT shell), the velocity for $R_b/R_t = 0.7$ is $4.1 \times 10^7 \text{ cm/s}$ when using the more-optimal beam profiles during the drive, compared to an estimated $3.7 \times 10^7 \text{ cm/s}$ when using the OMEGA ZPP profiles.

b. Laser-plasma interactions. Reducing the radii of the beams during the drive increases the single-beam laser intensity. In typical cryogenic designs on OMEGA, where $R_b/R_t = 1$, the peak single-beam intensity is approximately

$$I_p(r=0) \cong \frac{8}{N} I_{\text{ovr}} \sim 1.2 \times 10^{14} \text{ W/cm}^2,$$

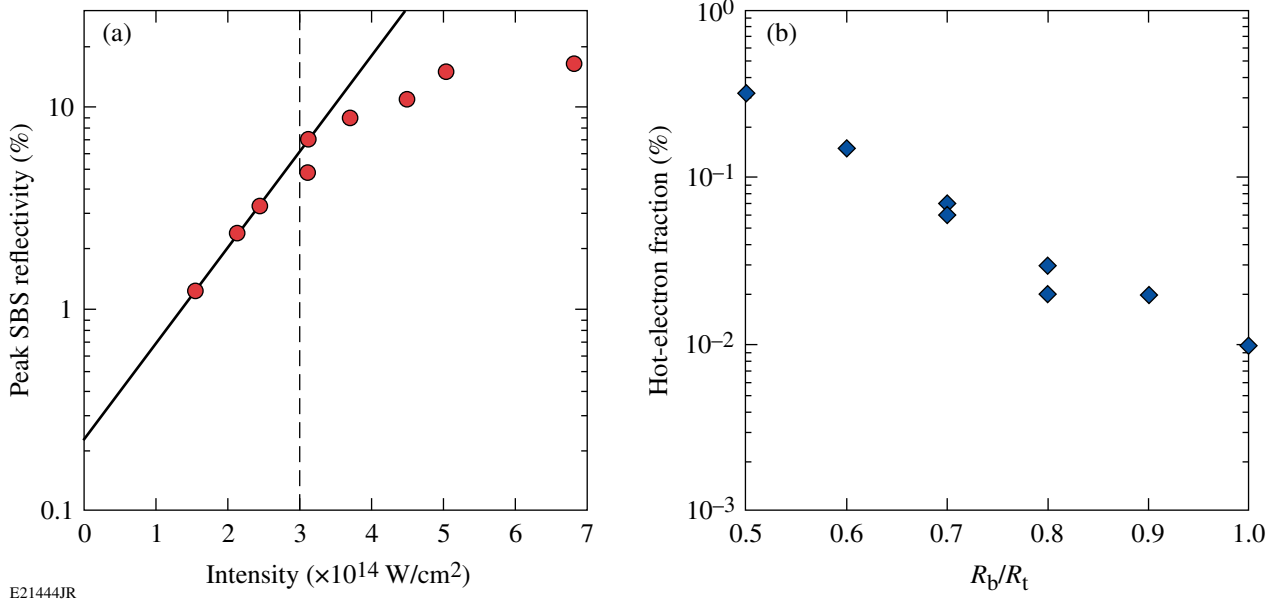
where $N = 60$ is the number of beams, $I_{\text{ovr}} = P_d/A_t = 8.8 \times 10^{14} \text{ W/cm}^2$, $P_d = 20 \text{ TW}$ is the power in the drive, and A_t is the surface area of the target. The single-beam intensity is increased as the radii of the beams are reduced:

$$I_d(r=0) \cong 1.2 \times 10^{14} \left(\frac{R_t}{R_b} \right)^2 \text{ W/cm}^2.$$

For $R_b = 300 \mu\text{m}$, the corresponding single-beam intensity during the drive is $\sim 2.5 \times 10^{14} \text{ W/cm}^2$.

Figure 133.47(a) shows the measured peak SBS reflectivity threshold for OMEGA direct-drive plasmas. Exceeding the SBS intensity thresholds will backscatter laser light from the target, reducing the drive efficiency. These results suggest that the peak laser intensities must remain below $3 \times 10^{14} \text{ W/cm}^2$ to keep SBS from becoming energetically significant, but this threshold depends on the exact plasma conditions.

Experiments on OMEGA show an increase in the hot-electron fraction when reducing the radii of the laser beams (see Ref. 18 for the experimental setup). Figure 133.47(b) shows that the fraction of laser energy converted to hot electrons increased by more than an order of magnitude when the radii of the laser beams were changed from $430 \mu\text{m}$ to $215 \mu\text{m}$.



E21444JR

Figure 133.47

(a) The peak SBS reflectivity measured from OMEGA 860- μ m-diam CH implosion experiments is shown as a function of the peak single-beam laser intensity. The SBS reflectivity peaks during the intensity rise in the main drive pulse when the electron temperature is low. (b) The fraction of laser energy converted to hot electrons inferred from hard x-ray measurements is shown as a function of the radii of the laser beams normalized to the target radius ($R_t = 430 \mu\text{m}$). The overlapped intensity was held nearly constant at 4.5×10^{14} W/cm².

3. Hydrodynamic Stability (2-D Physics)

a. Low-mode stability. Two-dimensional *DRACO*²⁷ simulations were performed to investigate the level of perturbations induced by the lower illumination uniformity when the diameter of the laser beams were reduced at various times in the laser pulse. The simulations use a cryogenic, low-adiabat, triple-picket implosion design (OMEGA shot 55722, 9.5 μm of CD + a 66- μm -thick DT shell). The simulations that do not include CBET employ a thermal-transport model where the heat flux was limited to a fraction ($f = 0.06$) of the free-streaming flux.²⁸ This is a reasonable approach since 1-D simulations indicate very little effect from CBET for these conditions (i.e., $R_b/R_t = 0.7$).

Figure 133.48 shows simulated shell densities at maximum compression. Improvements in target uniformity are clearly seen in Fig. 133.48(b), where two-state zooming was applied after the third picket in comparison with those simulations where zooming was not used [Fig. 133.48(a)]. Table 133.VII summarizes the performance of simulated targets depending on the transition time from large- to small-diameter beams. At peak neutron flux, the normalized areal-density perturbations (Σ_{rms}) are shown and quantify the effect of the overlapped nonuniformities. These results indicate that the amplitude of perturbations is reduced by an order of magnitude when the

Table 133.VII: A summary of the effect of zooming on areal-density perturbations at peak neutron flux when zooming at different times from $R_b/R_t = 1.0$ to $R_b/R_t = 0.7$.

Zooming	R_b/R_t	Σ_{rms} (%)
Not applied	0.7	9
After first picket	1.0 to 0.7	7
After second picket	1.0 to 0.7	1.1
After third picket	1.0 to 0.7	1.1
At beginning of main pulse	1.0 to 0.7	1.1
Not applied	1.0	1.2

transition occurs after the second or third picket and that zooming between the third picket and the main pulse will maintain target uniformity while mitigating CBET.

b. High-frequency imprint. The proposed OMEGA zooming scheme requires that the near-field diameter be reduced by a factor of 2 to produce larger laser spots during the pickets. This reduced near-field diameter may impact the target performance by increasing the rms (root-mean-square) illumination nonuniformity. Figure 133.49 shows the ratio of the ℓ -mode σ_{rms} amplitude spectrum for the OMEGA ZPP design during the pickets ($D_{\text{ZPP}} = 14$ cm) to the standard OMEGA configuration ($D = 28$ cm). The ℓ -mode σ_{rms} is given by²⁹

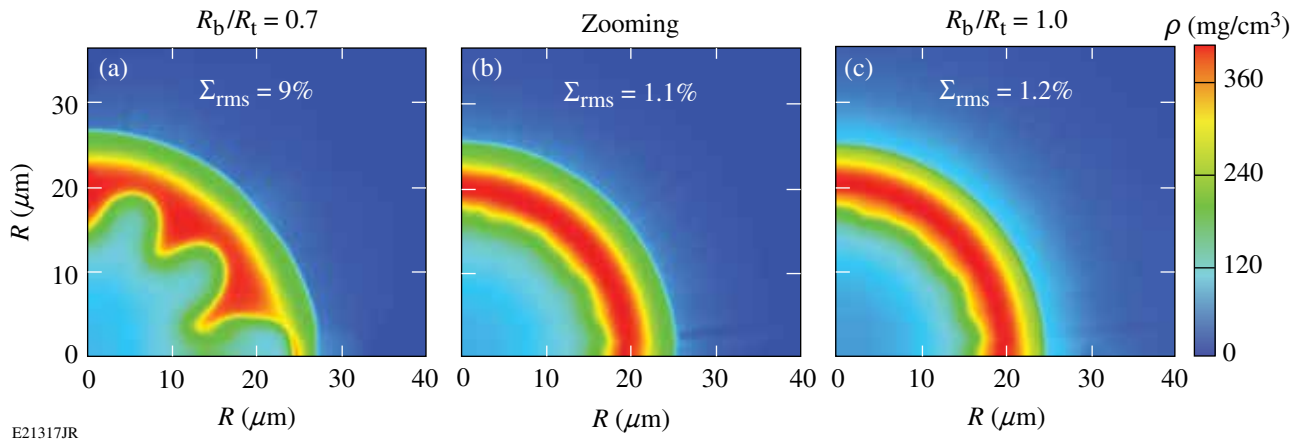


Figure 133.48

Simulated shell density at maximum compression in the case of using (a) small-diameter beams ($R_b/R_t = 0.7$) for the entire laser pulse, (b) large-diameter beams ($R_b/R_t = 1$) for pickets and small-diameter beams ($R_b/R_t = 0.7$) for the main pulse, and (c) large-diameter beams for the entire pulse.

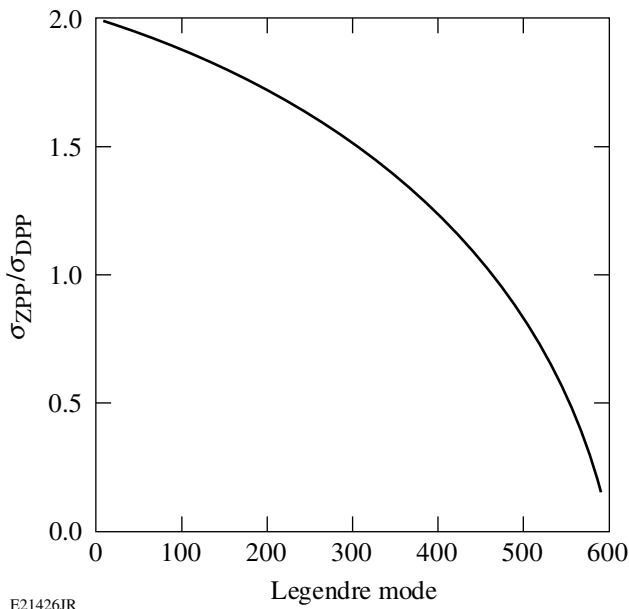


Figure 133.49

The ratio of rms (root-mean-square) illumination uniformity for the sub-aperture pickets (half-aperture) over the standard OMEGA full-aperture configuration is plotted against the Legendre mode for a target radius of 430 μm .

$$\sigma_l^2 = \frac{16}{\pi \ell_{\max}} \frac{\ell}{\ell_{\max}} \times \left[\cos^{-1} \left(\frac{\ell}{\ell_{\max}} \right) - \left(\frac{\ell}{\ell_{\max}} \right) \sqrt{1 - \left(\frac{\ell}{\ell_{\max}} \right)^2} \right],$$

where $\ell_{\max} = Rk_{\max} = 2\pi R/F\#\lambda$, $R = 460 \mu\text{m}$ is the target radius, $F\# = FL/D$, $FL = 190 \text{ cm}$, and D is the diameter of the beam at the lens plane.

Over the range of modes that most significantly impacts target performance (10 to 300), σ_{rms} increases by a factor of nearly 2. In addition, the $4\times$ reduction in beam area will result in fewer speckles to fill out the envelope and the focal spot will contain a lumpy pattern. An assessment of the impact of increased illumination uniformities will be performed but mitigation strategies have been demonstrated that reduce imprint by a factor of 2 when using doped ablaters.^{22,23} Although a larger beam size during the pickets would fill out the power spectrum, the correspondingly larger central region of the ZPP would increase the energy in the tails of the beam profiles during the drive and would increase CBET.

Propagation of a beam with a half diameter through the current SSD system will produce 1.5 color cycles over the beam rather than the current three color cycles. Although the angular dispersion remains constant, the simultaneity of the colors in the spectrum is not guaranteed and a certain amount of modulation frequency may appear in the integrated focal spot on target, i.e., unwanted pulse shaping. If this is found to be a problem for the experiment, the SSD system will need to be modified.

4. Target Physics Requirements for Zooming on OMEGA

The physics requirements for zooming are based on demonstrating implosion performance on OMEGA that is hydrodynamically equivalent to a 1.5-MJ ignition implosion on the National Ignition Facility (NIF). This requires a Lawson criteria³⁰ $\left[\chi \approx (\rho R)^{0.6} (0.24 Y_n / M_{\text{fuel}})^{0.3} \right]$ of $\chi = 0.16$, where ρR is in g/cm^2 , Y_n is the yield in units of 10^{16} , and M_{fuel} is the mass of the fuel in milligrams (mg) (Ref. 31). For the total laser energy available on OMEGA, this corresponds to a ρR of

300 mg/cm² and a yield of 4×10^{13} . Currently, the best implosions on OMEGA produce a yield of 2.1×10^{13} and a ρR of 160 mg/cm² corresponding to $\chi = 0.09$ (Ref. 32). Mitigation of CBET will increase the ablation pressure, providing both a higher ρR ($\rho R \propto \sqrt{P_a}$) and a higher yield ($Y \propto P_a$). The physics requirements for zooming on OMEGA are based on increasing the ablation pressure by reducing CBET without imposing deleterious effects through nonuniformities or laser–plasma interactions. The following section provides the physics basis for the OMEGA zooming design and presents the main logic used to determine the requirements summarized in Table 133.VIII.

Table 133.VIII: Target physics requirements for zooming on OMEGA.

	R_b (μm)	Power spectrum	SG order	Peak power (TW/beam)
Pickets	430	See below*	4	0.12
Drive	365**	Best effort	2 to 20	0.35

*See **Power Spectrum (Pickets)** below.

See **Drive-Beam Radius below.

a. Picket-beam radius. The radii of the laser beams during the pickets are defined to maximize illumination uniformity and minimize the energy lost outside of the target. The proposed design assumes that the current SG4 distributed phase plate (DPP) profiles are optimized ($m = 4$, $r = 365 \mu\text{m}$). A further optimization study could be performed to characterize the effect of reducing the picket-beam radius on the illumination nonuniformities and the CBET during the drive; reducing the beam radius during the pickets will reduce the wings in the drive profile.

b. Drive-beam radius. The minimum drive-beam radius is governed by the acceptable low-frequency modulations and the acceptable laser–plasma interaction intensity thresholds. The maximum drive-beam radius is governed by the required reduction in CBET to regain hydrodynamically equivalent implosions on OMEGA. A minimum radius of $R_b = 300 \mu\text{m}$ is proposed to ensure that the peak intensity remains below the intensity, where SBS scatters <5% of the incident laser light.

c. Power spectrum (pickets). The power spectrum between Legendre modes 10 and 300 has the largest impact on target performance. A study will be performed to assess the impact of the increased power spectrum over these modes, but mitigation strategies exist that can reduce the imprint by a factor of 2 (Refs. 22 and 23).

d. Super-Gaussian order (pickets). To maintain reasonable illumination uniformities during the pickets, a super-Gaussian order consistent with the current OMEGA SG4 design ($m = 4$) is proposed.^{33,34} With the OMEGA near-field limitations during the drive, increasing the super-Gaussian order may reduce CBET; a further study will be performed to optimize this gain with the loss of illumination uniformity.

e. Super-Gaussian order (drive). A series of 1-D LILAC simulations were performed to investigate the sensitivity of CBET to the super-Gaussian order of the laser beams during the main drive. In these simulations the profile of the laser beams during the pickets was given by a fourth-order super-Gaussian with 95% of the energy contained within the target diameter ($2R_t = 860 \mu\text{m}$), and the super-Gaussian order during the main drive was varied between 2 and 20 [Fig. 133.50(a)] while maintaining 95% of the energy within $R_b = 300 \mu\text{m}$. Figure 133.50(b) shows a small effect on the laser-beam absorption. For a given laser power and spot size, high-order super-Gaussian beam profiles reduce the peak intensities limiting the risk of laser–plasma instabilities.

f. Peak power (pickets). The picket-pulse shapes (timing and peak powers) are used to set the adiabat, and it is not currently envisioned that the peak power in the pickets will exceed 0.12 TW. This peak power must be consistent with the diameter of the laser beams during the pickets to ensure the laser system remains below damage thresholds.

g. Peak power (drive). The current cryogenic target design uses 25 kJ of energy to produce a peak power of nearly 0.35 TW in the drive.

5. Proposed Physics Studies

Several physics issues are identified that require further study:

1. The fraction of laser energy converted to hot electrons will be measured and their impact on target performance assessed for laser beams with $R_b = 300 \mu\text{m}$, producing an overlapped intensity of $8 \times 10^{14} \text{ W/cm}^2$ on a standard 430- μm -radius target.
2. The impact of the increased power spectrum during the pickets on the OMEGA implosion performance will be studied and mitigation strategies developed to reduce the effects of imprint.
3. A study is required to optimize the picket-beam profiles. Because the drive pulse shares the central portion of the ZPP with the pickets, the picket profile defines the wings during the main pulse. Reducing the beam radius or increasing the super-Gaussian order during the pickets will further reduce CBET but may increase laser imprint.

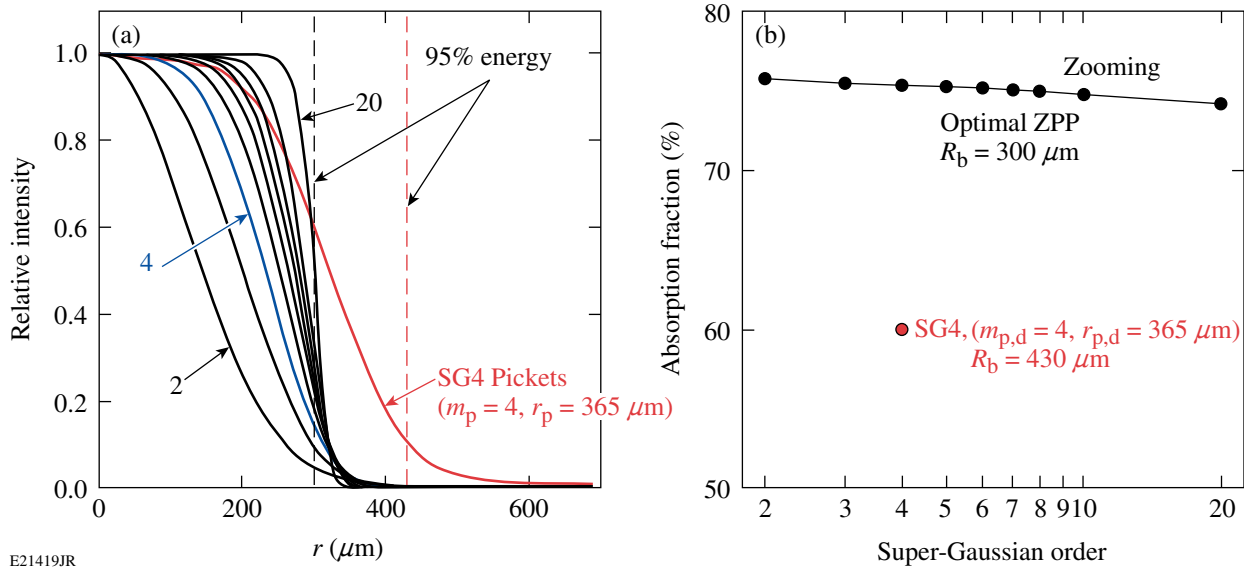


Figure 133.50

The profiles used in simulations to investigate the sensitivity of CBET to super-Gaussian order during the main drive. (a) The profiles in the main drive were varied by changing the super-Gaussian order between 2 and 20 while maintaining 95% of the energy within $R_b = 300 \mu\text{m}$. (b) The effect of super-Gaussian order over this range has a small effect on total absorption.

- The $4\times$ reduction in the area of the laser beam during the pickets will result in fewer speckles to fill out the envelope and the focal spot could contain lumps. This effect on target performance will be assessed by simulating the implosion performance using the calculated ZPP phase.

Implementation of Zooming on OMEGA

The proposed implementation of zooming on OMEGA requires a dynamic two-state near-field profile and a set of ZPP's. To generate the required two-state near-field profile, a dual-driver co-propagation configuration is proposed. The driver that will generate the pickets will contain the current rectangular SSD kernel and pass through an apodizer, forming a beam of half the standard diameter. A second driver will generate the drive pulse and propagate without SSD through its own apodizer, forming a full-diameter beam.

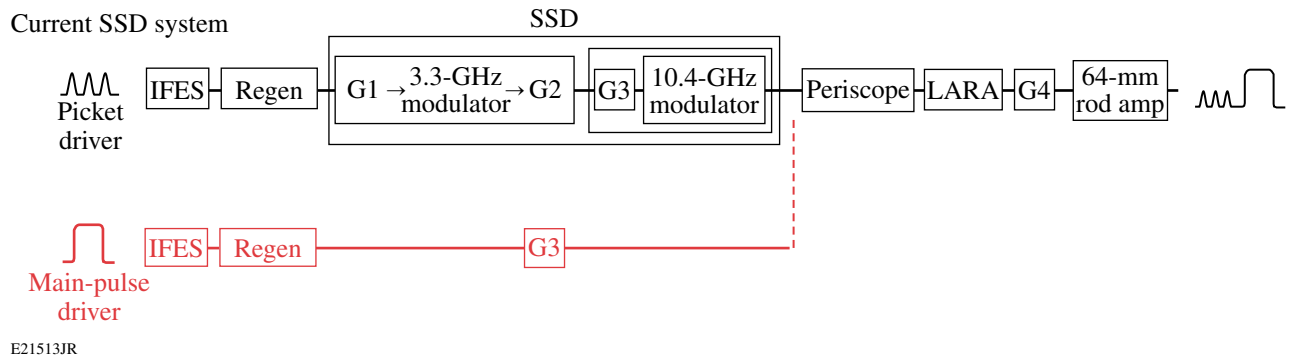
Implementation of focal-spot zooming on OMEGA will require the development of a new main-pulse driver (zooming driver) that can be combined and co-propagated with the current SSD driver after the SSD modulators (Fig. 133.51). By combining the drivers at the base of the periscope, the losses introduced by the combining optic can be offset by rebalancing the engineered losses that currently exist at the output of the regenerative amplifier. The driver combination would be located before the G4 grating(s). To compensate for the G4

grating(s), a G3 surrogate grating would be integrated into the zooming driver line to apply the required spatiotemporal shear to precompensate for the G4 grating.

An initial study of implementing zooming on OMEGA indicates no technical limitations. Introducing a dual-driver co-propagation configuration will provide (1) a 14-cm-diam beam during the pickets ($1.5\text{-}\text{\AA} \times 3\text{-}\text{\AA}$ SSD) and a full-aperture, 28-cm-diam beam (no SSD) during the main drive; and (2) an $\sim 10\%$ increase in on-target energy as a result of better frequency-conversion efficiency.

Summary

To demonstrate hydrodynamic-equivalent ignition performance on OMEGA, CBET must be mitigated. For a nominal direct-drive configuration, CBET scatters $\sim 20\%$ of the laser energy from the target, reducing the ablation pressure by 40%. This reduced ablation pressure impacts the direct-drive implosions by reducing the hot-spot pressure and the implosion velocity. This results in a lower yield and reduced stability of the implosion when maintaining a constant minimum energy. On OMEGA cryogenic implosions, the reduced ablation pressure results in an order-of-magnitude reduction in yield. Reducing the radii of the laser beams during the main drive, while maintaining the nominal radius of the laser beams during the pickets (two-state zooming),¹⁹ is shown to significantly reduce



E21513JR

Figure 133.51

The current smoothing by spectral dispersion (SSD) driver line (black) and the proposed zooming drive line (red) are shown. IFES: integrated front-end source; Regen: regenerative amplifier; LARA: large-aperture ring amplifier.

CBET while maintaining high-quality implosions. A two-state zooming scheme is proposed for OMEGA that will recover 35% of the energy lost to CBET.

Implementing zooming on OMEGA will require a new set of phase plates and a dynamic near-field profile. The proposed dynamic near-field profile can be produced using a co-propagating dual-driver configuration. The initial driver line would produce the pickets and propagate through the central half-diameter of the laser system, while the second driver would produce the drive pulse and propagate through the full aperture of the laser system. The central 14-cm diameter of the radially varying phase plates would produce the nominal laser profile on target during the pickets and a smaller radius profile during the main drive.

Implementing zooming on OMEGA will provide a higher hydrodynamic efficiency that will allow targets to be driven faster with higher stability and is equivalent to an increased velocity corresponding to a 30% increase in the on-target laser energy.

ACKNOWLEDGMENT

This work was supported by the U.S. Department of Energy Office of Inertial Confinement Fusion under Cooperative Agreement No. DE-FC52-08NA28302, the University of Rochester, and the New York State Energy Research and Development Authority. The support of DOE does not constitute an endorsement by DOE of the views expressed in this article.

Appendix A: Alternate Concepts for Zooming on OMEGA

Additional focal-zooming schemes are available for consideration. The zooming effect from 2-D SSD is proportional to the bandwidth, the grating dispersion, and the focal length of the final lens. Increasing either the bandwidth or the grating dispersion on OMEGA would necessarily require opening

the spatial-filter apertures. Placing the final dispersion grating closer to the end of each beamline would allow greater angular dispersion without the risk of damaging the laser chain. Alternatively, the focal length of the final lens could be increased to achieve larger deflection at the focal plane. In this case the focal lens assemblies would be positioned within the hex tubes and the vacuum windows would be repositioned outside the surface of the target chamber rather than being re-entrant. Another option involves using a circular grating at the end of the system to provide both beam smoothing and focal-plane broadening.

1. Zooming with Enhanced 2-D SSD Reduction

An alternative approach to zooming that takes advantage of the reduced deflection that occurs when SSD is turned off was investigated. This approach could achieve the optimum reduction of CBET (i.e., no wings in the profiles during the main drive) but requires that the SSD deflection be symmetric and significantly increased to achieve a change in the focal-spot radius of $65 \mu\text{m}$ (from $430 \mu\text{m}$ to $365 \mu\text{m}$ for equivalent ZPP scheme performance). This initial study indicates that the small SSD dimension could be doubled to form a symmetric 2-D SSD kernel that would produce an $\sim 35\text{-}\mu\text{m}$ change in the focal-spot radius, but it is unlikely that a further increase to accommodate the required deflection is feasible.

Currently, laser-beam smoothing on the OMEGA 60-beam system includes 2-D SSD and distributed polarization rotation (DPR). The 2-D angular deflection kernel is square and consists of SSD deflection in the first dimension with a 50/50 combination of SSD and DPR deflections in the second dimension. The magnitude of angular deflection from SSD is the product of the angular dispersion and the bandwidth. The angular deflection from the DPR is set by the wedge in the birefringent plate. The

resulting spatial shift in the focal plane is the product of the total angular deflection and the focal length of the lens.

To fully benefit from SSD broadening in two dimensions, the wedged DPR is removed, while the second dimension of SSD is doubled in magnitude. This could be achieved by either doubling the bandwidth or doubling the angular dispersion, or an optimized combination of both. The resulting focal spots would be nominally round either with or without 2-D SSD. Downward zooming would be achieved by turning off the bandwidth, and, therefore, the deflection kernel, in such a way that a smaller monochromatic focal spot would irradiate the target. In this scenario, a 2-D symmetric SSD kernel would be turned off after the pickets and before the main pulse.

a. Ability for OMEGA to support a symmetric 2-D SSD kernel. Removing the current DPR's and making the resultant rectangular far-field kernel square by increasing the deflection Γ in the narrow dimension were investigated to determine if a symmetric SSD kernel could be supported by the OMEGA system. Since the far-field deflection is the product of the frequency dispersion ($\partial\theta/\partial\lambda$) and the total bandwidth $\Delta\lambda$, the deflection may be increased by increasing either the dispersion or the total bandwidth.

Prior to addressing changes to OMEGA that are required to support the symmetric kernel, the current state of SSD on OMEGA was assessed. The current implementation of three-color-cycle SSD consists of 1.5 Å of FM bandwidth at 3.3 GHz dispersed in the phase-matching direction of the frequency doubler and 3.0 Å of FM bandwidth at 10.4 GHz dispersed in the phase-matching direction of the tripler. The dispersion, measured at the 30-cm output aperture of OMEGA, is $32 \mu\text{rad}/\text{Å}$ in both directions. In the absence of any aberrations, this results in a rectangular far field with a 2:1 aspect ratio [Fig. 133.52(a)]. The actual far-field pattern is a convolution of the theoretical rectangle with the aberrated, undispersed focal spot.

Figure 133.52(b) shows an estimated OMEGA IR far-field spot along with the limiting pinhole aperture in the OMEGA Laser System. Plasma blowoff from laser intensity on the pinhole edges ultimately limits how much dispersed bandwidth can be propagated through OMEGA. This is a statistical function of the deflection, temporal pulse shape, beamline aberration, pulse length, alignment tolerances, and pinhole geometry and cleanliness.

To assess OMEGA's ability to support a symmetric SSD kernel, the required system changes, implications for the

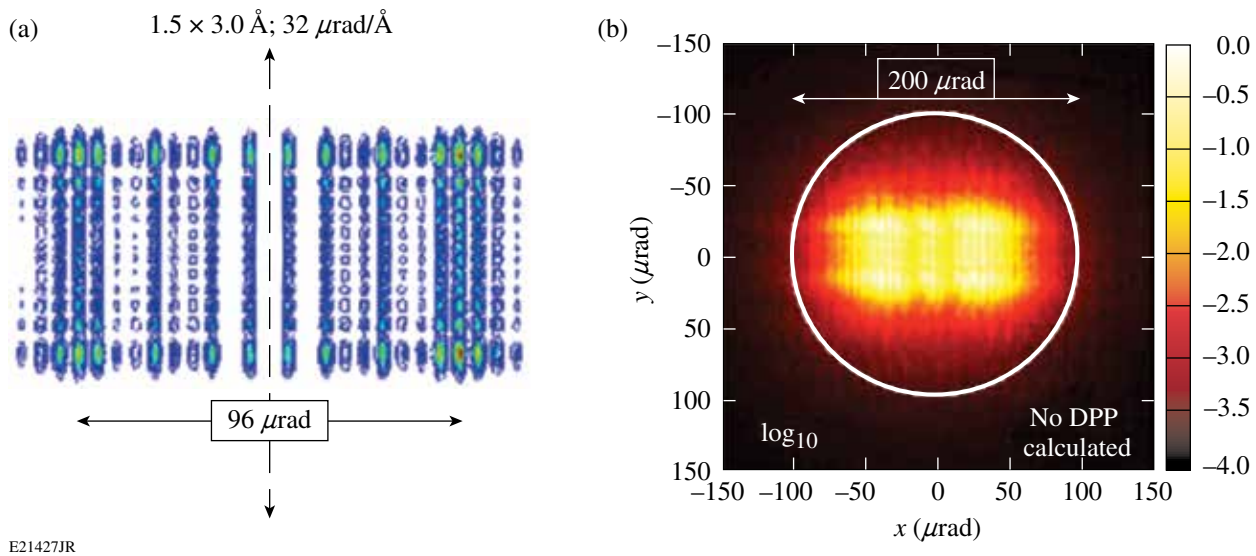


Figure 133.52

(a) The theoretically perfect rectangular far-field pattern. Note the Bessel-function structure in either direction. The narrow (vertical in figure) dimension is the 1.5-Å bandwidth, 3.3-GHz direction; the wide (horizontal in figure) dimension is the 3.0-Å bandwidth, 10.4-GHz direction. (b) Simulated IR \log_{10} far-field spot ($4\times$ diffraction limit) at the 30-cm aperture. The white circle is the aperture of the limiting pinhole calculated at the end of the laser system.

OMEGA pinholes as a result of the focal-spot shape change, and the impact on the frequency-conversion efficiency and potential FM-to-AM effects of the increase in bandwidth and/or dispersion are investigated.

System changes: Achieving a symmetric focal spot requires increasing the far-field deflection of the 3.3-GHz axis. This can be achieved by increasing the bandwidth at 3.3 GHz or increasing the dispersion. Further increases in bandwidth would require testing of the 3.3-GHz modulator, which is currently near its power limit. It is possible that some increase in bandwidth can be realized, but this remains to be experimentally demonstrated. Increasing the dispersion in the 3.3-GHz direction requires that a single grating in the pulse-generation room be replaced with a new grating. The actual implementation of a new grating geometry would require substantial realignment of the 3.3-GHz SSD arm.

Pinhole implications: In the early days of three-color-cycle SSD on OMEGA, it became clear that the current pinhole configuration cannot tolerate any increase in the far-field deflection in the 10.4-GHz direction (wide direction). Any increase in the current OMEGA pinhole size is prohibited by the observed damage rate to the Stage-D, -E, and -F input spatial-filter lenses and the necessity of preventing catastrophic retroreflections in the beamlines. It is possible that the current pinholes could tolerate an increase in the far-field deflection in the narrow 3.3-GHz direction.

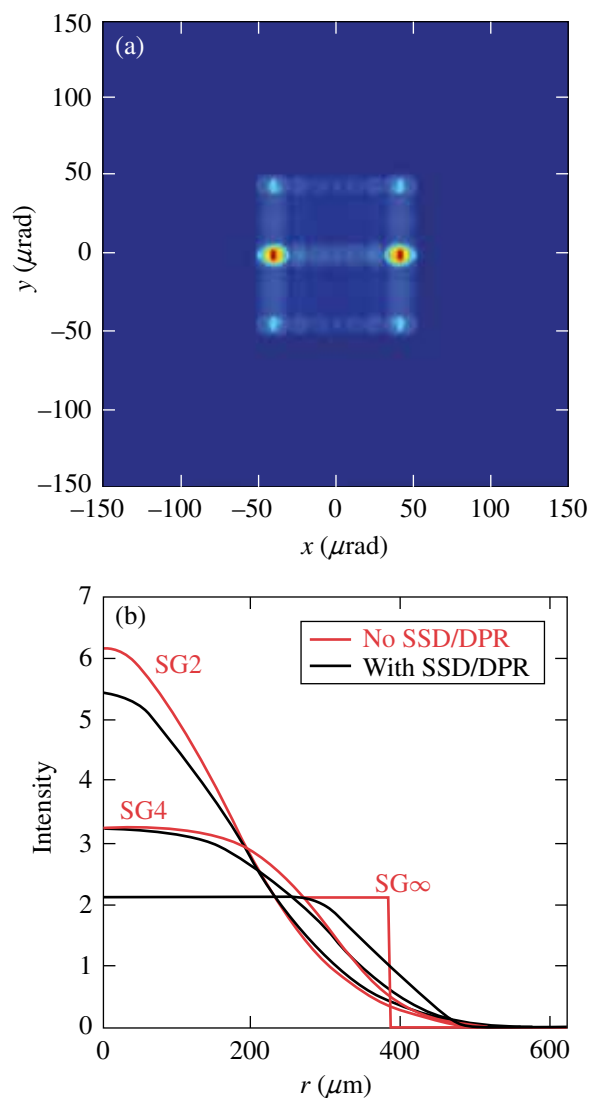
Several factors contribute to the position and size of the focal spot relative to the pinhole. These factors are statistical in nature, so while theoretical calculations can provide an estimate of the amount of deflection in the narrow direction that can be realized, the actual capability of OMEGA to support this change can be measured only via a series of laser shots. This experimental investigation will require a dedicated laser campaign that increases relative deflection while monitoring the transmitted near-field profile, transmitted temporal pulse shape, retroreflected energy, and pinhole-scattered light.

Frequency conversion: A deflection increase in the narrow 3.3-GHz direction has the potential to limit conversion efficiency and introduce FM-to-AM conversion because of the poor conversion efficiency of certain components of the FM spectrum. This loss of frequency conversion can occur regardless of which technique (increased dispersion or increased bandwidth) is used to increase deflection. Both options have been examined with respect to frequency-conversion implica-

tions using the code Miró,³⁵ and preliminary results indicate no preferred method from this standpoint. Implementation difficulty will most probably dictate the choice of technique.

b. Effects of the current OMEGA kernel on the focal spot.

To estimate the effect of 2-D dynamic bandwidth reduction, the best understanding of the current OMEGA SSD/DPR deflection kernel [Fig. 133.53(a)] was used. Figure 133.53(b) shows



E21421JR

Figure 133.53
 (a) The current OMEGA far-field SSD/DPR convolution kernel applied to a diffraction-limited ($\sim 12 \mu\text{m}$ at the target plane) beam (smoothed for presentation purposes). (b) The beam profiles when the current SSD/DPR kernel is applied (black) to the “no SSD/DPR” (red) profiles generated with super-Gaussian orders of 2, 4, and infinity. All beams have a “with SSD/DPR” diameter of $860 \mu\text{m}$.

the effect of this kernel on various laser-beam far-field profiles. Table 133.IX summarizes these results with respect to zooming; the maximum effect occurs for an infinitely steep profile where the 95% encircled-energy radius is increased from 377 μm to 430 μm . To achieve the proposed zooming conditions (430 μm to 300 μm), where 70% of the energy lost to CBET is recovered, the kernel would need to be increased by more than a factor of 2.5. This approach requires that the spatial-filter apertures on OMEGA be increased in size beyond the point considered appropriate for a noisy and aging laser system.

Table 133.IX: The 95% encircled-energy radius increase as a result of SSD/DPR versus order of super-Gaussian of “no SSD/DPR” beam. All beams have a “with SSD/DPR” diameter of 860 μm .

Super-Gaussian order	R_b increase (μm)
2	24.5
4	31.8
6	36.1
8	39.6
10	42.1
20	47.3
100	51.6
∞	52.9

2. New DPR Options

To maintain a round focal spot throughout the laser pulse when implementing zooming with a symmetric 2-D SSD kernel, the wedged DPR’s must be removed from the current system. Polarization smoothing, using advanced DPR’s, could be maintained on OMEGA even with fully dispersive 2-D SSD. Several non-wedged DPR options are being developed for use in polar-drive experiments on the NIF. A 4×4 checkerboard array of left-handed and right-handed glancing-angle deposition coatings are being developed at LLE to provide an improved power spectrum with smoothing. Alternatively, a 2×2 checkerboard array of KD*P half-wave plates and air is the baseline DPR for polar drive on the NIF.

REFERENCES

1. J. Nuckolls *et al.*, Nature **239**, 139 (1972).
2. E. I. Moses and C. R. Wuest, Fusion Sci. Technol. **47**, 314 (2005).
3. C. Cavaller, Plasma Phys. Control. Fusion **47**, B389 (2005).
4. J. D. Lindl *et al.*, Phys. Plasmas **11**, 339 (2004).

5. R. L. McCrory, D. D. Meyerhofer, R. Betti, R. S. Craxton, J. A. Delettrez, D. H. Edgell, V. Yu. Glebov, V. N. Goncharov, D. R. Harding, D. W. Jacobs-Perkins, J. P. Knauer, F. J. Marshall, P. W. McKenty, P. B. Radha, S. P. Regan, T. C. Sangster, W. Seka, R. W. Short, S. Skupsky, V. A. Smalyuk, J. M. Soures, C. Stoeckl, B. Yaakobi, D. Shvarts, J. A. Frenje, C. K. Li, R. D. Petrasso, and F. H. Séguin, Phys. Plasmas **15**, 055503 (2008).
6. V. N. Goncharov, T. C. Sangster, T. R. Boehly, S. X. Hu, I. V. Igumenshchev, F. J. Marshall, R. L. McCrory, D. D. Meyerhofer, P. B. Radha, W. Seka, S. Skupsky, C. Stoeckl, D. T. Casey, J. A. Frenje, and R. D. Petrasso, Phys. Rev. Lett. **104**, 165001 (2010).
7. R. K. Kirkwood *et al.*, Phys. Rev. Lett. **76**, 2065 (1996).
8. W. Seka, H. A. Baldis, J. Fuchs, S. P. Regan, D. D. Meyerhofer, C. Stoeckl, B. Yaakobi, R. S. Craxton, and R. W. Short, Phys. Rev. Lett. **89**, 175002 (2002).
9. J. Myatt, A. V. Maximov, W. Seka, R. S. Craxton, and R. W. Short, Phys. Plasmas **11**, 3394 (2004).
10. P. Michel *et al.*, Phys. Rev. Lett. **102**, 025004 (2009).
11. I. V. Igumenshchev, W. Seka, D. H. Edgell, D. T. Michel, D. H. Froula, V. N. Goncharov, R. S. Craxton, L. Divol, R. Epstein, R. Follett, J. H. Kelly, T. Z. Kosc, A. V. Maximov, R. L. McCrory, D. D. Meyerhofer, P. Michel, J. F. Myatt, T. C. Sangster, A. Shvydky, S. Skupsky, and C. Stoeckl, Phys. Plasmas **19**, 056314 (2012).
12. P. Michel *et al.*, Phys. Rev. E **83**, 046409 (2011).
13. S. H. Glenzer *et al.*, Science **327**, 1228 (2010).
14. J. D. Moody *et al.*, Nat. Phys. **8**, 344 (2012).
15. T. R. Boehly, D. L. Brown, R. S. Craxton, R. L. Keck, J. P. Knauer, J. H. Kelly, T. J. Kessler, S. A. Kumpan, S. J. Loucks, S. A. Letzring, F. J. Marshall, R. L. McCrory, S. F. B. Morse, W. Seka, J. M. Soures, and C. P. Verdon, Opt. Commun. **133**, 495 (1997).
16. W. Seka, D. H. Edgell, J. P. Knauer, J. F. Myatt, A. V. Maximov, R. W. Short, T. C. Sangster, C. Stoeckl, R. E. Bahr, R. S. Craxton, J. A. Delettrez, V. N. Goncharov, I. V. Igumenshchev, and D. Shvarts, Phys. Plasmas **15**, 056312 (2008).
17. I. V. Igumenshchev, D. H. Edgell, V. N. Goncharov, J. A. Delettrez, A. V. Maximov, J. F. Myatt, W. Seka, A. Shvydky, S. Skupsky, and C. Stoeckl, Phys. Plasmas **17**, 122708 (2010).
18. D. H. Froula, I. V. Igumenshchev, D. T. Michel, D. H. Edgell, R. Follett, V. Yu. Glebov, V. N. Goncharov, J. Kwiatkowski, F. J. Marshall, P. B. Radha, W. Seka, C. Sorce, S. Stagmitto, C. Stoeckl, and T. C. Sangster, Phys. Rev. Lett. **108**, 125003 (2012).
19. I. V. Igumenshchev, D. H. Froula, D. H. Edgell, V. N. Goncharov, T. J. Kessler, F. J. Marshall, R. L. McCrory, P. W. McKenty, D. D. Meyerhofer, D. T. Michel, T. C. Sangster, W. Seka, and S. Skupsky, “Laser-Beam Zooming to Mitigate Crossed-Beam Energy Losses in Direct-Drive Implosions,” to be published in Physical Review Letters.
20. M. C. Myers *et al.*, Nucl. Fusion **44**, S247 (2004).

21. S. Skupsky, R. W. Short, T. Kessler, R. S. Craxton, S. Letzring, and J. M. Soures, *J. Appl. Phys.* **66**, 3456 (1989).
22. G. Fiksel, S. X. Hu, V. N. Goncharov, D. D. Meyerhofer, T. C. Sangster, V. A. Smalyuk, B. Yaakobi, M. J. Bonino, and R. Jungquist, *Phys. Plasmas* **19**, 062704 (2012).
23. S. X. Hu, G. Fiksel, V. N. Goncharov, S. Skupsky, D. D. Meyerhofer, and V. A. Smalyuk, *Phys. Rev. Lett.* **108**, 195003 (2012).
24. M. C. Herrmann, M. Tabak, and J. D. Lindl, *Phys. Plasmas* **8**, 2296 (2001).
25. "Cross-Beam Energy Transfer in Polar-Drive Implosions on OMEGA," published in this volume.
26. J. Delettrez, *Can. J. Phys.* **64**, 932 (1986).
27. P. B. Radha, T. J. B. Collins, J. A. Delettrez, Y. Elbaz, R. Epstein, V. Yu. Glebov, V. N. Goncharov, R. L. Keck, J. P. Knauer, J. A. Marozas, F. J. Marshall, R. L. McCrory, P. W. McKenty, D. D. Meyerhofer, S. P. Regan, T. C. Sangster, W. Seka, D. Shvarts, S. Skupsky, Y. Srebro, and C. Stoeckl, *Phys. Plasmas* **12**, 056307 (2005).
28. R. C. Malone, R. L. McCrory, and R. L. Morse, *Phys. Rev. Lett.* **34**, 721 (1975).
29. R. Epstein, *J. Appl. Phys.* **82**, 2123 (1997).
30. P. Y. Chang, R. Betti, B. K. Spears, K. S. Anderson, J. Edwards, M. Fatenejad, J. D. Lindl, R. L. McCrory, R. Nora, and D. Shvarts, *Phys. Rev. Lett.* **104**, 135002 (2010); R. Betti, P. Y. Chang, B. K. Spears, K. S. Anderson, J. Edwards, M. Fatenejad, J. D. Lindl, R. L. McCrory, R. Nora, and D. Shvarts, *Phys. Plasmas* **17**, 058102 (2010).
31. R. Betti, presented at the 24th IAEA Fusion Energy Conference, San Diego, CA, 8–13 October 2012.
32. T. C. Sangster, V. N. Goncharov, R. Betti, P. B. Radha, T. R. Boehly, D. T. Casey, T. J. B. Collins, R. S. Craxton, J. A. Delettrez, D. H. Edgell, R. Epstein, C. J. Forrest, J. A. Frenje, D. H. Froula, M. Gatu-Johnson, V. Yu. Glebov, D. R. Harding, M. Hohenberger, S. X. Hu, I. V. Igumenshchev, R. T. Janezic, J. H. Kelly, T. J. Kessler, C. Kingsley, T. Z. Kosc, J. P. Knauer, S. J. Loucks, J. A. Marozas, F. J. Marshall, A. V. Maximov, R. L. McCrory, P. W. McKenty, D. D. Meyerhofer, D. T. Michel, J. F. Myatt, R. D. Petrasso, S. P. Regan, W. Seka, W. T. Shmayda, R. W. Short, A. Shvydkiy, S. Skupsky, J. M. Soures, C. Stoeckl, W. Theobald, V. Versteeg, B. Yaakobi, and J. D. Zuegel, "Improving Cryogenic DT Implosion Performance on OMEGA," submitted to *Physics of Plasmas*.
33. F. J. Marshall, J. A. Delettrez, R. Epstein, R. Forties, R. L. Keck, J. H. Kelly, P. W. McKenty, S. P. Regan, and L. J. Waxer, *Phys. Plasmas* **11**, 251 (2004).
34. F. J. Marshall, J. A. Delettrez, R. Epstein, R. Forties, V. Yu. Glebov, J. H. Kelly, T. J. Kessler, J. P. Knauer, P. W. McKenty, S. P. Regan, V. A. Smalyuk, C. Stoeckl, J. A. Frenje, C. K. Li, R. D. Petrasso, and F. H. Séguin, *Bull. Am. Phys. Soc.* **48**, 56 (2003).
35. O. Morice, *Opt. Eng.* **42**, 1530 (2003).

Measuring 8- to 250-ps Short Pulses Using a High-Speed Streak Camera on Kilojoule, Petawatt-Class Laser Systems

Introduction

Optical streak cameras have been used as the primary diagnostic for a variety of laser and target experiments. OMEGA EP¹ uses a high-speed optical streak camera comprising a P820 streak tube² in a ROSS (Rochester Optical Streak System)^{3–5} to measure the pulse shape for pulse durations ranging from 8 to 250 ps. A small percentage (0.7%) of the main laser beam (370 mm × 370 mm) is picked off by a full-size diagnostic mirror, demagnified to a size of 65 mm × 65 mm by a down-collimator inside the grating compressor chamber (GCC), and transported to the short-pulse diagnostic package (SPDP) residing outside the GCC. This diagnostic beam is further demagnified to 4 mm × 4 mm by three stages of down-collimators inside the SPDP (65 mm × 65 mm to 25 mm × 25 mm, to 12 mm × 12 mm, and, finally, to 4 mm × 4 mm). In the initial configuration, the 4-mm × 4-mm beam was focused onto the input slit of the ROSS by a cylindrical lens. The streak image of the line focus provides the temporal profile and the spatial profile in one direction of the laser beam. The focusing of a laser beam with aberration [approximately 0.5- λ rms (root mean square), $\lambda = 1053$ nm] by a cylindrical lens produces multiple local hot spots within the focal line. Because of shot-to-shot focal-spot pointing and structure variations, these hot spots move across the slit in both the space and time directions, leading to distorted pulse-shape measurements. Moreover, interactions among the photoelectrons transiting in the streak tube cause the electrons to repel each other (space-charge broadening).⁶ This effect is particularly pronounced for shorter pulses, leading to an artificially broadened pulse measurement. The space-charge broadening is further exacerbated by the hot spots imaged onto the photocathode. The signal's sensitivity to far-field-based coupling and the space-charge broadening make it very challenging to operate a streak camera during short-pulse laser operations. The initial shot-to-shot streak measurements are found to exhibit a large signal variation (5:1 is typical), making it operationally impractical to accurately control space-charge-induced pulse broadening and to operate the streak camera within the traditionally defined dynamic range of less than 20% broadening.⁶

We report a beam-homogenizing method that uses an anamorphic diffuser to provide significantly more uniform illumination on the photocathode of a streak camera as compared with the conventional cylindrical-lens coupling approach, therefore increasing the signal-to-noise ratio and the ability to conduct a global space-charge-broadening calibration. A method to calibrate space-charge-induced pulse broadening of streak-camera measurements is described and validated by modeling and experiments.

Anamorphic Diffuser for Uniform Photocathode Illumination

Figure 133.54(a) illustrates a typical streak image of a 230-ps laser pulse obtained with the cylindrical-lens-coupling approach. Figures 133.54(b) and 133.54(c) show the corresponding spatial and temporal profiles, respectively. The hot spots typically induce an undesired 5-to-1 spatial modulation. As shown in Fig. 133.54(c), the pulse shape is also somewhat distorted into a tilted top by the hot spots present during the first half of the pulse. The spatial-profile variation at different times also indicates that the streak image is sensitive to the far-field structure and pointing changes. A new coupling scheme is required to provide more-uniform streak images, higher signal-to-noise ratios, and less sensitivity to focal-spot structure and pointing changes.

An anamorphic-diffuser-based coupler has been developed to provide more-uniform streak images and to increase the signal-to-noise ratio. Figures 133.55(a) and 133.55(b) show the principle of the new coupling approach: it consists of an anamorphic diffuser followed by a spherical focusing lens. The divergence angles of the anamorphic diffuser are 10° and 0.4° along and across the ROSS slit (corresponding to the spatial and temporal directions), respectively. A 12-mm × 12-mm collimated beam is transmitted through the diffuser and diverges into a 10° × 0.4° solid angle. The focusing lens, having a 35-mm focal length, transfers the common angle from the diffuser to the same location on the focal plane, forming a focal line. All the rays with the same angle on the object plane contribute to

the energy collected at a particular location on the focal plane; therefore, any hot spot in the incoming beam will be averaged out at the image plane.

The spatial profile of this diffuser-based coupler was measured with a continuous-wave (cw) laser at a 675-nm wavelength. The profiles along the spatial and temporal directions

are shown in Figs. 133.55(c) and 133.55(d), respectively. The full-width-at-half-maximum (FWHM) spot sizes are $270\ \mu\text{m}$ and $6.1\ \text{mm}$ across and along the slit, respectively. The measured coupling efficiency through a $100\text{-}\mu\text{m}$ slit was 20%.

The diffuser coupler was tested with a ROSS on a pulsed laser system. Figures 133.56(a)–133.56(c) show the measured

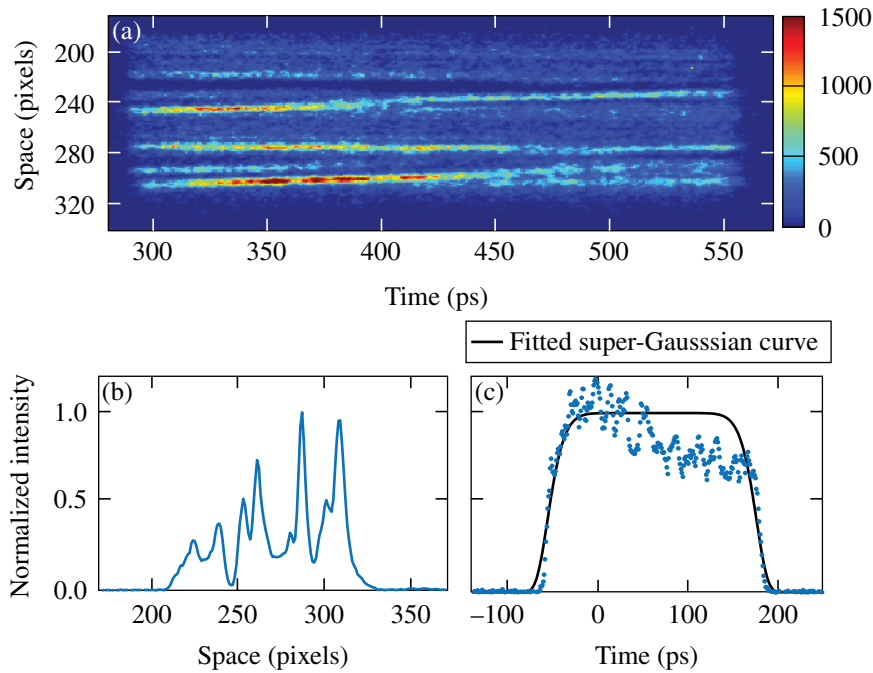


Figure 133.54
(a) Streak image with a cylindrical lens coupling; (b) spatial profile showing modulation from the hot spots; (c) temporal profile distorted by the hot spots.

G9373JR

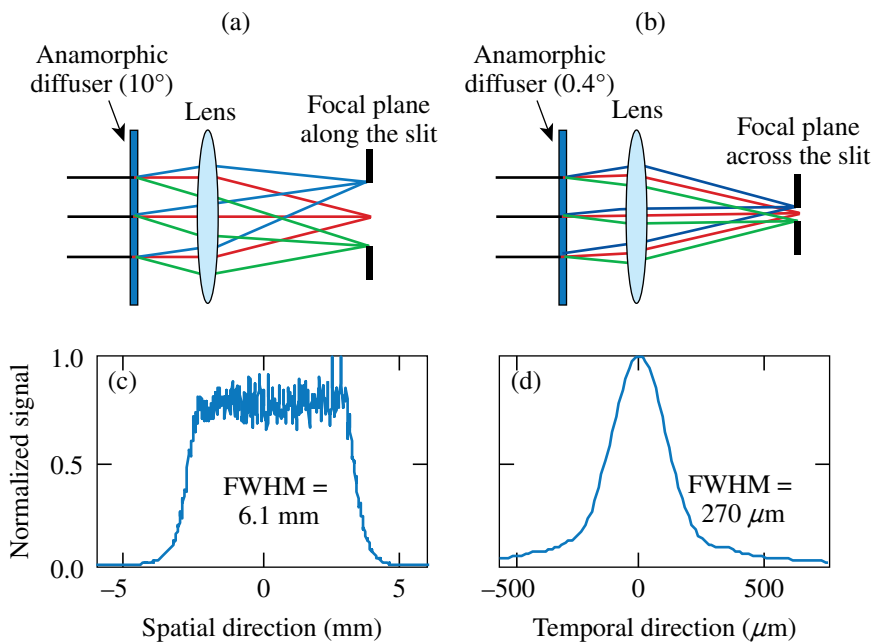


Figure 133.55
[(a),(c)] A 10° divergence angle in the spatial direction achieved a 6.1-mm -long focal line along the slit. [(b),(d)] A 0.4° divergence angle in the temporal direction achieved a $270\text{-}\mu\text{m}$ -wide focal line across the slit.

G9374JR

streak image and spatial and temporal profiles of a 180-ps (FWHM) laser pulse. Compared to the cylindrical-lens coupling results shown in Fig. 133.54, the anamorphic-diffuser-based coupling provides a more-uniform photocathode illumination; the spatial modulation is less than 2:1, down from 5:1 for the cylindrical-coupling approach. Figure 133.57 illustrates

that the temporal distortions induced by the hot spots in region of interest #2 (ROI2) [Fig. 133.57(a)] with the cylindrical lens coupling were eliminated through the more-uniform illumination [Fig. 133.57(b)] on the photocathode with the $10^\circ \times 0.4^\circ$ diffuser [comparing Figs. 133.57(a), 133.57(c) and 133.57(b), 133.57(d)]. Therefore, consistent temporal profiles are achieved

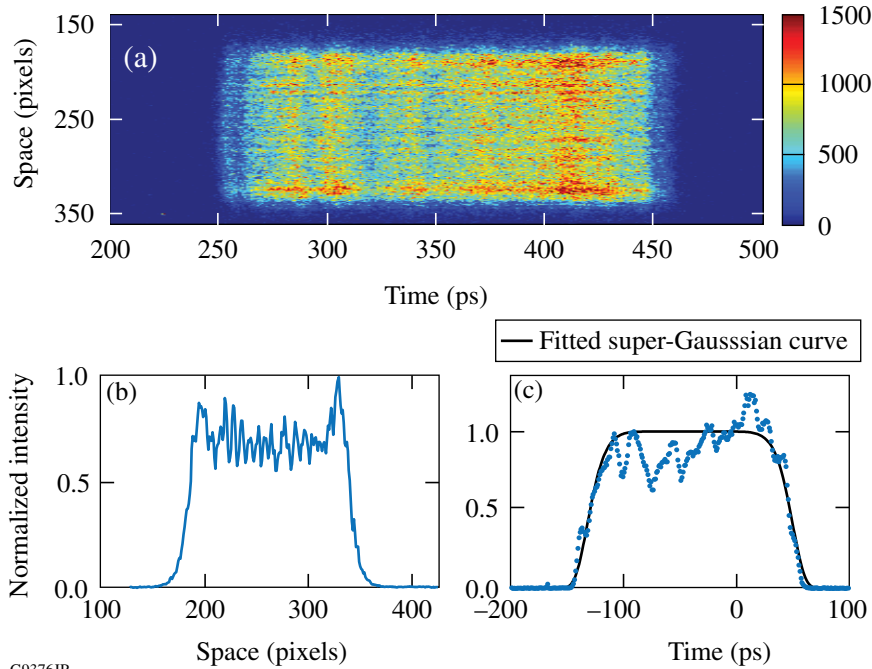


Figure 133.56
(a) A streak image obtained with the $10^\circ \times 0.4^\circ$ diffuser; (b) spatial profile; (c) temporal profile.

G9376JR

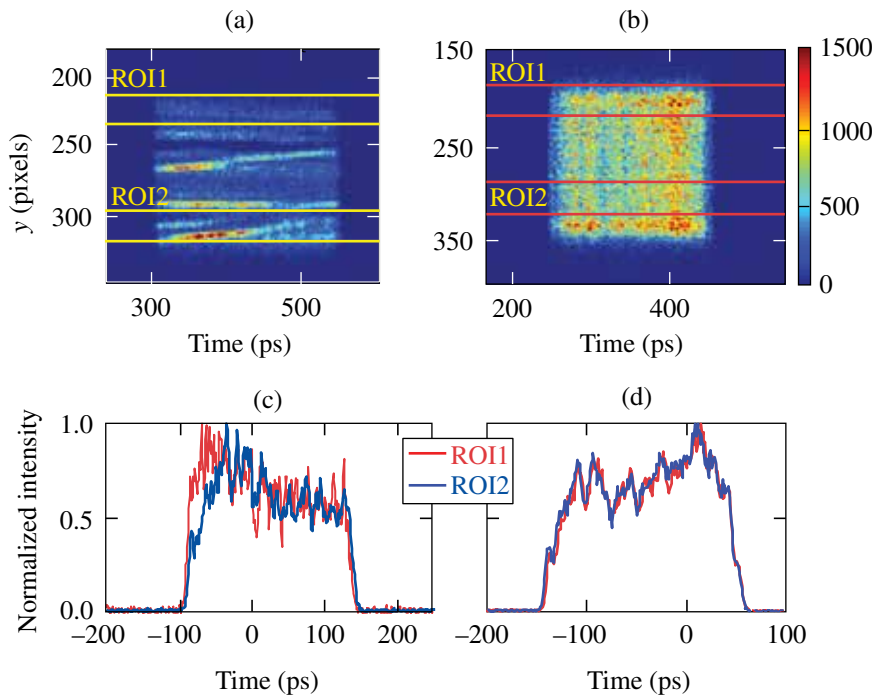


Figure 133.57
[(a),(c)] Streak image and temporal profiles obtained through a cylindrical lens. Temporal profiles were distorted by the hot spots in ROI2. [(b),(d)] Streak image and temporal profiles obtained through a $10^\circ \times 0.4^\circ$ diffuser. Temporal profiles are consistent across the spatial direction.

G9716JR

across the spatial direction. A higher signal-to-noise ratio can be achieved by averaging across the spatial direction without compromising the pulse-shape measurement.

The maximum optical-path difference (OPD) of the rays traveling from the diffuser to the focal plane was investigated in OSLO®, and induced pulse broadening was found to be less than 0.5 ps (140λ , $\lambda = 1053 \text{ nm}$). The impulse response of the ROSS and diffuser-coupler system was measured with a subpicosecond pulse to verify that diffuser-induced pulse broadening was minimal. The measured impulse response width remained at 3 ps (FWHM, shown in Fig. 133.58), narrow enough to measure 10-ps pulses.

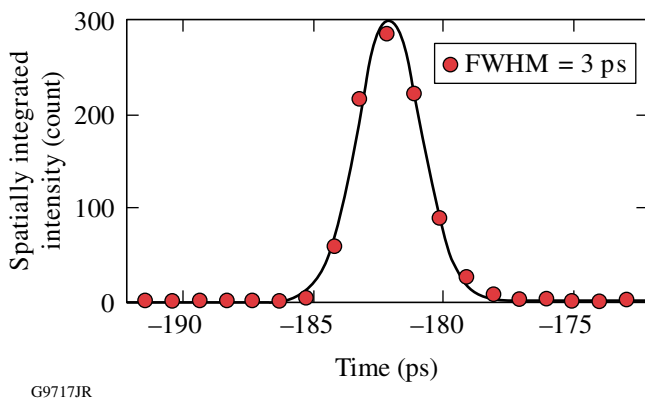


Figure 133.58 Impulse response of the streak camera using the $10^\circ \times 0.4^\circ$ diffuser with a 3-ps FWHM.

Characterization of Space-Charge–Broadening Effects

Maintaining the dynamic range of a streak camera requires that the input signal to the photocathode be controllable under a certain level and stable from shot to shot. However, the large 5-to-1, shot-to-shot streak signal variation makes it difficult to control the space-charge–induced broadening effect. Therefore, the traditionally defined dynamic range is operationally impractical to achieve; the pulse width broadens with an increasing total number of electrons per pulse.

The spatial averaging produced by the diffuser eliminates the local hot spots imaged to the photocathode and subsequently simplifies the space-charge mechanism so that pulse broadening depends on the total current in the tube, rather than on local variations in intensity. As a result, a global space-charge analysis can be used to determine the amount of broadening from the total signal, integrated in space and time.

A method to calibrate space-charge–induced pulse broadening has been developed and validated on OMEGA EP. The input energy to the slit of the ROSS was varied to obtain a series of broadened pulses for each stretcher position. The true pulse width was determined by a linear regression between the measured pulse width and the total pixel values in an analog-to-digital units (ADU’s) measured by the ultrafast ROSS charge-coupled device (CCD). The offset at zero ADU represents the true pulse width without space-charge broadening.

Rather than using a $10^\circ \times 0.4^\circ$ diffuser that provided only 20% coupling efficiency, a $10^\circ \times 0^\circ$ diffuser with 75% coupling efficiency was used to provide sufficient energy for a ROSS on OMEGA EP to characterize the space-charge effects on streak measurements of short pulses with various lengths and shapes. Characterization traces were measured for stretcher positions of 16 mm, 40 mm, and 80 mm (relative to the position corresponding to a best-compression pulse width of approximately 1 ps). With the full front-end spectrum, these stretcher positions produce approximately square pulses with FWHM’s of 23 ps, 58 ps, and 120 ps, respectively, as predicted by a system model. When the beamline amplifiers are fired, spectral gain narrowing produces approximately Gaussian pulses with widths of 10 ps, 25 ps, and 50 ps for these stretcher positions. Figure 133.59 demonstrates that the pulse width linearly increases with the total signal on the photocathode. In the absence of gain narrowing, for stretcher positions of 16 mm, 40 mm, and 80 mm, the regressed true pulse widths are 21.1 ps, 55.7 ps, and 113.7 ps, respectively. The corresponding 95%

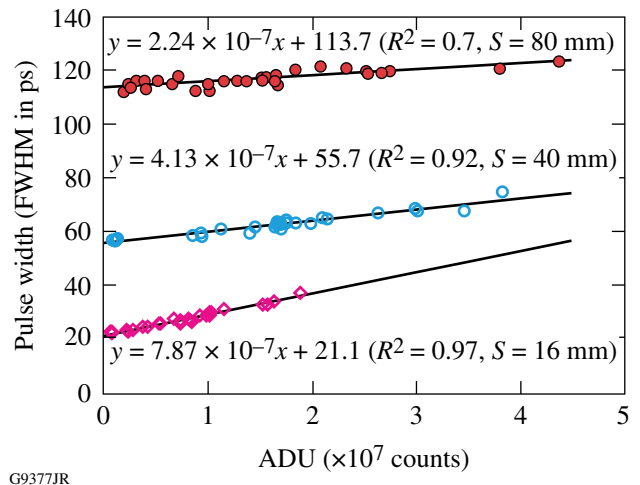
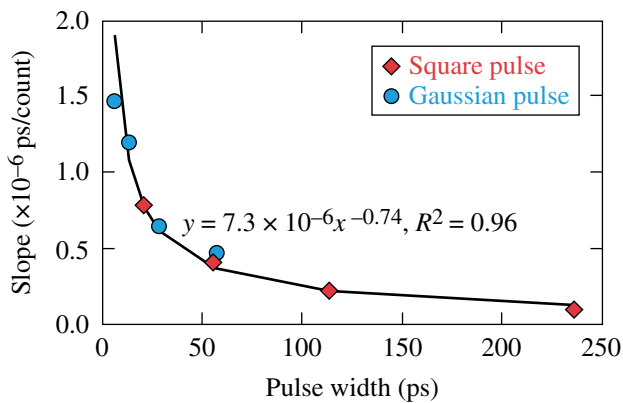


Figure 133.59 Space-charge–broadening calibration for stretcher positions of $S = 16 \text{ mm}$, $S = 40 \text{ mm}$, and $S = 80 \text{ mm}$.

confidence intervals are [20.6 ps, 21.7 ps]; [54.8 ps, 56.7 ps]; and [112.7 ps, 114.7 ps]. The slopes obtained from linear regressions between the measured pulse width and photocathode signal at each stretcher position reveal that the magnitude of the space-charge–broadening effect depends on the stretcher position, i.e., the pulse width to be measured. The shorter the pulse to be measured, the larger the slope, and the more pronounced the space-charge–broadening effects.

Figure 133.60 shows the inverse relation between space-charge–induced pulse broadening (slope) and pulse width (offset) for both square and Gaussian pulses. For the limited number of measurements, the space-charge–broadening effect is comparable for these two pulse shapes, although the electron density at the edges of a Gaussian pulse is smaller than that of a square pulse. One would expect the effect on the former is less than that on the latter because a Gaussian pulse shape distorts to a super-Gaussian and to a square pulse shape with the increasing energy to the input slit.⁷



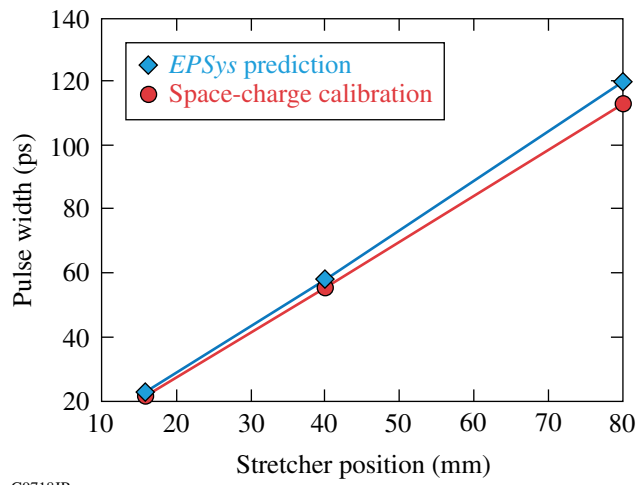
G9378JR

Figure 133.60
Inverse relation between space-charge broadening and pulse width.

During laser operations, the slope of each calibration trace, in conjunction with the streak-image signal level and measured pulse width, can be used to determine the true pulse width, removing space-charge–broadening effects.

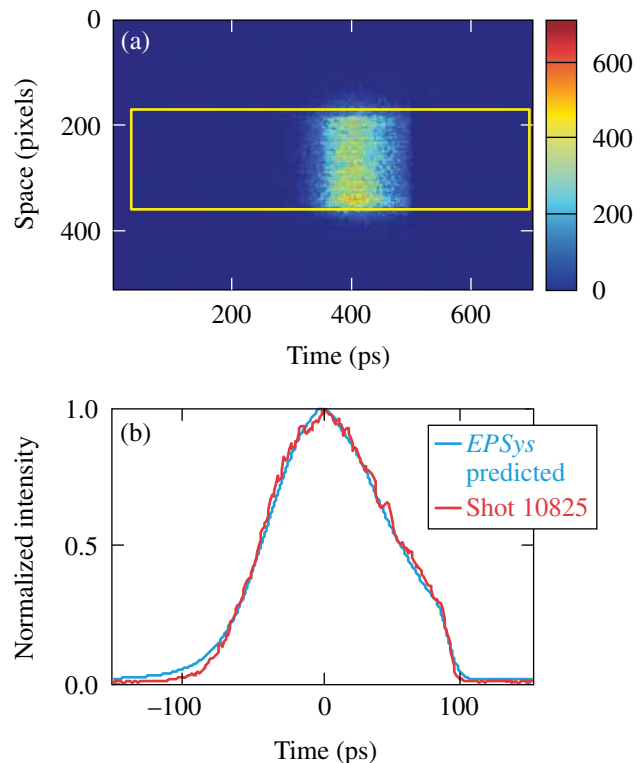
The inferred pulses are compared to the results from an *EPSys* model⁸ that predicts the pulse shape from the measured spectrum, the stretcher and compressor angles, and the stretcher slant distance. The pulse widths determined using the two methods show a systematic error of 5% (Fig. 133.61). Figure 133.62(a) shows a uniform streak image obtained on a high-energy shot. Figure 133.62(b) illustrates that the measured pulse shape, at a low input energy level to minimize space-charge broadening, agrees with the *EPSys*-predicted pulse shape.

To validate the accuracy of the space-charge–broadening calibration method, a <10-ps inferred pulse from the streak-camera measurements was compared to the measurements from



G9718JR

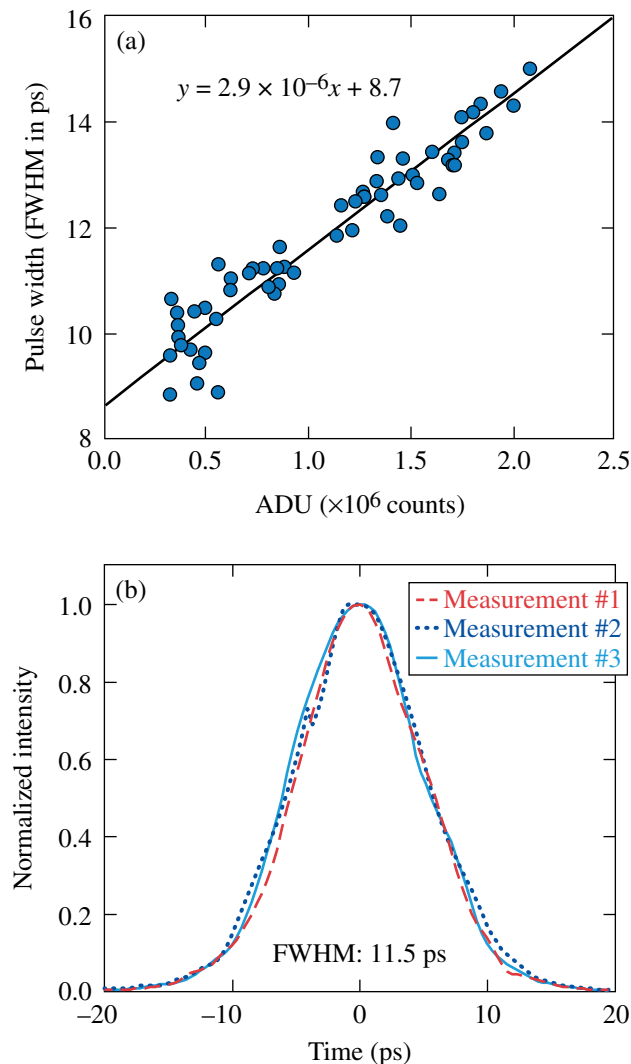
Figure 133.61
Comparison of results from space-charge–broadening calibration and *EPSys* prediction.



G9485JR

Figure 133.62
(a) Uniform streak image achieved on high-energy laser shots; (b) Measured pulse shape and model prediction.

a scanning autocorrelator (suitable for pulses ranging from 0.2 to 20 ps). Figure 133.63(a) shows the streak-camera data. The pulse width (FWHM), after a space-charge-broadening calibration was applied, was $8.7 \text{ ps} \pm 0.5 \text{ ps}$. Figure 133.63(b) shows three consecutive autocorrelation measurements with an averaged FWHM of 11.5 ps and a standard deviation of 0.1 ps. By applying a decorrelation factor of 1.36 (the ratio of the width of the autocorrelation of the pulse predicted by *EPsys* to the width of the pulse itself), the pulse width determined from the scanning autocorrelator was 8.5 ps, which agrees with the space-charge-broadening-calibrated measurement of 8.7 ps by the ultrafast ROSS.



G9550JR

Figure 133.63
 (a) Space-charge-broadening-calibrated pulse measurement (FWHM = 8.7 ps). (b) Three autocorrelation measurements leading to a pulse FWHM of 8.5 ps using a decorrelation factor of 1.36 obtained by modeling.

Conclusions

The insertion of an anamorphic-diffuser coupler provides more-uniform photocathode illumination, less sensitivity to focal-spot pointing and structure changes, and improved space-charge-broadening characterization, resulting in improved pulse-measurement accuracy. A linear regression method was developed to calibrate space-charge-broadening effects. By increasing the effective dynamic range and reducing the sensitivity to wavefront errors, the space-charge-broadening calibration method, in conjunction with the anamorphic diffuser coupler, allows one to more easily operate a streak camera and obtain more-accurate pulse measurements in the 8- to 250-ps range on OMEGA EP. This approach is well suited for other short-pulse laser systems.

ACKNOWLEDGMENT

This work was supported by the U.S. Department of Energy Office of Inertial Confinement Fusion under Cooperative Agreement No. DE-FC52-08NA28302, the University of Rochester, and the New York State Energy Research and Development Authority. The support of DOE does not constitute an endorsement by DOE of the views expressed in this article. The authors thank M. Millecchia and A. Kalb for their support on the anamorphic-diffuser-based coupler testing.

REFERENCES

1. J. H. Kelly, L. J. Waxer, V. Bagnoud, I. A. Begishev, J. Bromage, B. E. Kruschwitz, T. J. Kessler, S. J. Loucks, D. N. Maywar, R. L. McCrory, D. D. Meyerhofer, S. F. B. Morse, J. B. Oliver, A. L. Rigatti, A. W. Schmid, C. Stoeckl, S. Dalton, L. Folsbee, M. J. Guardalben, R. Jungquist, J. Puth, M. J. Shoup III, D. Weiner, and J. D. Zuegel, *J. Phys. IV France* **133**, 75 (2006).
2. PHOTONIS, 19106 Brive, France.
3. W. R. Donaldson, R. Boni, R. L. Keck, and P. A. Jaanimagi, *Rev. Sci. Instrum.* **73**, 2606 (2002).
4. R. A. Lerche, J. W. McDonald, R. L. Griffith, G. Vergel de Dios, D. S. Andrews, A. W. Huey, P. M. Bell, O. L. Landen, P. A. Jaanimagi, and R. Boni, *Rev. Sci. Instrum.* **75**, 4042 (2004).
5. Sydor Instruments, LLC, Rochester, NY 14624.
6. D. J. Bradley *et al.*, *Rev. Sci. Instrum.* **49**, 215 (1978).
7. X. Wang *et al.*, *Rev. Sci. Instrum.* **80**, 013902 (2009).
8. *Final Proposal for Renewal Award for Cooperative Agreement DE-FC52-92SF-19460*, Between the U.S. Department of Energy and the Laboratory for Laser Energetics of the University of Rochester, Part 1: Technical Program (Rochester, NY, 2007), p. 2.245.

A Solid-State, Inductive-Adder, 10-kV Pulse Generator for Driving Large-Aperture Pockels Cells

Introduction

Pockels cells use electro-optic crystals with electrodes to apply electric fields that modulate the birefringence of the crystals and serve as voltage-controlled wave plates in laser systems. When combined with polarizers, these devices operate as optical switches for laser applications that include picking individual pulses from pulse trains, Q -switching laser cavities, isolating the gain of multiple amplifier stages, and protecting stages early in a power-amplifier chain from backward-propagating beams caused by unwanted retroreflections. These applications are illustrated schematically in Fig. 133.64. In this figure, a ring laser amplifier, such as the large-aperture ring amplifier (LARA)¹ or a similar system using Nd:YLF crystals for the laser gain (CLARA),² is shown.

Highly deuterated potassium dihydrogen phosphate (KD_2PO_4 , often abbreviated KD^*P or DKDP) is a common crystal used in Pockels cells, especially in devices that apply the electric field in the direction of the light beam propagation when large apertures are required. An important property of a Pockels cell is the half-wave voltage V_π . It is defined as the potential producing a retardance within the Pockels cell that rotates linear polarized light 90° to change the transmission state through an accompanying polarizer from minimum to maximum. The half-wave voltage for KD^*P Pockels cells with longitudinal electrodes is approximately 8 kV, which is roughly independent of the aperture size. Voltage pulses up to 9 kV are needed to accommodate losses.

Figure 133.65 shows high-voltage pulse generation and delivery schemes used to drive Pockels cells. These cells form

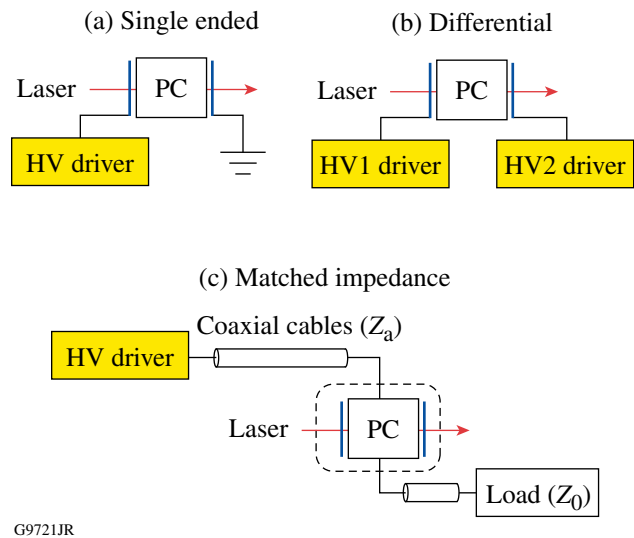


Figure 133.65 Pockels cell schemes. (a) A low-impedance, high-voltage (HV) half-wave driver is connected directly to the Pockels cell in the single-ended scheme. (b) Two low-impedance quarter-wave voltage drivers of opposite polarity are connected directly to the Pockels cell in the differential scheme. (c) In the matched-impedance scheme, a half-wave driver is connected to a Pockels cell, shunted with a resistance Z_0 , via a coaxial line of characteristic impedance Z_0 .

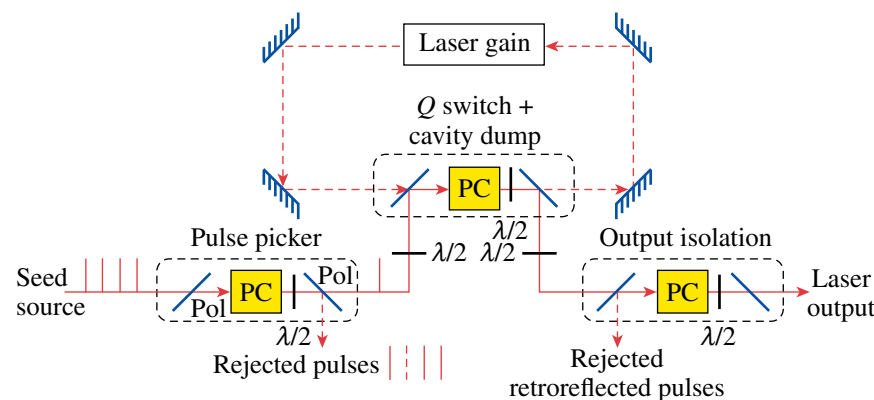


Figure 133.64 Applications of Pockels cells in laser systems. Pulse pickers use a Pockels cell (PC) between polarizers (Pol) in combination with a half-wave plate ($\lambda/2$) to select an individual pulse from a repetitive seed source. Output isolation stages similarly gate through single pulses to reject pulses leaked from multipass amplifiers; in addition, they protect front-end systems from retroreflected light. Pockels cells are used to Q -switch and cavity-dump multipass laser cavities.

G9720JR

capacitive loads with capacitance ranging from a few picofarads for small cells to hundreds of picofarads for large-aperture cells. Drive schemes include single-ended³ [Fig. 133.65(a)] and differential⁴ [Fig. 133.65(b)] schemes with short-length connections that directly drive the electrodes to limit pulse distortion resulting from parasitic reactances. Also illustrated is a matched-impedance driver⁵ [Fig. 133.65(c)] that delivers high-voltage pulses on shielded coaxial cable to a resistively shunted Pockels cell with resistance equal to the characteristic impedance of the coaxial line Z_0 . Two advantages of the coaxial-cable matched-impedance driver scheme are limited radiated electromagnetic interference (EMI) and the option of physical separation of the pulse generator from the Pockels cell with minimal distortion of the driver pulse shape.

A commonly used matched-impedance Pockels cell driver employs a thyratron electron tube as a closing switch to connect a fixed-length charged transmission line (charge line) to the Pockels cell.⁵ This design generates high-voltage pulses with nanosecond switching times required for many applications. The charge line produces a rectangular pulse at half of the line charge voltage and twice the transmission line's pulse propagation length. Thyratrons designed for this application can switch voltages and currents up to 25 kV and 1 kA, respectively, and one device per pulser is generally used. Unfortunately, these electron tubes degrade with operation. Currently, aging thyratron pulsers are no longer serviceable since manufacturers have discontinued production of suitable thyratron replacement tubes.

It is desirable to replace thyratron-based drivers with drivers based on solid-state devices to avoid matched-impedance drivers based on modern solid-state devices is desirable to avoid degradation over time, improve reliability, and address availability issues associated with electron tubes. Several fast-switching, high-voltage, high-current technologies exist including metal-oxide-semiconductor field-effect transistors (MOSFET's),⁶ avalanche bipolar transistors,⁷ dynistors,⁸ and drift-step-recovery diodes.⁹ A fundamental advantage of MOSFET's compared to the other devices is that they can be turned on and off using low-voltage gate drive signals, allowing them to act as both opening and closing switches, making it possible to adjust output-pulse lengths without changing charge-line hardware. Avalanche and dynistor devices act only as closing switches and require a hardware pulse-forming network, such as a charge line, to set the duration of the output pulse. High-voltage MOSFET's are economical and produce fast switching speeds of less than 5 ns. Fast-switching, high-voltage MOSFET's can switch 1.2 kV at currents in the tens of amperes for each device and can be configured in various

series- and parallel-connected networks to increase the total switching voltage and current capability.

The circuit topology used in this design—an inductive adder schematically illustrated in Fig. 133.66—is a circuit utilizing inductive coupling to achieve high-voltage pulse outputs from lower-voltage, ground-referenced pulse generators, or primary drivers. The output pulse is initiated when the switches in each primary driver simultaneously close and provide a current path from the charge-storage capacitors across the transformer's primary winding. The desired output level is obtained by series connecting, or adding, a sufficient number of individual transformer secondary windings. The pulse is terminated when the primary switches open and the primary current flow ceases. The lower-voltage primary driver units improve reliability and reduce switching device and charge-storage voltage requirements, as well as circuit layout stand-off requirements. The inductive-adder topology allows one to adjust both pulse amplitude and duration without changing the pulser's internal components.

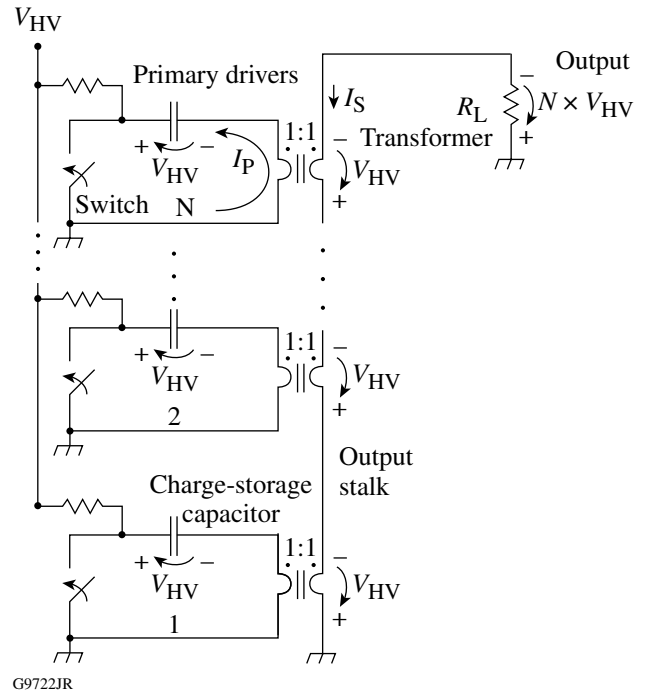


Figure 133.66 Inductive-adder schematic. When the switches simultaneously close within the N primary driver circuits, the charge-storage capacitance creates a current in the primary circuit of each coupled inductor (transformer). This current is inductively coupled to each transformer secondary and creates a voltage equal to the capacitor charge voltage. The secondary of each transformer is series connected to add the pulse voltage from each primary circuit and apply it to the load R_L .

Inductive-adder technology for driving Pockels cells has been demonstrated at voltages of tens of kilovolts and currents of hundreds of amperes with switching times less than 10 ns. Original designs were developed at Lawrence Livermore National Laboratory (LLNL) for fast pulse beam “kickers” in particle accelerators¹⁰ and adapted at LLE to produce 20-kV pulses to switch the plasma-electrode Pockels cell (PEPC) in the OMEGA EP laser, where a closing and opening switch was required to produce the necessary double-pulse waveform.¹¹ Five solid-state switch-pulse PEPC driver (SS-SPD) units have been fielded at LLE since 2005 with performance and reliability far exceeding that of equivalent thyatron-based drivers.

A solid-state, high-voltage pulse generator based on inductive-adder technology for driving 50-Ω, KD*P Pockels cells is reported. The design considerations, subsystem characteristics, and electrical and optical performance are presented, as well as considerations to optimize the design for other potential applications.

Solid-State Pockels-Cell Driver Design

The requirements for a matched-impedance, solid-state Pockels-cell driver (SSPD) are summarized in Table 133.X. The output voltage and output impedance specifications determine the transmission values and stability for large-aperture KD*P Pockels cells¹² used in the half-wave applications illustrated in Fig. 133.64. The electrical pulse-timing values determine the

Table 133.X: Solid-state Pockels-cell driver requirements.

Specification	Requirement
Output Voltage	
Peak output	5 to 10 kV
Peak voltage stability	<±3%
Pre-/post-pulse voltage	<±3%
Flattop variation	<±4%
Output Impedance	50 Ω
Pulse Timing	
10% to 90% rise time	<10 ns
90% to 10% fall time	<10 ns
Pulse duration	9 to 100 ns
Pulse jitter	<200-ps rms
Maximum repetition rate	10 Hz
External Trigger	5-V Logic Edge
Output Voltage Monitor	10,000:1
Primary Power	110/220 VAC, 50/60 Hz

maximum usable laser pulse length in a multipass laser amplifier and the maximum repetition rate of laser pulse trains from which a single pulse can be isolated.

State-of-the-art, fast-switching, high-voltage (1200-V) power MOSFET’s, de-rated to 750 V, are utilized in the design of the primary drivers. A charge-storage voltage of 750 V requires an inductive-adder stack of at least 15 transformers to produce output-pulse voltages up to 10 kV, accounting for inductive coupling and driver losses. This circuit is shown schematically in Fig. 133.67. The 15 identical transformers and corresponding primary drive circuits are easily maintained, repaired, and inventoried as spares. An adjustable 750-V (dc) power supply charges all of the primary drive circuit charge-storage capacitors to the appropriate voltage for the desired pulse amplitude. The driver circuits are triggered simultaneously from a common trigger conditioning system initiated from an external 5-V logic trigger edge. Details of these subsystems and other features of the SSPD are provided below.

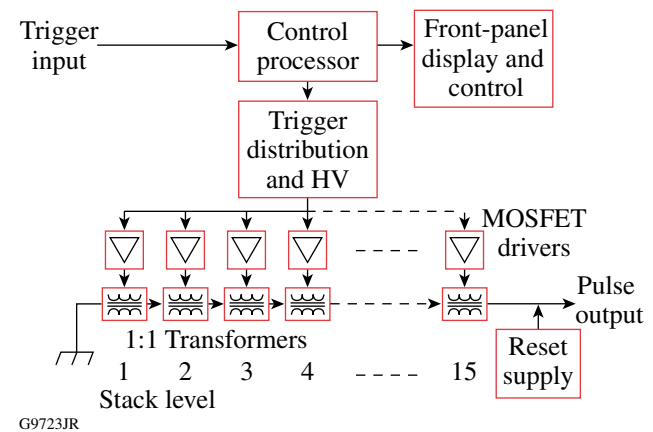
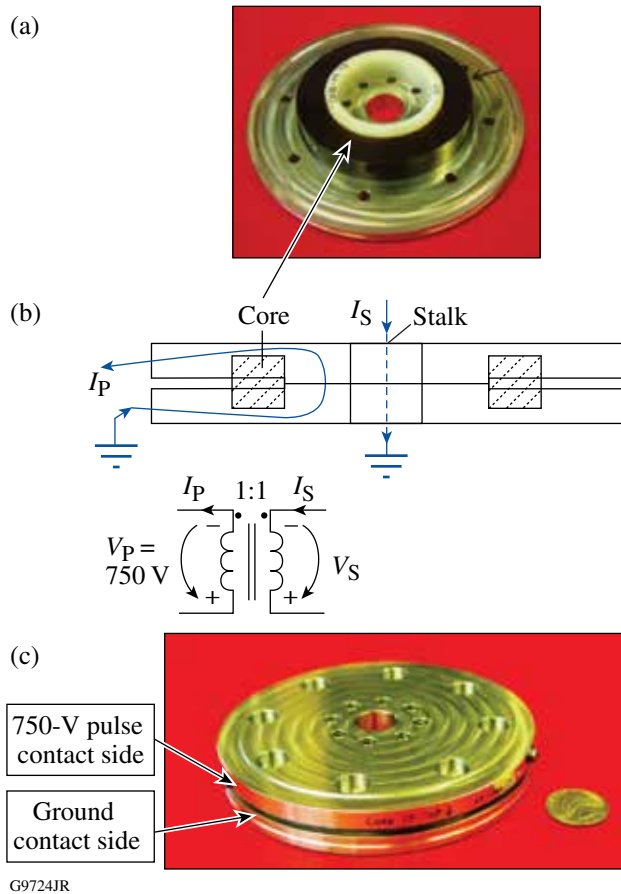


Figure 133.67 Schematic diagram of the solid-state Pockels-cell driver (SSPD). The pulser consists of 15 ground-referenced drivers, each driving a 1:1 transformer with secondaries series-connected to form the high-voltage output pulse.

1. Pulse Transformer Design

An inductive-adder transformer is illustrated in Fig. 133.68. The transformer uses a single-turn, solid primary winding machined from aluminum that completely surrounds a toroidal transformer core [Fig. 133.68(a)]. This configuration maximizes the inductive coupling between primary and secondary by minimizing the leakage inductance from uncoupled magnetic fields. Leakage inductance appears in series with the primary drive circuit, directly impacting high-frequency performance and resulting in increased pulse transition times and reduced pulse amplitude. The secondary circuit of the transformer



G9724JR

Figure 133.68 Inductive-adder transformer cell. [(a),(b)] The 750-V pulse contact side of the primary winding of a cell is isolated from the ground side of the next transformer above by standoffs seated on the ground contact side. (c) The standoffs are positioned in eight cut-outs (holes) in the 750-V side with sufficient air-gap clearance. The standoffs provide both isolation of the 750-V contact side and connection of successive transformers ground contact sides in the stack. Threaded rods extend through the center of the standoffs to hold the cells in the stack together. An isolated conductive rod extends through the center hole of each transformer to form the series-connected secondary circuit.

structure is created by passing an isolated metal rod through the center of the transformer structure [Fig. 133.68(b)]. This metal rod extends through the entire stack of transformer cores, thereby series-connecting the secondaries of each. This rod is termed the “stalk.”

A toroid core geometry was chosen to create an efficient magnetic coupling path between the primary and secondary that had minimal leakage inductance. The size of the core is selected to have sufficient cross-sectional area and magnetic path length (average circumference) to support the pulse voltage–time product without magnetic-flux saturation of the core material. If core flux saturation occurs, the single-turn primary

drops to a very low impedance, which results in catastrophic over-current failure of the primary drive circuits. A safety margin was applied to the design of the transformer core to ensure that the magnetic-flux density in the core is three times less than the saturation flux density for the longest pulse of the largest amplitude.

The first step in the design is to determine the core material and size for the 1:1 single-turn transformer. The core is constructed from a tape-wound, low-loss amorphous ferromagnetic alloy. The core material was selected for its large saturation flux density and low loss. This type of core provides high coupling over a wide bandwidth extending into the VHF (very high frequency) range. The core material chosen was Metglas 2601SA1 (Ref. 13), which is the same material used in the SS-SPD for the OMEGA EP PEPC pulser.¹¹ The material saturation flux density swing (ΔB_{sat}) is 3 teslas (T). The maximum operational flux density was set at 1 T to provide a 3× safety margin. The core effective cross-sectional area A_e to achieve this flux density is derived from the standard equations for flux density B (tesla), inductance L (henrys), and voltage of a toroid wound inductor:¹⁴

$$A_e = \frac{3 \cdot V \cdot \Delta t}{\Delta B_{\text{sat}} \cdot PF} \text{ (m}^2\text{)}, \quad (1)$$

where V is the maximum voltage across the primary circuit for the pulse duration Δt and PF is the core packing factor defined as the ratio of the ferromagnetic material cross-sectional area to the overall cross-sectional area of the core material. The value of 3 in the numerator relates to the safety margin.

With the values of $V = 750\text{ V}$, $\Delta t = 100\text{ ns}$, $\Delta B_{\text{sat}} = 1\text{ T}$, and $PF = 0.65$, $A_e = 1.15\text{ cm}^2$ is obtained. A toroid core with a 1.27-cm^2 cross section was chosen. Once the cross-sectional area is calculated, the circumference of the toroid must be determined. For a transformer, the inductance of a winding, with all others open-circuited, is termed the “magnetizing inductance.” This inductance is electrically in shunt with the drive or load circuitry of that winding. The magnetizing inductance must be large enough that the current through the inductor at the end of the maximum amplitude pulse will not create distortion by excessive loading. Ideally, a large inductance is desirable; however, a tradeoff must be made since a large inductance requires a small core diameter. A small core diameter decreases the driver circuit board’s component placement area if minimum current path length is required for low leakage inductance. The circumference was selected

as a compromise between magnetizing inductance value and driver circuit board's component physical layout. The chosen 3-in. outer diameter produces a magnetizing inductance of approximately 2 μ H as calculated using Eq. (2) (Ref. 14):

$$L = \frac{\mu_0 \mu_r N^2 A_e}{l_e} \text{ (H)}, \quad (2)$$

where the number of turns $N = 1$, $\mu_0 \mu_r$ is the core material's magnetic permeability, and the effective magnetic path length or the average circumference l_e is $2\pi(r = 2.5\text{-in.}/2)$. An inductance of 2 μ H produces a magnetizing current of about 13% of the total primary current at the end of the longest pulse operation.

Another characteristic of the ferromagnetic core material is the core magnetization current. This current is required to overcome the permanent magnetization of the core material since it will take on an amount of permanent magnetization. This is exhibited in the hysteresis loop of the $B-H$ curves (magnetic field versus flux density).¹³ An $\sim 45\text{-A}$ magnetization current is required for the core material chosen in this design to overcome the magnetization hysteresis.

2. Primary Drive Circuit

A simplified schematic of the transformer and the associated primary drive circuit is illustrated in Fig. 133.69. The primary drive to each transformer of the inductive adder is produced by a low-impedance, pulsed-voltage source formed by a group of 12 parallel-connected MOSFET's and a bank of charge-storage capacitors. The pulsed-drive units are connected to the primary

winding along its circumference to minimize parasitic inductance. The primary driver is split into two identical printed wiring boards that plug into the transformer circumference from opposite sides for ease of assembly and maintenance. The number of parallel-connected MOSFET's for each primary driver is determined by the sum of the current required at the output plus the core magnetizing and magnetization currents. The total primary current is equally divided among the parallel-connected, synchronously triggered MOSFET's. The design uses a higher MOSFET count than what is minimally required to switch the output current level to provide a safety margin. In the SSPD design, the maximum MOSFET operational current is limited to 64% of the MOSFET pulsed maximum current as specified by the MOSFET manufacturer.⁶

The primary-driver board is illustrated in Fig. 133.70. This board contains the high-voltage-power MOSFET's as well as the MOSFET gate-driver integrated circuits and charge-storage capacitors. The MOSFET gate-driver integrated circuit is a low-voltage (24-V), 14-A peak switching current driver specifically designed to drive MOSFET gates with nanosecond switching times. Each MOSFET has its own gate driver to maximize switching speeds. The charge-storage capacitors charge to the potential of the primary pulse voltage, which is theoretically $15\times$ less than the actual output-pulse voltage. The capacitors are effectively connected across the primary winding when the MOSFET turns on (low impedance from drain to source). The pulse output current flows from the discharging storage capacitors through the primary winding and is coupled to the secondary via the transformer. The charge-storage capacitor value is calculated to support the output current pulse requirement with less than a 1% droop in charge voltage over the maximum

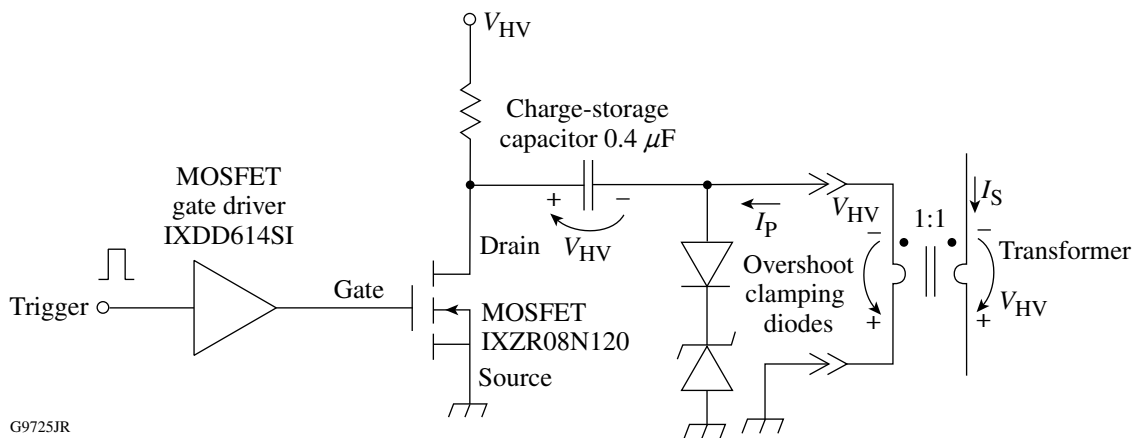


Figure 133.69
Schematic of the transformer primary drive circuit.

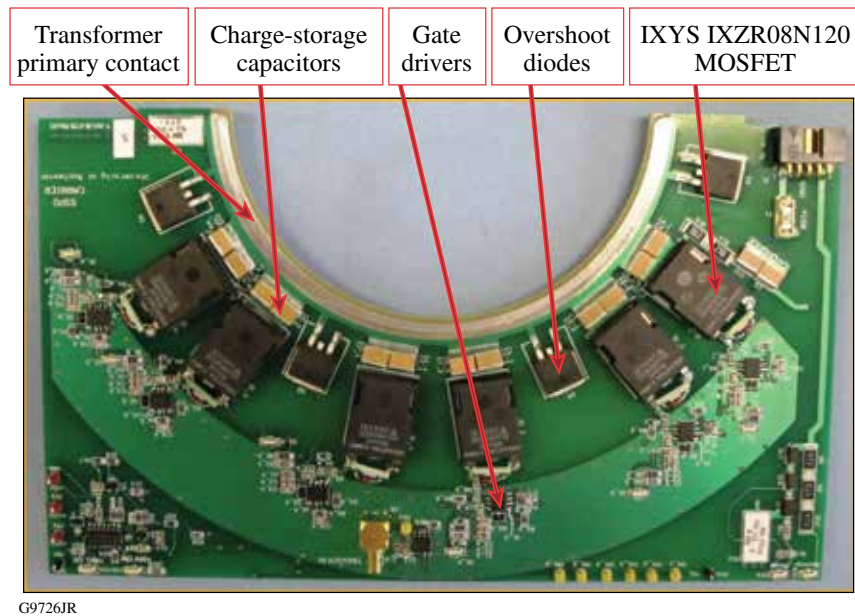


Figure 133.70

MOSFET driver board. The MOSFET driver board contains the circuitry to produce the pulsed voltage to the primary of the inductive-adder transformers. Each transformer has two driver boards that plug in and connect to the circumference of the primary winding. Each driver board contains six MOSFET's.

pulse duration. Overshoot clamping diodes are included in the driver circuit and connected across the transformer primary. The diodes clamp the inductive spike voltage produced by the magnetizing and leakage inductance when the MOSFET driver turns off (high impedance from drain to source). Clamping prevents the drain-to-source spike from exceeding the breakdown voltage of the MOSFET's while preventing output post-pulse ringing and overshoot.

To drive the 50- Ω -loaded LARA and CLARA Pockels cells, the maximum load current is 200 A with the maximum load voltage set at 10 kV. The total primary current is approximately 280 A, including the magnetization current and the magnetizing inductance current. IXYS-Colorado Semiconductor IXZR08N120 1200-V MOSFET's were chosen to provide sufficient voltage-breakdown headroom to prevent inductively generated overshoot in the transformer primary circuit waveforms from damaging them. These devices are also designed for ultralow internal capacitance and parasitic inductance to enhance switching speed. Twelve MOSFET devices are connected in parallel for each primary winding to limit the drain switching current to 23 A per device for the maximum duration and amplitude output pulse. The MOSFET pulsed drain current rating is significantly higher (40 A) (Ref. 6), but allowances are made for adverse load conditions, such as capacitive transients and arc-over short circuits.

When switching a MOSFET, the gate is biased positively with respect to the source to create a negative charge accumulation within the drain-source conduction layer. The gate is insulated from the other terminals of the device by the gate oxide layer above the conduction channel. The negative charge in the conduction layer creates a low-impedance channel for electron flow between the drain and source, thereby turning the MOSFET switch on. The insulated gate is mainly capacitive in nature with respect to the other terminals of the device. The gate capacitance is increased by the Miller switching capacitance effect between the gate and drain while they are changing potential.¹⁵ Taking the Miller effect into account, the total gate input switching capacitance is of the order of 28 nF. The MOSFET gate driver's integrated circuit (IC) from the Clare Semiconductor division of IXYS (IXDD614SI) provides peak gate currents up to 14 A to charge and discharge the gate input switching capacitance. With 14 A, the charge rate for 28 nF across the gate switching transition of 2.5 V is 4.9 ns. This rate is fast enough to switch the MOSFET in the time required by the overall pulser performance specification.

The charge storage for the primary current pulse must be sufficient to restrict voltage droop over the pulse duration. For the SSPD design, the droop was limited to 7.5 V (1%) for a 100-ns pulse at full load current. The total charge-storage capacitance was calculated to be 4.8 μ F to meet this require-

ment. This is divided into 12 0.4- μF capacitor blocks, one in the drain circuit of each of the 12 MOSFET's. Each capacitor block is formed from four individual 0.1- μF , 1000-V ceramic multilayer capacitors.

Groups of overshoot clamping diodes are connected across the primary transformer winding to dissipate the energy within the leakage and magnetizing inductance after the MOSFET's are turned off. This limits ringing and overshoot on the trailing edge of the output pulse and protects the MOSFETs from overvoltage breakdown failure.

The charge storage, MOSFET's, and driver IC's are split into two boards that plug into the circumference of the transformer primary winding to minimize circuit path lengths, thereby minimizing the leakage inductance effects. Splitting the drivers onto two boards also simplifies transformer assembly and removal/repair of the driver boards. Each board contains diagnostic test points and light-emitting-diode (LED) fault indicators to facilitate diagnosis of board failures. Diagnostics are focused on isolating failures down to the component level for quick repair turnaround.

Fifteen identical driver/transformer units (30 driver boards and 15 transformers) are required in the pulser stack to sum the output level to that required in the output specifications defined in Table 133.X. The inductive-adder stack is illustrated in Fig. 133.71.

3. Output Stalk

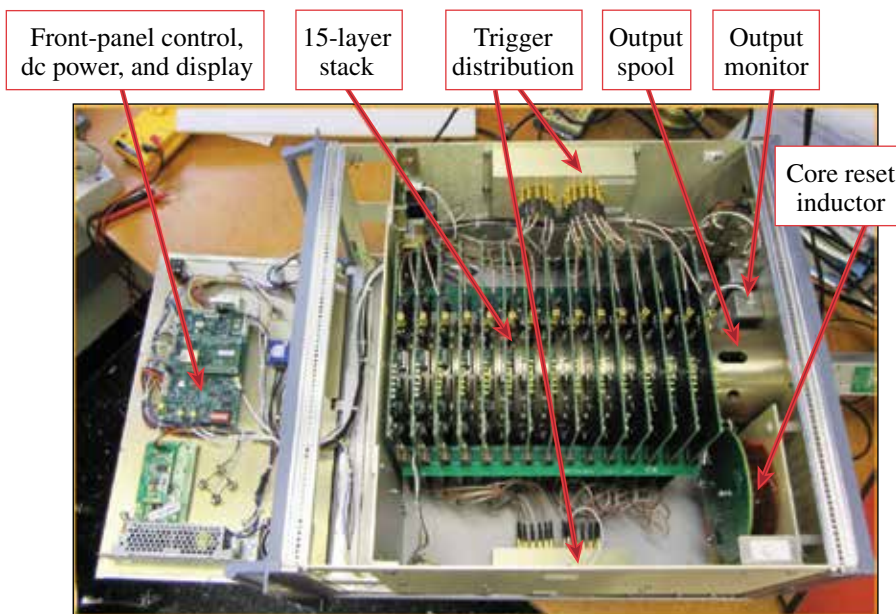
The series-connected secondary of the stacked transformers is a single conductive rod (the output stalk) that extends through the center of each transformer. One end is connected to ground and the other is connected to the 50- Ω output connector. Previous modeling studies have indicated that the stalk characteristic impedance should be set equal to the standard load impedance for optimal rise- and fall-time performance.¹⁶ The stalk characteristic impedance is given by

$$Z_0 = \sqrt{\frac{L_{\text{stalk}} + L_{\text{leakage}}}{C_{\text{stalk}}}}, \quad (3)$$

where L_{stalk} is the inductance of the stalk per unit transformer length, L_{leakage} is the transformer leakage inductance for each individual transformer placed in series with the stalk inductance with the MOSFET switch on, and C_{stalk} is the capacitance of the stalk to ground per unit transformer length. For this design, the stalk diameter is adjusted to provide optimal matching to 50 Ω , the load impedance of the pulser.

4. Control

Overall control of the pulser is accomplished by utilizing an embedded microprocessor. The microprocessor controls operational conditions of the pulser and monitors safety and failure detection circuits. The processor is capable of remote control communications via an Ethernet connection; however,



G9727JR

Figure 133.71
SSPD pulser stack with top cover removed and front panel open. All circuit boards are accessible without major disassembly of the enclosure.

this feature has not been implemented in the current design pending an operational need. The control assembly also conditions the incoming trigger to produce the desired output-pulse length. The externally supplied input trigger pulse edge is used to initiate an adjustable-width pulse generator, which is the source for internal synchronous triggers utilized by each of the 30 driver boards. The pulse length is adjustable in binary steps with a maximum length of 100 ns and a resolution of 0.5 ns. The front-panel interface is also implemented within the control assembly. This interface provides a menu-driven display with a simple push button panel for control of the pulser operation.

5. Front-Panel Display

The front-panel display is an LCD-backlit display that provides pulser operational information. The display includes three pages of information containing control firmware revision status, pulse voltage setting and output level, pulse output length, pulse output state (on/off), and fault status.

6. Trigger Distribution

Each of the 30 driver boards requires a synchronous trigger of the appropriate duration for the desired output pulse. To accommodate this, we use two 1-to-15 active trigger splitters whose trigger source is supplied by the trigger conditioning circuits on the control assembly board. Each splitter has a trigger driver integrated circuit and a resistive trigger splitter that can drive 15 driver board trigger inputs terminated in 50 Ω . The triggers are supplied to each transformer driver board via equal-length, 50- Ω shielded coaxial cables to maintain synchronization of all triggers on the stack.

7. Reset-Current Circuit

The output pulse is a unipolar pulse, and over repeated pulses, the transformer cores will take on a permanent magnetization that will saturate the magnetic core material. To avoid core saturation, a direct current (dc) is connected into the output stalk of opposite polarity to the output current. The dc current is called the “core reset current.” The supply to produce this current must be isolated from the output pulse with a low-pass filter constructed from a large series inductor capable of withstanding the longest-duration and maximum-amplitude pulse output voltage.

8. High-Voltage Power Supply Control

The high-voltage supply is the main charging supply for the charge-storage capacitors on the MOSFET primary circuit driver boards. This supply is adjustable from 0 to 750 V in accordance with the desired output-pulse voltage. This supply is set by the controller board in response to an operator’s

front-panel commands. The controller board monitors a scaled version of the supply output voltage to verify that the supply is operating correctly. The controller displays the monitor value as well as the set-point value on the front-panel display.

9. Housekeeping Supply

The low-potential dc power for all of the circuit boards throughout the pulser is provided by the housekeeping power supply, which is 24 V dc. Lower voltages, like 12 V, 5 V, and 3.3 V, are regulated down on individual boards as required by the circuitry contained on each assembly. The controller board monitors the 24-V housekeeping supply and will issue a fault if the supply drops below a prescribed fault threshold value.

10. Enclosure

The packaged SSPD prototype is shown in Fig. 133.72. The enclosure is a standard 19-in. rack-mount chassis that is six rack units (6 U = 10.5 in.) high and 20 in. deep. The enclosure is designed to facilitate assembly and for ease of pulser repair. All stack MOSFET driver boards are accessible through removable top and bottom covers, as shown in Fig. 133.71. The front panel hinges forward to allow access to the control board and dc supplies.



G9728JR

Figure 133.72
Solid-state Pockels-cell driver package.

11. SSPD Electrical Performance

Two SSPD prototype units were assembled and tested with nearly identical performance into a 50- Ω load network. Figure 133.73(a) illustrates electrical output for approximately 100-ns-long pulses at various output levels. The inset table summarizes the performance parameters at the approximate quarter- and half-wave voltages for KD*P Pockels cells (5 kV and 10 kV, respectively). Figure 133.73(b) shows the measured

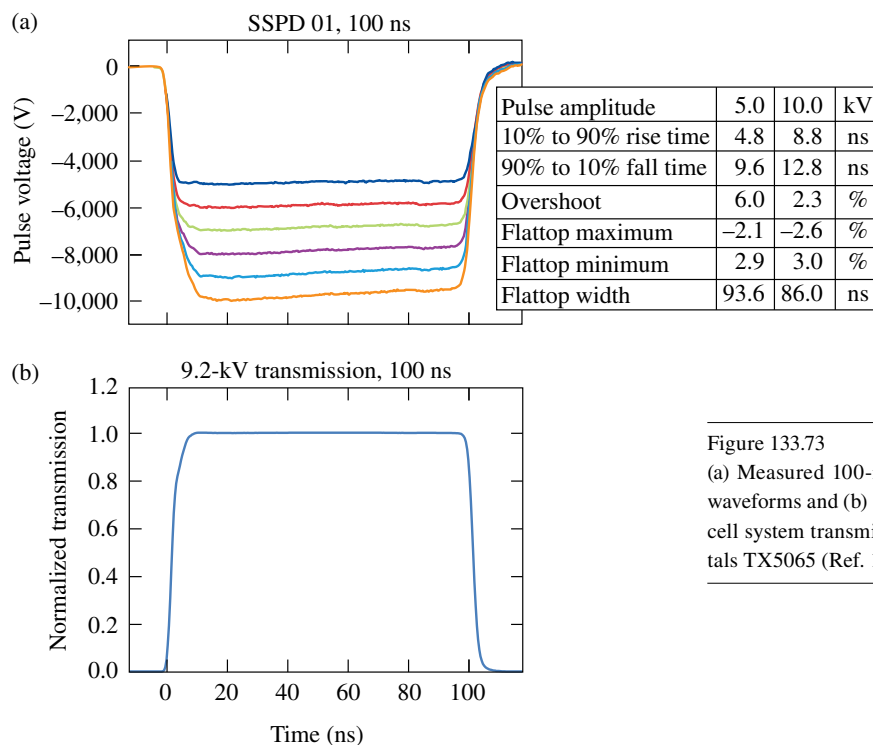


Figure 133.73
 (a) Measured 100-ns output pulse electrical waveforms and (b) 100-ns measured Pockels-cell system transmission for Cleveland Crystals TX5065 (Ref. 12).

G9729JR

transmission of a Pockels cell [Cleveland Crystals TX5065 (Ref. 12)] driven by the SSPD. Similarly, Fig. 133.74 shows the measured electrical SSPD output and calculated optical performance for approximately 25-ns pulses.

A prototype SSPD pulser was connected to a 25-mm Pockels cell [Cleveland Crystals TX-2650 (Ref. 12)] operating as a cavity Q-switch in a CLARA and tested. Measured laser performance, including energy stability and pulse shape, matched performance produced by the thyatron pulser that was replaced by the prototype SSPD unit.

Future Considerations

Future enhancements can be explored to improve SSPD operation, including optimizing the transformer core size to improve output-pulse fidelity. Core selection can be further optimized to improve rise and fall time as well as reduce the magnetization current. The mechanical design of the transformer can also be improved to reduce the cost of manufacture as well as weight.

The number of parallel-connected MOSFET's in each stack could be reduced by working each at higher pulsed currents. This may improve switching speed and reduce the driver size but may reduce the overcurrent safety margin. The same may be accomplished as future higher-performance MOSFET devices

are developed without impacting safety margin. Overall, a reduction in MOSFET count could reduce the total parts count and size of each driver board with potential reductions in the overall size and weight of the pulser enclosure.

As noted in Fig. 133.74, the trailing edge of the two largest-amplitude, 25-ns pulses has a tail that increases the rise time. Future work may expose the cause of this and determine a correction.

Summary

A solid-state, 50-Ω, 10-kV, 100-ns Pockels-cell driver has been designed and assembled as a replacement for aging thyatron switched drivers. The design is based on the inductive-adder approach developed at Lawrence Livermore National Laboratory. Performance tests in a CLARA produced results equivalent to the thyatron driver in the same application.

ACKNOWLEDGMENT

We acknowledge the efforts of the LLE Electronics Shop and Mechanical Engineering group in the design, assembly, and testing of the inductive-adder pulser. We also acknowledge the design consultation support provided by Ed Cook of LLNL. This work was supported by the U.S. Department of Energy Office of Inertial Confinement Fusion under Cooperative Agreement No. DEFC52-08NA28302, the University of Rochester, and the New York State Energy Research and Development Authority. The support of DOE does not constitute an endorsement by DOE of the views expressed in this article.

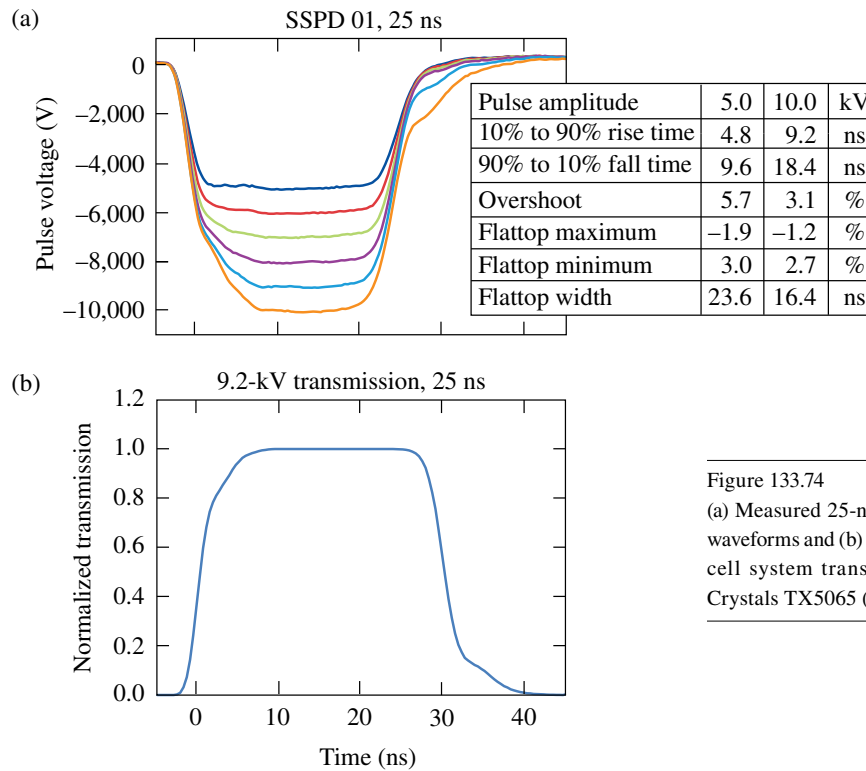


Figure 133.74
 (a) Measured 25-ns output pulse electrical waveforms and (b) 25-ns measured Pockels-cell system transmission for Cleveland Crystals TX5065 (Ref. 12).

G9730JR

REFERENCES

1. A. Babushkin, J. H. Kelly, C. T. Cotton, M. A. Labuzeta, M. O. Miller, T. A. Safford, R. G. Roides, W. Seka, I. Will, M. D. Tracy, and D. L. Brown, in *Third International Conference on Solid State Lasers for Application to Inertial Confinement Fusion*, edited by W. H. Lowdermilk (SPIE, Bellingham, WA, 1999), Vol. 3492, pp. 939–943.
2. V. Bagnoud, M. J. Guardalben, J. Puth, J. D. Zuegel, T. Mooney, and P. Dumas, *Appl. Opt.* **44**, 282 (2005).
3. Series 5056D Self-Contained Q-Switch Driver Data Sheet, FastPulse Technology, Inc., Lasermetrics Division, Saddle Brook, NJ 07663 (see <http://www.fastpulse.com/pdf/5056D.pdf>).
4. “Pumped Diode Regen Cavity Switch,” E-DN-B-022, Laboratory for Laser Energetics, University of Rochester, Rochester, NY (19 October 2004).
5. Pulse Generators, Models 3148 and 3150, Operating Instructions and Service Manual, Bournlea Instruments, Ltd., Ipswich, England (1990).
6. IXZR08N120 and IXZR08N120A/B Z-MOS RF Power MOSFET Data Sheet, IXYS Colorado, Fort Collins, CO 80525 (see http://www.directedenergy.com/index.php?page=shop.product_details&flypage=flypage.tpl&product_id=71&category_id=15&option=com_virtuemart&Itemid=34).
7. FMMT415 and FMMT417 SOT23 NPN Silicon Planar Avalanche Transistor Data Sheets, Diodes Incorporated, Plano, TX 75024 (see <http://www.diodes.com/datasheets/FMMT415.pdf>).
8. V. N. Efanov *et al.*, in *11th IEEE Pulsed Power Conference, 1997* (IEEE, Piscataway, NJ, 2013), Vol. 2, pp. 988–991.
9. V. A. Kozlov *et al.*, in *Conference Record of the Twenty-Fifth International Power Modulator Symposium and 2002 High-Voltage Workshop*, edited by H. C. Kirbie, D. Goebel, and L. Gordon (IEEE, Piscataway, NJ, 2002), pp. 441–444.
10. E. G. Cook *et al.*, in *Proceedings of the Particle Accelerator Conference, 2005* (IEEE, Piscataway, NJ, 2005), pp. 637–641.
11. “OMEGA EP PEPC Inductive Adder Solid State Pulser Requirement Specification,” C-AP-R-001, Laboratory for Laser Energetics, University of Rochester, Rochester, NY (4 January 2005).
12. Large Aperture Pockels Cells Specifications, Cleveland Crystals, Inc. (CCI), Highland Hts, OH 44143 (see www.clevelandcrystals.com/tx.htm).
13. Magnetic Alloy 2605SA1 Technical Bulletin, Metglas®, Inc., Conway, SC 29526 (see <http://metglas.com/assets/pdf/2605sa1.pdf>).
14. M. Plonus, *Applied Electromagnetics* (McGraw-Hill, New York, 1978).
15. J. Millman and C. C. Halkias, *Integrated Electronics: Analog and Digital Circuits and Systems*, McGraw-Hill Electrical and Electronic Engineering Series (McGraw-Hill, New York, 1972).
16. W. Zhang *et al.*, in *Proceedings of the 2007 IEEE Particle Accelerator Conference (PAC)* (IEEE, Piscataway, NJ, 2007), pp. 2553–2555.

Publications and Conference Presentations

Publications

- B. Beeman, A. G. MacPhee, J. R. Kimbrough, G. A. Lacaille, M. A. Barrios, J. Emig, J. R. Hunter, E. K. Miller, and W. R. Donaldson, "Mach-Zehnder Modulator Performance Using the Comet Laser Facility and Implications for Use on NIF," in *Target Diagnostics Physics and Engineering for Inertial Confinement Fusion*, edited by P. Bell and G. P. Grim (SPIE, Bellingham, WA, 2012), Vol. 8505, Paper 850507.
- D. T. Casey, J. A. Frenje, F. H. Séguin, C. K. Li, M. J. Rosenberg, H. Rinderknecht, M. J.-E. Manuel, M. Gatu Johnson, J. C. Schaeffer, R. Frankel, N. Sinenian, R. A. Childs, R. D. Petrasso, V. Yu. Glebov, T. C. Sangster, M. Burke, and S. Roberts, "The Coincidence Counting Technique for Orders of Magnitude Background Reduction in Data Obtained with the Magnetic Recoil Spectrometer at OMEGA and the NIF," *Rev. Sci. Instrum.* **82**, 073502 (2011).
- D. E. Fratanduono, T. R. Boehly, P. M. Celliers, M. A. Barrios, J. H. Eggert, R. F. Smith, D. G. Hicks, G. W. Collins, and D. D. Meyerhofer, "The Direct Measurement of Ablation Pressure Driven by 351-nm Laser Radiation," *J. Appl. Phys.* **110**, 073110 (2011).
- D. H. Froula, D. T. Michel, I. V. Igumenshchev, S. X. Hu, B. Yaakobi, J. F. Myatt, D. H. Edgell, R. Follett, V. Yu. Glebov, V. N. Goncharov, T. J. Kessler, A. V. Maximov, P. B. Radha, T. C. Sangster, W. Seka, R. W. Short, A. A. Solodov, C. Sorce, and C. Stoeckl, "Laser-Plasma Interactions in Direct-Drive Ignition Plasmas," *Plasma Phys. Control. Fusion* **54**, 124016 (2012).
- S. Hamel, L. X. Benedict, P. M. Celliers, M. A. Barrios, T. R. Boehly, G. W. Collins, T. Döppner, J. H. Eggert, D. R. Farley, D. G. Hicks, J. L. Kline, A. Lazicki, S. LePape, A. J. Mackinnon, J. D. Moody, H. F. Robey, E. Schwegler, and P. A. Sterne, "Equation of State of CH_{1.36}: First-Principles Molecular Dynamics Simulations and Shock-and-Release Wave Speed Measurements," *Phys. Rev. B* **86**, 094113 (2012).
- N. L. Kugland, D. D. Ryutov, P.-Y. Chang, R. P. Drake, G. Fiksel, D. H. Froula, S. H. Glenzer, G. Gregori, M. Grosskopf, M. Koenig, Y. Kuramitsu, C. Kuranz, M. C. Levy, E. Liang, J. Meinecke, F. Miniati, T. Morita, A. Pelka, C. Plechaty, R. Presura, A. Ravasio, B. A. Remington, B. Reville, J. S. Ross, Y. Sakawa, A. Spitkovsky, H. Takabe, and H.-S. Park, "Self-Organized Electromagnetic Field Structures in Laser-Produced Counter-Streaming Plasmas," *Nat. Phys.* **8**, 809 (2012).
- O. Landoas, V. Yu. Glebov, B. Rossé, M. Briat, L. Disdier, T. C. Sangster, T. Duffy, J. G. Marmouget, C. Varignon, X. Ledoux, T. Caillaud, I. Thfoin, and J.-L. Bourgade, "Absolute Calibration Method for Laser Megajoule Neutron Yield Measurement by Activation Diagnostics," *Rev. Sci. Instrum.* **82**, 073501 (2011).
- P. Loubeyre, S. Brygoo, J. Eggert, P. M. Celliers, D. K. Spaulding, J. R. Rygg, T. R. Boehly, G. W. Collins, and R. Jeanloz, "Extended Data Set for the Equation of State of Warm Dense Hydrogen Isotopes," *Phys. Rev. B* **86**, 144115 (2012).
- K. L. Marshall, C. Dorrer, M. Vargas, A. Gnolek, M. Statt, and S.-H. Chen, "Photoaligned Liquid Crystal Devices for High-Peak-Power Laser Applications," in *Liquid Crystals XVI*, edited by I. C. Khoo (SPIE, Bellingham, WA, 2012), Vol. 8475, Paper 84750U (invited).
- K. Mehrotra, H. P. Howard, S. D. Jacobs, and J. C. Lambropoulos, "Mechanical Characterization of 'Blister' Defects on Optical Oxide Multilayers Using Nanoindentation," in *Nanocomposites, Nanostructures and Heterostructures of Correlated Oxide Systems*, edited by T. Endo, H. Nishikawa, N. Iwata, A. Bhattacharya, and L. W. Martin, *Mat. Res. Soc. Symp. Proc.* Vol. 1454 (Cambridge University Press, Cambridge, England, 2012), pp. 215–220.
- D. T. Michel, A. V. Maximov, R. W. Short, S. X. Hu, J. F. Myatt, W. Seka, A. A. Solodov, B. Yaakobi, and D. H. Froula, "Experimental Validation of the Two-Plasmon-Decay Common-Wave Process," *Phys. Rev. Lett.* **109**, 155007 (2012).

C. Mileham, C. Stoeckl, W. Theobald, G. Fiksel, D. Guy, R. K. Junquist, P. M. Nilson, T. C. Sangster, and M. J. Shoup III, “Crystal Imager Development at the Laboratory for Laser Energetics,” in *Target Diagnostics Physics and Engineering for Inertial Confinement Fusion*, edited by P. Bell and G. P. Grim (SPIE, Bellingham, WA, 2012), Vol. 8505, Paper 85050L.

S. Papernov, E. Shin, T. Murray, A. W. Schmid, and J. B. Oliver, “355-nm Absorption in HfO₂ and SiO₂ Monolayers with Embedded Hf Nanoclusters Studied Using Photothermal Heterodyne Imaging,” in *Laser-Induced Damage in Optical Materials: 2012*, edited by G. J. Exarhos, V. E. Gruzdev, J. A. Menapace, D. Ristau, and M. J. Soileau (SPIE, Bellingham, WA, 2012), Vol. 8530, Paper 85301H.

S. P. Regan, K. Falk, G. Gregori, P. B. Radha, S. X. Hu, T. R. Boehly, B. J. B. Crowley, S. H. Glenzer, O. L. Landen, D. O. Gericke, T. Döppner, D. D. Meyerhofer, C. D. Murphy, T. C. Sangster, and J. Vorberger, “Inelastic X-Ray Scattering from Shocked Liquid Deuterium,” *Phys. Rev. Lett.* **109**, 265003 (2012).

M. J. Rosenberg, J. S. Ross, C. K. Li, R. P. J. Town, F. H. Séguin, J. A. Frenje, D. H. Froula, and R. D. Petrasso, “Characterization of Single and Colliding Laser-Produced Plasma Bubbles

Using Thomson Scattering and Proton Radiography,” *Phys. Rev. E* **86**, 056407 (2012).

J. R. Rygg, J. H. Eggert, A. E. Lazicki, F. Coppari, J. A. Hawreliak, D. G. Hicks, R. F. Smith, C. M. Sorce, T. M. Uphaus, B. Yaakobi, and G. W. Collins, “Powder Diffraction from Solids in the Terapascal Regime,” *Rev. Sci. Instrum.* **83**, 113904 (2012).

W. Theobald, R. Nora, M. Lafon, A. Casner, X. Ribeyre, K. S. Anderson, R. Betti, J. A. Delettrez, J. A. Frenje, V. Yu. Glebov, O. V. Gotchev, M. Hohenberger, S. X. Hu, F. J. Marshall, D. D. Meyerhofer, T. C. Sangster, G. Schurtz, W. Seka, V. A. Smalyuk, C. Stoeckl, and B. Yaakobi, “Spherical Shock-Ignition Experiments with the 40 + 20-Beam Configuration on OMEGA,” *Phys. Plasmas* **19**, 102706 (2012).

H. X. Vu, D. F. DuBois, J. F. Myatt, and D. A. Russell, “Hot-Electron Production and Suprathermal Heat Flux Scaling with Laser Intensity from the Two-Plasmon–Decay Instability,” *Phys. Plasmas* **19**, 102703 (2012).

H. X. Vu, D. F. DuBois, D. A. Russell, and J. F. Myatt, “Hot-Electron Generation by ‘Cavitating’ Langmuir Turbulence in the Nonlinear Stage of the Two-Plasmon–Decay Instability,” *Phys. Plasmas* **19**, 102708 (2012).

Forthcoming Publications

V. N. Goncharov, “Cryogenic Deuterium and Deuterium–Tritium Direct-Drive Implosions on OMEGA,” to be published in *Laser–Plasma Interactions and Applications*.

D. R. Harding and W. T. Shmayda, “Stress-Radiation–Induced Swelling in Plastic Capsules,” to be published in *Fusion Science and Technology*.

D. R. Harding, M. D. Wittman, and D. H. Edgell, “Considerations and Requirements for Providing Cryogenic Targets for Direct-Drive Inertial Fusion Implosions at the National Ignition Facility,” to be published in *Fusion Science and Technology*.

H. P. Howard, A. F. Aiello, J. G. Dressler, N. R. Edwards, T. J. Kessler, A. A. Kozlov, I. R. T. Manwaring, K. L. Marshall, J. B. Oliver, A. L. Rigatti, A. N. Roux, A. W. Schmid, N. P. Slaney, C. C. Smith, B. N. Taylor, and S. D. Jacobs, “Improving the Performance of High-Laser-Damage-Threshold, Multilayer Dielectric Pulse-Compression Gratings Through Low-Temperature Chemical Cleaning,” to be published in *Applied Optics*.

I. V. Igumenshchev, D. H. Froula, D. H. Edgell, V. N. Goncharov, T. J. Kessler, F. J. Marshall, R. L. McCrory, P. W. McKenty, D. D. Meyerhofer, D. T. Michel, T. C. Sangster, W. Seka, and S. Skupsky, “Laser-Beam Zooming to Mitigate Crossed-Beam Energy Losses in Direct-Drive Implosions,” to be published in *Physical Review Letters*.

M. Lafon, X. Ribeyre, and G. Schurtz, “Optimal Conditions for Shock Ignition of Scaled Cryogenic DT Targets,” to be published in *Physics of Plasmas*.

K. Mehrotra, H. P. Howard, S. D. Jacobs, and J. C. Lambropoulos, “Nanoindentation Probing of High-Aspect-Ratio Pillar Structures on Optical Multilayer Dielectric Diffraction Gratings,” to be published in the *Material Research Society Proceedings*.

W. T. Shmayda, D. R. Harding, V. Veerstedt, C. Kingsley, M. Hallgren, and S. J. Loucks, “Micron-Scaled Defects on Cryogenic Targets: An Assessment of Condensate Sources,” to be published in *Fusion Science and Technology*.

Conference Presentations

The following presentations were made at the 24th IAEA Fusion Energy Conference, San Diego, CA, 8–13 October 2012:

R. Betti, “Theory of Ignition and Hydro-Equivalence for Inertial Confinement Fusion.”

R. L. McCrory, D. D. Meyerhofer, R. Betti, T. R. Boehly, D. T. Casey, T. J. B. Collins, R. S. Craxton, J. A. Delettrez, D. H. Edgell, R. Epstein, J. A. Frenje, D. H. Froula, M. Gatu-Johnson, V. Yu. Glebov, V. N. Goncharov, D. R. Harding, M. Hohenberger, S. X. Hu, I. V. Igumenshchev, T. J. Kessler, J. P. Knauer, C. K. Li, J. A. Marozas, F. J. Marshall, P. W. McKenty, T. Michel, J. F. Myatt, P. M. Nilson, S. J. Padalino, R. D. Petrasso, P. B. Radha, S. P. Regan, T. C. Sangster, F. H. Séguin, W. Seka, R. W. Short, O. Shvydky, S. Skupsky, J. M. Soures, C. Stoeckl, W. Theobald, B. Yaakobi, and J. D. Zuegel, “Progress Toward Polar-Drive Ignition for the NIF.”

The following presentations were made at Frontiers in Optics 2012, Rochester, NY, 14–18 October 2012:

C. Dorrer, V. Bagnoud, I. A. Begishev, J. Bromage, A. Consentino, M. J. Guardalben, A. V. Okishev, J. Qiao, R. G. Roides, and J. D. Zuegel, “OPCPA Front End and Contrast Optimization for the OMEGA EP Kilojoule, Picosecond Laser.”

C. Dorrer, K. L. Marshall, S. H. Chen, M. Vargas, M. Statt, C. Caggiano, S. K.-H. Wei, J. B. Oliver, P. Leung, K. Wegman, J. Boulé, Z. Zhao, S. Papernov, A. Rakhmann, and I. Jovanovic, “High-Damage-Threshold Beam Shaping Using Optically Patterned Liquid Crystal Devices.”

T. Petersen and J. Bromage, “Intracavity Chirped-Pulse Amplification for High-Energy, Ultrafast Optical Parametric Oscillators.”

J. P. Knauer, P.-Y. Chang, M. Hohenberger, G. Fiksel, F. J. Marshall, D. D. Meyerhofer, R. Betti, F. H. Séguin, and R. D. Petrasso, “Compressing Magnetic Fields with High-Energy Lasers,” 14th International Conference on Megagauss Magnetic Field Generation and Related Topics, Maui, HI, 14–19 October 2012.

S. Papernov, “Mechanisms of Near-Ultraviolet, Nanosecond-Pulse Laser Damage in HfO₂/SiO₂-Based Multilayer Coatings,” Frontiers of Optical Coatings, Hangzhou, China, 15–18 October 2012.

The following presentations were made at the 54th Annual Meeting of the APS Division of Plasma Physics, Providence, RI, 29 October–2 November 2012:

K. S. Anderson, R. Betti, P. W. McKenty, T. J. B. Collins, M. Hohenberger, W. Theobald, R. S. Craxton, J. A. Delettrez, M. Lafon, J. A. Marozas, R. Nora, S. Skupsky, and A. Shvydky, “A Polar-Drive Shock-Ignition Design for the National Ignition Facility” (invited).

R. Betti, R. Nora, M. Lafon, J. F. Myatt, C. Ren, R. Yan, J. Li, A. V. Maximov, D. H. Froula, W. Seka, K. S. Anderson, R. Epstein, J. A. Delettrez, S. X. Hu, P. M. Nilson, V. A. Smalyuk, and W. Theobald, “High-Z Ablator Targets for Direct-Drive ICF.”

T. R. Boehly, V. N. Goncharov, S. X. Hu, J. A. Marozas, T. C. Sangster, and D. D. Meyerhofer, “The Growth of Surface Defects Driven by Shock Waves.”

A. Bose, R. Betti, P.-Y. Chang, and J. R. Davies, “Non-Inertial Eulerian Hydrodynamic Code for ICF Implosion Simulations.”

P.-Y. Chang, A. Agliata, D. H. Barnak, W. Bittle, G. Fiksel, D. Hasset, M. Hohenberger, D. Lonobile, M. J. Shoup III, C. Taylor, and R. Betti, “Experimental Platform for Magnetized HEDP Science at OMEGA.”

T. J. B. Collins, J. A. Marozas, K. S. Anderson, V. N. Goncharov, P. W. McKenty, R. Betti, and S. Skupsky, “Optimization with *Telios* of the Polar-Drive Point Design for the National Ignition Facility.”

R. S. Craxton, P. W. McKenty, P. A. Olson, D. H. Froula, D. T. Michel, S. Le Pape, and A. J. MacKinnon, “Optimization of Drive Uniformity in NIF Polar-Drive Implosions Using Gated X-Ray Self-Emission Images.”

J. A. Delettrez, T. J. B. Collins, A. Shvydky, G. Moses, D. Cao, and M. M. Marinak, “Effect of Nonlocal Electron

Transport in Two Dimensions on the Symmetry of Polar-Drive-Ignition Targets.”

D. H. Edgell, P. B. Radha, V. N. Goncharov, I. V. Igumenshchev, J. Marozas, J. F. Myatt, W. Seka, and D. H. Froula, “Modeling Cross-Beam Energy Transfer for Polar-Drive Experiments.”

B. Eichman, W. Theobald, C. Stoeckl, C. Mileham, and T. C. Sangster, “Time-Resolved X-Ray Brightness Measurements from Short-Pulse Laser-Irradiated Thin Foils.”

R. Epstein, S. P. Regan, R. L. McCrory, D. D. Meyerhofer, T. C. Sangster, J. L. Tucker, B. A. Hammel, L. J. Suter, H. Scott, D. A. Callahan, C. Cerjan, N. Izumi, M. H. Key, O. L. Landen, N. B. Meezan, B. A. Remington, I. E. Golovkin, J. J. MacFarlane, R. C. Mancini, and K. J. Peterson, “Spectroscopy of Mid-Z Shell Additives in Implosions at the National Ignition Facility.”

G. Fiksel, V. A. Goncharov, D. D. Meyerhofer, T. C. Sangster, B. Yaakobi, M. J. Bonino, and V. A. Smalyuk, “Experimental Reduction of Laser Imprinting and Rayleigh–Taylor Growth in Spherically Compressed, Medium-Z–Doped Plastic Targets.”

R. K. Follett, D. T. Michel, J. F. Myatt, S. X. Hu, B. Yaakobi, and D. H. Froula, “Thomson-Scattering Measurements of Ion-Acoustic Wave Amplitudes Driven by the Two-Plasmon-Decay Instability.”

C. J. Forrest, V. Yu. Glebov, J. P. Knauer, T. C. Sangster, C. Stoeckl, S. Gardner, K. S. Anderson, P. B. Radha, V. N. Goncharov, D. D. Meyerhofer, C. Morrison, D. Baldwin, and S. Padalino, “Modeling Cold Fusion Distributions Inferred from Elastically Scattered Neutrons in Layered Cryogenic DT Direct-Drive Implosions.”

J. A. Frenje, D. T. Casey, M. Gatu-Johnson, C. K. Li, F. H. Séguin, R. D. Petrasso, R. Bionta, M. J. Edwards, S. H. Glenzer, O. L. Landen, A. J. MacKinnon, D. H. Munro, P. J. Springer, J. D. Kilkenny, V. Yu. Glebov, T. C. Sangster, and C. Stoeckl, “A Streak-Camera–Based Magnetic Recoil Spectrometer (SCMRS) for Measurements of $T_i(t)$, $Y_n(t)$, $d_{sr}(t)$ on OMEGA and the NIF.”

D. H. Froula, B. Yaakobi, D. T. Michel, D. H. Edgell, R. K. Follett, W. Seka, C. Stoeckl, T. C. Sangster, A. A. Solodov, S. X. Hu, I. V. Igumenshchev, P. B. Radha, J. A. Delettrez, J. F. Myatt, R. W. Short, and V. N. Goncharov, “Two-Plasmon–

Decay Electron-Divergence Measurements in Direct-Drive Implosions on OMEGA.”

L. Gao, P. M. Nilson, I. V. Igumenshchev, S. X. Hu, J. R. Davies, C. Stoeckl, D. H. Froula, R. Betti, D. D. Meyerhofer, and M. G. Haines, “Magnetic-Field Generation by the Rayleigh–Taylor Instability in Planar Targets on OMEGA EP.”

M. Gatu-Johnson, D. T. Casey, J. A. Frenje, C. K. Li, F. H. Séguin, R. D. Petrasso, V. Yu. Glebov, J. P. Knauer, T. C. Sangster, R. Bionta, M. J. Edwards, S. H. Glenzer, S. P. Hatchett, O. L. Landen, A. J. MacKinnon, D. McNabb, D. H. Munro, J. Pino, S. Sepke, P. J. Springer, and J. D. Kilkenny, “Measurements and Interpretation of TT and Down-Scattered DT Neutron Spectra on OMEGA and the NIF.”

V. Yu. Glebov, C. Stoeckl, T. C. Sangster, C. Forrest, and R. A. Lerche, “Absolute Ion-Temperature Measurements in DD and DT Implosions on OMEGA.”

V. N. Goncharov, T. C. Sangster, R. Epstein, S. X. Hu, I. V. Igumenshchev, D. H. Froula, R. L. McCrory, D. D. Meyerhofer, D. T. Michel, P. B. Radha, W. Seka, S. Skupsky, C. Stoeckl, D. T. Casey, J. A. Frenje, and M. Gatu-Johnson, “Improving Implosion Velocity in Cryogenic Deuterium–Tritium Implosions on OMEGA.”

D. Haberberger, D. H. Froula, S. X. Hu, C. Joshi, S. Tochitsky, C. Gong, F. Fiuza, and L. Silva, “Collisionless Shock Wave Acceleration of Ions on OMEGA EP.”

M. Hohenberger, W. Theobald, S. X. Hu, R. Betti, K. S. Anderson, T. R. Boehly, A. Casner, D. D. Meyerhofer, X. Ribeyre, T. C. Sangster, G. Schurtz, W. Seka, C. Stoeckl, and B. Yaakobi, “Shock-Ignition Studies in Planar Geometry on OMEGA.”

S. X. Hu, V. N. Goncharov, and S. Skupsky, “Burning DT Plasmas with Ultrafast Soft X-Ray Pulses.”

I. V. Igumenshchev, V. N. Goncharov, T. R. Boehly, T. C. Sangster, and S. Skupsky, “Fuel–Ablator Mix from Surface Nonuniformities in Directly Driven Implosions.”

S. Ivancic, W. Theobald, R. Boni, D. H. Froula, S. X. Hu, and D. D. Meyerhofer, “Ray-Trace Simulations for the Optical 4ω Probe Diagnostic on OMEGA EP.”

- J. P. Knauer, “Neutron Spectroscopy at the National Ignition Facility” (invited).
- M. Lafon, R. Nora, K. S. Anderson, and R. Betti, “Hydrodynamic Simulations of Direct-Drive Targets with Moderate-Z Ablators.”
- J. Li, R. Yan, C. Ren, A. V. Maximov, W. B. Mori, and F. S. Tsung, “Collisional Effects on Hot-Electron Generation in Two-Plasmon-Decay Instability in Inertial Confinement Fusion.”
- M. J.-E. Manuel, C. K. Li, F. H. Séguin, D. T. Casey, R. D. Petrasso, S. X. Hu, R. Betti, J. D. Hager, D. D. Meyerhofer, and V. A. Smalyuk, “Measurements of Rayleigh–Taylor-Induced Magnetic Fields During Linear and Nonlinear Growth Phases.”
- J. A. Marozas, T. J. B. Collins, D. H. Edgell, I. V. Igumenshchev, and J. F. Myatt, “Cross-Beam Energy Transfer with Additional Ion Heating Integrated into the 2-D Hydrodynamics Code *DRACO*.”
- F. J. Marshall, P. B. Radha, M. J. Bonino, J. A. Delettrez, R. Epstein, S. Skupsky, and E. Giraldez, “Polar-Drive Experiments with Shimmed Targets on OMEGA.”
- A. V. Maximov, J. F. Myatt, R. W. Short, I. V. Igumenshchev, D. H. Edgell, and W. Seka, “Scattering of Multiple Crossing Laser Beams in Direct-Drive ICF Plasmas.”
- C. McCoy, T. R. Boehly, P. M. Nilson, T. J. B. Collins, T. C. Sangster, D. D. Meyerhofer, D. E. Fratanduono, P. M. Celliers, and D. G. Hicks, “The Release of Shocked Materials.”
- P. W. McKenty, R. S. Craxton, A. Shvydky, D. H. Froula, D. T. Michel, J. A. Marozas, T. C. Sangster, D. D. Meyerhofer, R. L. McCrory, J. D. Kilkenny, A. Nikroo, M. L. Hoppe, S. Le Pape, A. J. MacKinnon, and D. H. Munro, “Drive-Symmetry Studies of NIF Exploding-Pusher Experiments.”
- D. D. Meyerhofer, D. H. Froula, V. N. Goncharov, I. V. Igumenshchev, S. J. Loucks, P. W. McKenty, R. L. McCrory, P. B. Radha, and T. C. Sangster, “Polar-Drive–Ignition Experimental Plan on the NIF.”
- D. T. Michel, A. V. Maximov, R. W. Short, J. A. Delettrez, D. Edgell, S. X. Hu, I. V. Igumenshchev, J. F. Myatt, A. A. Solodov, C. Stoeckl, B. Yaakobi, and D. H. Froula, “Measured Hot-Electron Intensity Thresholds Quantified by a Two-Plasmon–Decay Gain in Various Experimental Configurations” (invited).
- J. F. Myatt, J. Zhang, R. W. Short, A. V. Maximov, A. A. Solodov, W. Seka, D. H. Froula, B. Yaakobi, D. T. Michel, D. H. Edgell, D. F. DuBois, D. A. Russell, and H. X. Vu, “Mitigating Two-Plasmon–Decay Hot-Electron Generation Through the Modification of Langmuir and Ion-Acoustic Dissipation in Directly Driven Targets.”
- P. M. Nilson, G. Fiksel, C. Stoeckl, P. A. Jaanimagi, C. Mileham, W. Theobald, J. R. Davies, J. F. Myatt, A. A. Solodov, D. H. Froula, R. Betti, and D. D. Meyerhofer, “Tracking Intense Flows of Energy Inside OMEGA EP Laser-Irradiated Metal Targets.”
- R. Nora, W. Theobald, R. Betti, J. A. Delettrez, A. A. Solodov, K. S. Anderson, W. Seka, and M. Lafon, “Analysis of Fast Electrons in Shock-Ignition Implosions on OMEGA.”
- S. Padalino, M. Krieger, M. Russ, D. Polsin, M. Bienstock, D. Ellison, and A. Simone, “Design and Characterization of a Collimated Neutron Beam User Facility at SUNY Geneseo.”
- S. Padalino, D. Polsin, M. Russ, M. Krieger, M. Bienstock, D. Ellison, A. Simone, C. Stillman, M. Yuly, K. Mann, T. Reynolds, and C. Sangster, “Cross Section of the $(n, 2n)$ Reaction in ^{12}C in the Energy Interval 20–30 MeV.”
- S. Padalino, D. Polsin, M. Russ, M. Krieger, M. Bienstock, D. Ellison, A. Simone, C. Stillman, M. Yuly, K. Mann, T. Reynolds, and C. Sangster, “In Situ Calibration for Proton Particle Telescope.”
- S. Padalino, M. Russ, D. Polsin, M. Krieger, C. Stillman, M. Bienstock, D. Ellison, A. Simone, M. Yuly, K. Mann, T. Reynolds, and C. Sangster, “Coincidence Efficiency Measurement Using $^{11}\text{B}(p,n)^{11}\text{C}$.”
- J. Park, C. Ren, J. C. Workman, and E. G. Blackman, “Particle-in-Cell Simulations of Particle Energization via Shock Drift Acceleration from Low Mach Number Quasi-Perpendicular Shocks in Solar Flares.”
- P. B. Radha, F. J. Marshall, J. A. Marozas, A. Shvydky, I. Gabalski, T. R. Boehly, T. J. B. Collins, R. S. Craxton, D. H.

Edgell, R. Epstein, J. Frenje, D. H. Froula, V. N. Goncharov, M. Hohenberger, R. L. McCrory, P. W. McKenty, D. D. Meyerhofer, R. D. Petrasso, T. C. Sangster, and S. Skupsky, "Polar-Drive Implosions on OMEGA and the National Ignition Facility" (invited).

S. P. Regan, "X-Ray Thomson Scattering: Incisive Probe for Warm, Dense Matter."

S. P. Regan, R. Epstein, B. A. Hammel, L. J. Suter, J. Ralph, H. Scott, M. A. Barrios, D. K. Bradley, C. Cerjan, T. Doepfner, S. H. Glenzer, I. E. Golovkin, S. W. Haan, O. Jones, J. D. Kilkenny, J. L. Kline, and O. L. Landen, J. J. MacFarlane, R. C. Mancini, H.-S. Park, B. A. Remington, V. A. Smalyuk, and J. Springer, "Hot-Spot Mix and Compressed Ablator ρR Measurements in Ignition-Scale Implosions."

H. G. Rinderknecht, C. K. Li, M. Gatu-Johnson, A. Zylstra, M. Rosenberg, J. A. Frenje, F. H. Séguin, R. D. Petrasso, P. A. Amendt, A. Miles, J. R. Rygg, V. Yu. Glebov, C. Stoeckl, and T. C. Sangster, "Anomalous Shock Yields in Direct- and Indirect-Drive D^3He Exploding Pushers."

T. C. Sangster, V. N. Goncharov, R. Betti, P. B. Radha, T. R. Boehly, D. T. Casey, T. J. B. Collins, R. S. Craxton, J. A. Delettrez, D. H. Edgell, R. Epstein, C. J. Forrest, J. A. Frenje, D. H. Froula, M. Gatu-Johnson, V. Yu. Glebov, D. R. Harding, M. Hohenberger, S. X. Hu, I. V. Igumenshchev, R. T. Janezic, J. H. Kelly, T. J. Kessler, C. Kingsley, T. Z. Kosc, J. P. Knauer, S. J. Loucks, J. A. Marozas, F. J. Marshall, A. V. Maximov, R. L. McCrory, P. W. McKenty, D. D. Meyerhofer, D. T. Michel, J. F. Myatt, R. D. Petrasso, S. P. Regan, W. Seka, W. T. Shmayda, R. W. Short, A. Shvydky, S. Skupsky, J. M. Soures, C. Stoeckl, W. Theobald, V. Versteeg, B. Yaakobi, and J. D. Zuegel, "Improving Cryogenic DT Implosion Performance on OMEGA" (invited).

W. Seka, D. H. Edgell, D. H. Froula, J. Katz, J. F. Myatt, J. Zhang, R. W. Short, D. T. Michel, A. V. Maximov, and V. N. Goncharov, "Multibeam Two-Plasmon Decay: Experimental Signatures and Diagnostic Applications."

R. W. Short, J. F. Myatt, A. V. Maximov, D. T. Michel, D. H. Froula, and J. Zhang, "The Effects of Beam Polarization and Orientation on Convective and Absolute Two-Plasmon Decay by Multiple Laser Beams."

A. Shvydky, M. Hohenberger, J. A. Marozas, M. J. Bonino, D. Canning, T. J. B. Collins, T. J. Kessler, P. W. McKenty, T. C. Sangster, and J. D. Zuegel, "Two-Dimensional Numerical Evaluation of 1-D Multi-FM SSD Experiments."

N. Sinenian, M. J.-E. Manuel, J. A. Frenje, F. H. Séguin, C. K. Li, R. D. Petrasso, V. N. Goncharov, J. A. Delettrez, C. Stoeckl, T. C. Sangster, and J. Cobble, "An Empirical Target-Discharging Model for Direct-Drive Implosions on OMEGA."

H. Sio, M. Rosenberg, H. G. Rinderknecht, D. T. Casey, A. Zylstra, C. Waugh, M. Gatu-Johnson, F. H. Séguin, C. K. Li, J. A. Frenje, R. D. Petrasso, J. A. Delettrez, V. Yu. Glebov, T. C. Sangster, C. Stoeckl, V. N. Goncharov, P. A. Amendt, C. Bellei, and S. C. Wilks, "Developing a D^3He Exploding-Pusher Platform to Study Kinetic Effects."

A. A. Solodov, W. Theobald, K. S. Anderson, A. Shvydky, R. Betti, J. F. Myatt, C. Stoeckl, and R. B. Stephens, "Simulations of Cone-in-Shell Targets for Integrated Fast-Ignition Experiments on OMEGA."

C. Stoeckl, J. A. Delettrez, G. Fiksel, D. Guy, R. K. Jungquist, C. Mileham, P. M. Nilson, T. C. Sangster, M. J. Shoup III, and W. Theobald, "Soft X-Ray Backlighting of Direct-Drive Implosions Using a Narrowband Crystal Imaging System."

W. Theobald, A. A. Solodov, C. Stoeckl, R. Epstein, V. Yu. Glebov, G. Fiksel, S. Ivancic, F. J. Marshall, G. McKiernan, C. Mileham, P. M. Nilson, T. C. Sangster, C. Jarrott, F. N. Beg, E. Giraldez, R. B. Stephens, M. S. Wei, H. McLean, H. Sawada, and J. Santos, "Monochromatic 8.05-keV Flash Radiography of Imploded Cone-in-Shell Targets."

C. Waugh, M. Rosenberg, J. A. Frenje, F. H. Séguin, R. D. Petrasso, V. Yu. Glebov, T. C. Sangster, and C. Stoeckl, "A New Platform for Calibrating nTOF Detectors at ICF Facilities Using CR-39-Based Proton Detectors."

J. Zhang, J. F. Myatt, R. W. Short, A. V. Maximov, H. X. Vu, D. A. Russell, and D. F. DuBois, "A Three-Dimensional Zharov Model of the Two-Plasmon-Decay Instability in Inhomogeneous Plasmas Driven by Multiple Laser Beams."

The following presentations were made at the 12th International Workshop on Fast Ignition of Fusion Targets, Napa Valley, CA, 4–8 November 2012:

J. R. Davies, “Scaling of Ignition Laser Parameters with Fast-Electron Parameters.”

A. A. Solodov, W. Theobald, K. S. Anderson, A. Shvydky, R. Betti, J. F. Myatt, and R. B. Stephens, “Integrated Fast-Ignition Experiments on OMEGA.”

S. P. Regan, R. Epstein, B. A. Hammel, L. J. Suter, C. A. Iglesias, B. G. Wilson, M. A. Barrios, D. K. Bradley, D. A. Callahan, C. Cerjan, T. Doeppner, M. J. Edwards, S. H. Glenzer, I. E. Golovkin, S. W. Haan, N. Izumi, O. S. Jones, J. D. Kilkenny, J. L. Kline, G. A. Kyrala, O. L. Landen, T. Ma, J. J. MacFarlane, R. C. Mancini, R. L. McCrory, N. B. Meezan, D. D. Meyerhofer, H.-S. Park, K. J. Peterson, J. Ralph, B. A. Remington, T. C. Sangster, V. A. Smalyuk, P. Springer, and R. P. J. Town, “X-Ray Spectroscopy of Ignition-Scale Implosions on the National Ignition Facility,” 15th Workshop on Radiative Properties of Hot Dense Matter, Santa Barbara, CA, 5–9 November 2012.

W. T. Shmayda, D. R. Harding, and T. B. Jones, “Tritium Fuel Cycle for Direct-Drive Inertial Fusion Reactors Using Microfluidics,” 2012 American Nuclear Society Winter Meeting and Nuclear Technology Expo, San Diego, CA, 11–15 November 2012.

D. R. Harding, W. Wang, and T. B. Jones, “Textured Silicon Surfaces for Moving Oil Droplets in ‘Lab-on-Chip’ Devices,” Material Research Society Fall Meeting, Boston, MA, 25–30 November 2012.

The following presentations were made at the Fusion Power Associates Meeting, Washington, DC, 5–6 December 2012:

R. Betti, “Fusion Science Center Activities on Advanced ICF Ignition.”

R. L. McCrory, “Progress Toward Polar-Drive Ignition for the NIF.”

